Mechanical properties on nanometer scale and their relations to composition and microstructure.

A nanoindentation study on carbon implanted Ti-6Al-4V.
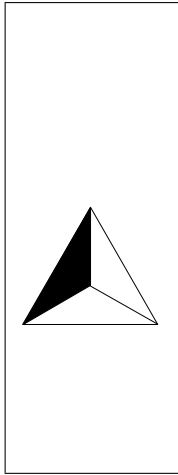
Table of Contents

Symbols and acronyms

Symbols

ν	Poisson ratio of the sample material
ν_i	Poisson ratio of the diamond indenter; $\nu_i = 0.07$
σ_y	yield stress
τ_c	critical shear stress
ε	constant (depending on the geometry of the indenter)
a, c	lattice parameters
A_c	projected contact area
a_i	fitting constants
$\vec{b}$	Burgers vector
b	length of the Burgers vector $\vec{b}$
c_f	load-frame compliance
c_s	compliance of the specimen
c_{tot}	total compliance
E	Young's modulus of the sample material
E_i	Young's modulus of the diamond indenter; $E_i = 1141$ GPa
E_r	reduced Young's modulus
f	volume fraction of precipitates
F_s	force supported by the sample
F_{el}	electrostatic force generated by the transducer
G	shear modulus

h	displacement
h_c	contact depth
h_i	intercept depth
h_{max}	maximum indentation depth
h_{sp}	sputter depth
H	hardness
H^i_{max}	maximum hardness value as obtained using the method i ($i =$ VLM, CLM, or CSM)
HV	Vickers hardness
I	indentation modulus
I^i_{max}	maximum value of the indentation modulus as obtained using the method i ($i =$ VLM, CLM, or CSM)
k_e	electrostatic force constant of the Hysitron transducer
k_s	spring constant of the suspension springs of the Hysitron transducer
P	load
P_{max}	maximum load
r	precipitate radius
S	stiffness
t	depth (see page 44)
$t^i_{max,H}$	depth at which H^i_{max} occurs
$t^i_{max,I}$	depth at which I^i_{max} occurs
V	voltage

Acronyms

AES	Auger Electron Spectroscopy
BF	Bright Field
CLM	Constant-Load Method
CSM	Cross-Section Method
DF	Dark Field
DSI	Depth-Sensing Indentation
EELS	Electron Energy Loss Spectrum
ESI	Electron Spectroscopic Imaging
FIB	Focused Ion Beam
LVM	Load-Variation Method
rms	root mean square (roughness)
SAD	Selected Area Diffraction
SEM	Scanning Electron Microscopy
SFM	Scanning Force Microscopy
SPM	Scanning Probe Microscopy
TEM	Transmission Electron Microscopy
UHMWPE	Ultra-High Molecular Weight Poly-Ethylene
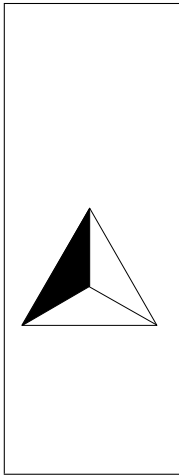
Summary

Carbon implantation into the titanium alloy Ti-6Al-4V improves the wear behaviour of this alloy against polyethylene [1]. This is used for surgical prostheses, in particular for artificial knee and hip joints, where the femoral bearing components consist of Ti-6Al-4V and the counterparts (tibial plateau and acetabular cup, respectively) are made of ultra-high molecular polyethylene (UHMWPE). Understanding of the influence of ion implantation on wear behaviour requires (i) the knowledge of the influence of the implantation parameters on the changes of composition and microstructure in the surface adjacent region (implanted region) of the sample and (ii) the knowledge of the effect of these compositional and microstructural variations on the mechanical properties within this region. The aim of the present work is the investigation of the latter. To this end, mechanical properties (hardness, indentation modulus), chemical composition, and microstructure within the carbon-implanted region of a Ti-6Al-4V alloy were determined as a function of depth and, for the first time, were related with each other with a depth accuracy as small as ± 20 nm.

The Ti-6Al-4V alloy specimens were doubly implanted with carbon ions using implantation energies of 120 keV and 60 keV and ion doses of $3 \cdot 10^{17}$ cm^{-2} and $4 \cdot 10^{17}$ cm^{-2}, respectively. This treatment led to an about 350 nm thick region — adjacent to the surface — enriched with carbon. The changes of chemical composition and microstructure within this implanted region were determined using standard means: Auger electron spectroscopy in combination with ion sputtering and cross sectional transmission electron microscopy, respectively. Hardness measurements on nanometer scale have only recently become possible with the development of the depth-sensing *nano*indentation technique (DSI) [2]. A standard method for assessing the change in hardness with depth with a depth resolution on nanometer scale — as necessary for the characterization of the variations present in an ion implanted region — was, however, not available.

In DSI, a diamond tip is pushed into the material to be probed and, after having reached a given maximum depth or load, is removed. During this procedure, the load

on as well as the displacement of the indenter are recorded. This load versus displacement behaviour represents a fingerprint of the mechanical properties of the material averaged over a certain volume, the size of which strongly increases with increasing load. Therefore, to obtain a high depth resolution (small probed volume), a small maximum load should be applied. Hardness-depth profiles, however, are — until now — usually assessed by gradually increasing the maximum load and thereby increasing the probed depth. Hence, the depth resolution of this load-variation method (LVM) becomes continuously smaller as the maximum load increases.

The depth-resolution of a hardness-depth profile can be enhanced if all hardness values of this profile are evaluated from indentations made to the same low maximum load. In order to determine a depth profile using such small and constant maximum loads two approaches were followed: the constant-load method (CLM) and the cross-section method (CSM).

By means of a model system, consisting of a 200 nm thick TiC film on a Ti-6Al-4V substrate, it is shown (see Chapter 2) that only the CSM, where the indentations are made perpendicularly to the hardness gradient on a cross section of the specimen, allows a direct determination of local changes in hardness with depth, with a depth resolution of a few nanometers. In the CLM, a depth profile is achieved by successive removing thin surface layers by ion sputtering and performing the indentations at each newly exposed surface. As in the LVM, the indentations are made perpendicularly to the original surface, *i.e.* in the direction of the hardness gradient. Therefore, the hardness-depth profiles obtained using the CLM and those obtained using the LVM suffer from the same aberration: they become smeared due to a combined response of the surface engineered region (film, implanted region) and the underlying (softer) substrate. The extend of this smearing is smaller, *i.e.* the depth resolution is higher, for the CLM as compared with the LVM because the same low maximum load is used for all indentations in the CLM.

The carbon depth profile of the carbon implanted Ti-6Al-4V alloy reflects the double implantation applied to the sample: it is characterized by the superposition of two flat-topped distributions. According to the larger dosis and the smaller kinetic energy of the C^{+}-ions used in the second implantation process ($60\,\mathrm{keV}/4\cdot10^{17}\,\mathrm{cm}^{-2}$) , the carbon content of the near-surface peak is larger than that of the peak resulting from the first implantation process ($120\,\mathrm{keV}/3\cdot10^{17}\,\mathrm{cm}^{-2}$). An evaluation of peak shape, peak intensity, and peak position of the $C\,(KLL)$ and the $Ti\,(LMM)$-Auger peaks in dependence of depth revealed that (i) the implanted carbon is completely bonded to titanium and that (ii) in the depth range between about 80–150 nm a large and nearly constant TiC-content is present.

The microstructure of the implanted region exhibits a complicated graded microstructure with a high density of TiC precipitates and dislocation networks. The precipitate density changes gradually with depth in accord with the carbon content. In the depth region with the highest carbon content an almost continuous TiC film had

formed. In one sample, in the depth range between about 50–100 nm twinned TiC was found.

The hardness-depth profile obtained using the CSM reflects well the microstructural and compositional variations within the carbon implanted region. Starting from the surface, the hardness value increases within a few ten nanometers from about 9 GPa to a value thrice as high. The shape of the hardness-depth profile is similar to that of the carbon content. The maximum hardness within the implanted region (27 GPa) occurs at that depth where the TiC content is maximal and an almost continuous TiC layer had formed. In zones with a smaller TiC precipitate density, the hardness can be quantitatively explained as due to TiC dispersion hardening.

The now available possibility to truly trace the hardness-depth profile of an ion implanted region and to relate this hardness-depth profile with the local variations in microstructure and composition, (also) provides a tool for the development of property-tailored ion implantation procedures.
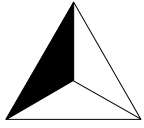
Preface
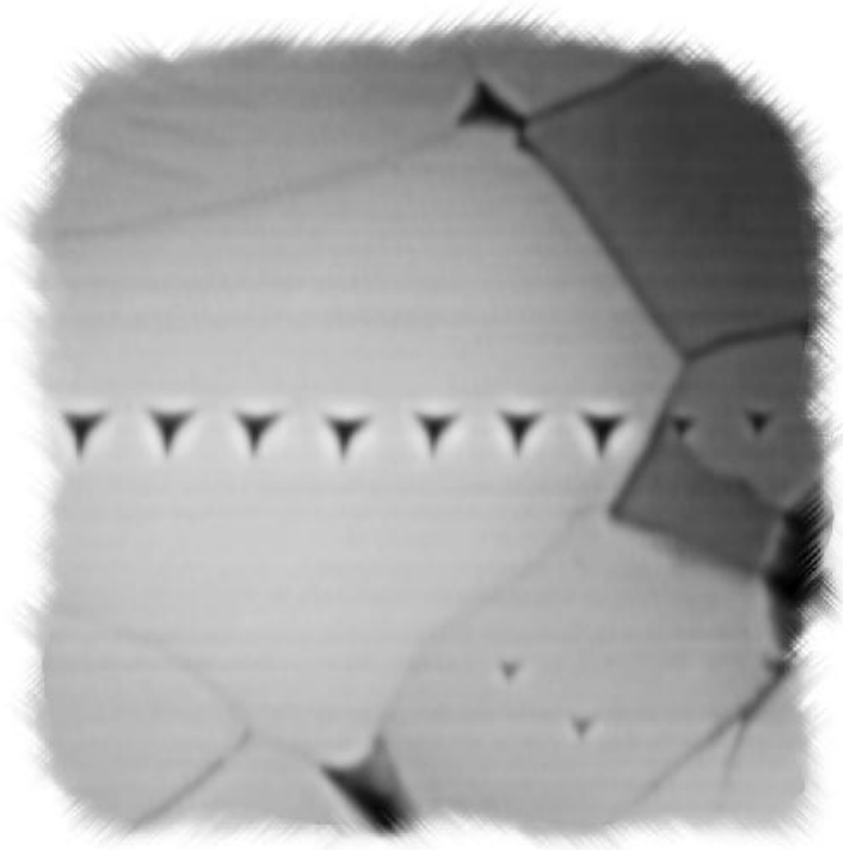
Hardness impressions in the surface of a multiphase alloy.
The larger indentations are about 45 nm deep and the smaller ones have
a depth of about 20 nm. The distance between the larger indentations is
about 600 nm.

The image of the indentation imprints on the last page illustrates what this dissertation is mainly about: indentation hardness testing. One hundred years after the introduction of the indentation hardness testing technique by Brinell [3] it is still a topic of great scientific and engineering interest. The distinguishing feature between the early years of this technique and its contemporary use is the size of the indentations. Today, hardness indentations can be performed to depths as small as some *nano*meters.

Why do we need to be able to measure the hardness on the "dwarfs"-scale[1]? There are two main reasons: The first is the ongoing miniaturization of components, *i.e.* the ability to manufacture smaller and smaller components and thus smaller functional systems. This system miniaturization is powered by enhancements in performance and efficiency; for some applications, *e.g.* medical tools for intrusive surgery, reduced device size is its own virtue. The second reason is the tailored engineering of the near-surface properties of components. The importance of surface engineering relies on the fact that the surface of a component encounters service conditions that are different from that of the bulk. For example, the body of a turbine blade must be strong, tough and creep-resistant, while its surface must be refractory and oxidation-resistant. In the current engineering praxis, however, a component is usually made of a homogeneous material chosen from a menu of a wide number of available materials. Surface engineering provides means to alter the properties near the surface of a component without affecting its bulk properties. Two possibilities exist: surface coating and surface modification. Surface coatings are often used to enhance the tribological properties of tools or components. For example, the surface of a magnetic hard disk is protected by an about 5 nm thick diamond-like carbon coating. Obviously, to characterize the hardness of such thin protective coatings very small indentations are necessary — the same is true for the analysis of very small homogeneous components. The technique that allows the measurement and the evaluation of the hardness on such a small scale is introduced and reviewed critically in Chapter 1 of this dissertation.

It is now well known that abrupt transitions in materials composition and properties as in coated components can result in sharp concentrations of stress along the interface, causing the coating to detach during service. It is also known that these stress concentrations are greatly reduced if the transition is made gradual [4]. Those gradual transitions can be produced using a wide spectrum of surface modification techniques, including techniques that produce microstructural variations only (*e.g.* shot peening, laser or electron beam surface hardening) and techniques that produce microstructural and compositional variations as well (*e.g.* nitriding, ion implantation). Since the mechanical properties of a material depend on its composition and its microstructure, variations in composition and/or microstructure result in a corresponding property variation.

Since the 1970s ion beam implantation is used to improve the near-surface mechanical properties (tribological, fatigue resistance) of metals and alloys [5]. In ion implantation, high-energetic ions are implanted into the surface of the sample. As a result, composition and microstructure of the near-surface region of the sample are

---

[1] *Nano* is the old greek word for dwarf.

changed. Typical thicknesses of implanted regions are of order 500 nm, or less. Within an implanted region, the distributions of the implanted ions and of the defects that have been generated during ion implantation are not homogeneous, but show large variations with depth. In order to tailor the mechanical properties of ion-implanted surfaces, it is necessary to understand both the effect of ion implantation parameters on the compositional and microstructural variations within the implanted region on the one hand and the relation among property, composition, and microstructure within this region on the other hand. The aim of this work is the latter: the examination of, and the relation among, the depth-dependent variations of the mechanical properties, the composition, and the microstructure within the ion-implanted region. Because of the large gradients within the implanted region the measurements must be made with a depth resolution of some nanometers. While Auger electron spectroscopy and cross-sectional transmission electron microscopy provide standard means for assessing changes in composition and microstructure with depth on nanometer scale, respectively, the measurement of hardness on this scale has only recently become possible with the development of the depth-sensing *nano*indentation technique (Chapter 1). In this measurement technique, a diamond tip is pressed into the material to be probed and is removed after a given maximum depth or load is reached. During this procedure, the load on, as well as the displacement of, the indenter are recorded. Depth profiles of hardness are usually measured by gradually increasing the maximally probed depth. With this method, a depth resolution of order of a few nanometers — as needed for the characterization of the variations present in an ion implanted region — can not be achieved. This is shown in Chapter 2, where the traditional and two other methods of hardness-depth profiling are compared with each other with regard to their capability to detect changes in hardness with depth, with a depth resolution on nanometer scale. For that purpose, all three methods were applied to a model system consisting of a very thin TiC film deposited onto a Ti-6Al-4V substrate.

The topic of Chapter 3 is the measurement of the hardness-depth profile of a carbon implanted region of a Ti-6Al-4V alloy and its relation to the variations of composition and microstructure with depth within this implanted region. Ti-6Al-4V is used for surgical prostheses such as artificial knees or hip joints because of its combination of high strength, high resistance to fatigue and to electrochemical corrosion, and its benign biological response [6]. In service, the Ti-6Al-4V alloy joint component moves in contact with ultra-high molecular weight polyethylene (UHMWPE). Unfortunately, the friction and wear behaviour of Ti-6Al-4V is unsatisfactory, even when rubbing against a soft material such as UHMWPE: extensive wear and blackening of the Ti-6Al-4V balls and the polymer cups has been observed [6]. Ion implantation into Ti-6Al-4V has been shown to significantly reduce the wear of Ti-6Al-4V against UHMWPE [1]. Although this is often attributed to an increase in surface hardness due to ion implantation [7], a direct relation among hardness, composition, and microstructure within the implanted region could, because of the low depth resolution of the hardness-depth profile, not been made until now. The results shown in Chapter 3 provide the first of such a relation on nanometer scale.

The present dissertation is based on work performed at the institute for materials science of the Max-Planck Institut für Metallforschung in Stuttgart, Germany. This work would not have been possible without the help of many people to whom I owe a great debt of gratitude. First of all I wish to thank Prof. E. J. Mittemeijer and Prof. M. Rühle for supporting this work. I thank Prof. E. J. Mittemeijer also for many valuable discussions throughout the time I worked in his group, for critical readings of several versions of the drafts and for writing the main opinion of this thesis. Prof. M. Rühle deserves thanks for his interest in this work and for writing the secondary opinion of this thesis. My special thanks are due to the advisors of this work: Dr. B. Baretzky and Prof. S. P. Baker of Cornell University. I owe a lot of deeper insights to them and am grateful for reading and commenting critically the drafts. I am especially grateful to Prof. S. P. Baker for keeping in touch after he moved to Cornell University, for unnumbered emails and facsimile-pages with valuable suggestions and comments. Many other individuals have helped me in various ways. Partly, this is acknowledged in the text. Mostly, however, those individuals remain unnamed. To all of them, especially to the latter, I am greatly indebted.

Stuttgart, 27th April 2000   Maik Kunert

Chapter

1

Hardness testing on nanometer scale: An introduction

Abstract: Depth-sensing indentation testing is a widely used tool for measuring the mechanical properties of thin films and small volumes of materials. This chapter presents an introduction into this testing technique, including a presentation of the testing machine and a review of the analysis method used in this work. Special attention is devoted to indentation testing on nanometer scale. The problems that arise for testing on this scale are discussed and the corresponding limitations are outlined. The necessity of a clear definition of the term *hardness* is emphasized. Finally, the need for, and the realization of, highly lateral resolved hardness measurements is discussed.

1.1 Hardness testing: then and now

The testing of the mechanical hardness of a material is probably one of the oldest testing procedures of mankind. Our ancestors probably quickly learned how to distinguish between hard and soft stones. Possibly, they scratched one stone with another to test which one is more suitable for making tools or arms. Later, Friedrich Mohs (1773-1839) [8], a German mineralogist, used this technique to devise a relative hardness scale of minerals, the Mohs scale. In this scale ten common minerals are arranged in order of increasing hardness and are assigned with numbers: talc (1), gypsum (2), calcite (3), ..., corundum (9), and diamond (10). The hardness of a mineral is obtained by determining which mineral in the Mohs scale will scratch the specimen. Nowadays, in materials science the scratch test is used to determine the adhesion strength of thin films on substrates.

The indentation hardness test was introduced at Paris International Exposition (1900) by the Swedish metallurgist Johan August Brinell (1849-1925) [3]. In a Brinell hardness test, a hard sphere is pressed into the surface of the specimen and, after some time, is removed. The hardness is then defined as the ratio of the applied load to the area of the residual imprint, which is traditionally determined by optical microscopy. As in case of the scratch test, the indentation hardness test, albeit not in a quantitative manner, has been used in everyday life long before. As an example we may think of the genuineness test of coins: using the hardest material of the human body, the (dental) enamel, as an indenter, the hardness of the coin is checked by an indentation test. Together with its colour, the hardness served as a criterion for the composition of the alloy used for making this coin.

Since the times of Brinell the principle of indentation hardness testing did not change. The Brinell test and its derivatives (Vickers, Knoop, Rockwell, ...) are now standard means for quality control in industry. During the last decades, people became interested in the mechanical properties of ever smaller volumes, for example of thin films or of single phases in a multiphase alloy. Obviously, for investigating smaller details smaller indentations are necessary. Today, hardness measurements are performed with indentation depths on the order of some nanometers. The determination of the remaining imprint area of such small indentations is not possible with traditional optical microscopy because of a too low resolution. The application of scanning electron microscopy (SEM) is limited due to difficulties in relocation of the imprints and a too low topography contrast for very small imprints. Hardness testing at such small indentation depths are therefore performed and evaluated using the so-called depth-sensing indentation technique which obviates the need for imaging the remaining imprint in order to determine the indentation hardness value.
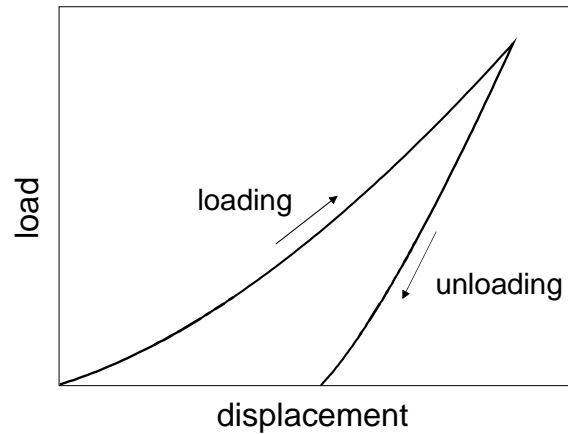
Figure 1.1: Schematic of a load-displacement curve as obtained from a single depth-sensing indentation hardness test. During loading, an indenter tip is pressed into the material until a given load or depth is reached. When the applied load is reduced, the indenter experiences some elastic recovery of the indent, causing the displacement to decrease during unloading.

1.2 Depth-sensing indentation hardness testing

In a depth-sensing indentation hardness test (DSI)[1] a diamond tip is pressed into the sample surface and, subsequently, after having reached a given maximum depth or maximum load, the tip is removed. During this procedure, the load on, as well as the displacement of, the indenter are recorded. The result of such an experiment is therefore not only a hardness value – as in the Brinell hardness test – but the complete history of the deformations occurring during the test, as saved in the so-called load (P)-displacement (h) curve (Fig. 1.1). A load-displacement curve consists of a loading and of an unloading curve. The loading curve characterizes the resistance of the sample against the penetration of the tip into the material and reflects both the elastic and the plastic properties of the tested material. The unloading curve is mainly determined by elastic recovery of the indent. From such a load-displacement curve hardness and Young's modulus of the specimen can be determined using an appropriate analysis model. Thus, two prerequisites are necessary for a successful application of the DSI technique: an apparatus capable of performing indentation experiments while simultaneously recording the applied load and the corresponding displacement of the indenter *and* a method for the analysis of the measured load-displacement curves. For an overview on DSI apparatuses see Ref. 9, pp. 324–348. The apparatus used in this work is described in the next section, followed by a section describing the analysis of load-displacement curves.

---

[1] Depth-sensing indentation, instrumented indentation, continuously recording indentation technique, mechanical properties microprobe, dynamic hardness testing, ultra-low-load indentation – all these names are used interchangeably in literature for the same testing technique. If indentations are performed in the nanometer depth range it is usually referred to as *nano*indentation.
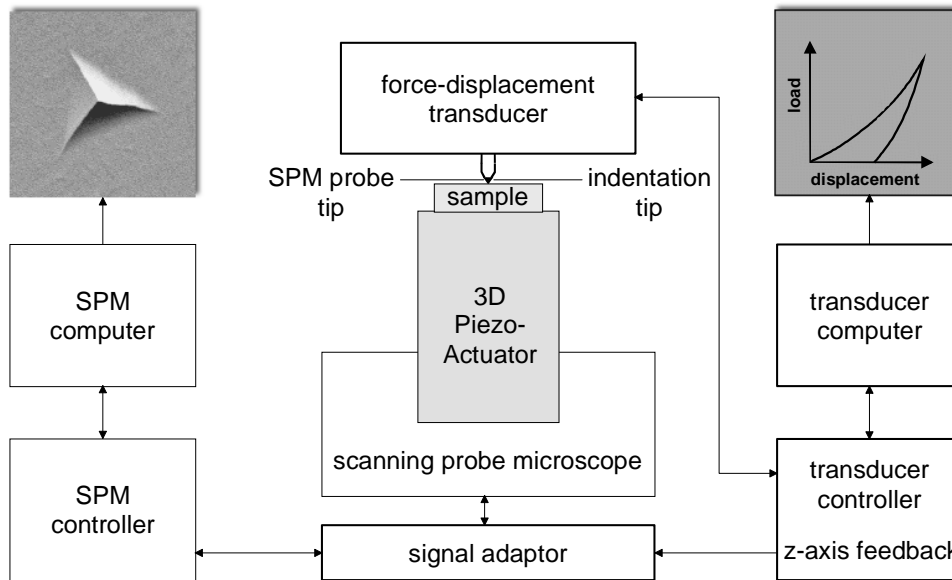
Figure 1.2: Schematic of the TriboScope in use with a scanning probe microscope (SPM). The parts belonging to the TriboScope are marked with thicker lines. The combination of a depth-sensing indentation apparatus with a SPM yields both load-displacement curves and images of the indents made.

1.2.1   The Hysitron TriboScope : Part I. A nanoindenter

The Hysitron TriboScope is an add-on DSI system to a commercial scanning probe microscope[2] (SPM), consisting of a force-displacement transducer, a transducer controller, and a computer (see Fig. 1.2). The combination of a DSI system with a SPM has a symbiotic effect: it extends the SPM in the capability of making DSI experiments with a high load and depth resolution (100 nN and 0.2 nm, respectively), and it enables the DSI system to take scanning force images of the sample surface by using the same diamond tip for imaging and for indentation. The advantages of the imaging capability will be discussed in section 1.6.2. Now we will focus on the indentation aspects.

The heart of the TriboScope is a three plate capacitive force-displacement transducer (Fig. 1.3). It consists of two fixed drive plates and a pick-up electrode, which is spring mounted to the housing. The diamond tip is mounted to the pick-up electrode, which can move up and down. To perform an indentation, an electrostatic force is generated between the pick-up electrode and a drive plate. The amount of this force, F_{el}, is proportional to the square of the voltage applied to the drive plate, V [10]:

$$F_{el} = k_e \cdot V^2 \ . \tag{1.1}$$

Here, k_e is an electrostatic force constant, which depends on the plate area and the distance between drive plate and pick-up electrode. It is determined by the manufac-

---

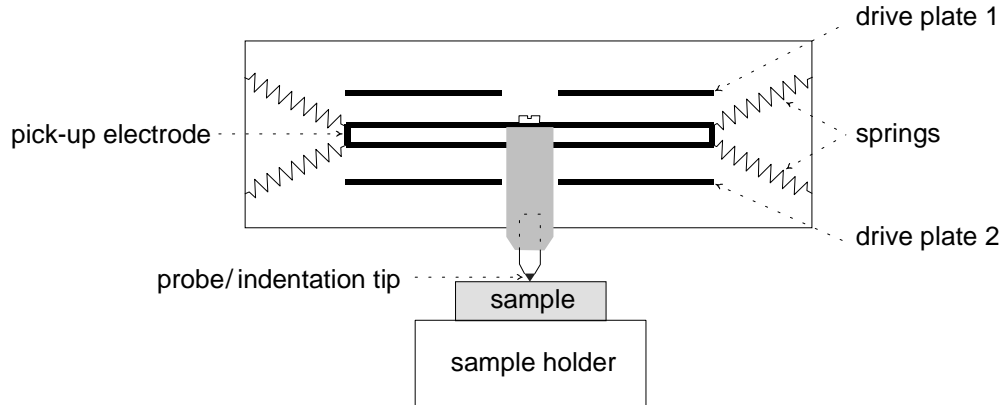[2] In this work a NanoScope III MultiMode (Digital Instruments) was used.

Figure 1.3: Schematic of the three plate capacitive force-displacement transducer of the Hysitron TriboScope.

turer and is supplied with the transducer. Using k_e, the force-time scheme set by the operator is translated by the control software [11] into a voltage-time scheme which is than applied to the transducer. The displacement is measured capacitively. A typical loading-unloading cycle of an indentation experiment is shown in Fig. 1.4. This cycle contains a zero-load segment, which is used to determine the thermal drift rate, a loading, and an unloading segment. During the experiment, the load on, and the displacement of, the indenter are measured as a function of time. From the load-time and the displacement-time plots, the corresponding load-displacement curve is obtained.

This load-displacement curve does not, however, represent the mechanical behaviour of only the investigated material for two reasons:

(1) A part of the electrostatically generated force is supported by the suspension springs of the pick-up electrode. This part must be subtracted from the electrostatically applied force to obtain the actual force applied to the sample, F_s: $F_s = F_{el} - k_s \cdot h$. Here, h is the displacement of the pick-up electrode and k_s is the spring constant of the suspension. The latter can be determined by making an indentation in air, *i.e.* an indentation for which $F_s = 0$. For the transducer used in this work, a spring constant of 160 N/m has been determined (Fig. 1.5).

(2) The apparatus used for performing an indentation test is not ideally stiff. The measured displacement of the indenter tip is therefore the sum of the indentation depth of the tip in the specimen and of the displacement associated with elastic deformation of the apparatus, referred to as load-frame compliance. In order to obtain the load-displacement curve that characterizes the response of only the investigated material, the load-frame compliance must be known. To understand the procedure of determining the load-frame compliance of the apparatus some details of the data analysis must be introduced. This procedure will therefore be presented in section 1.2.3.
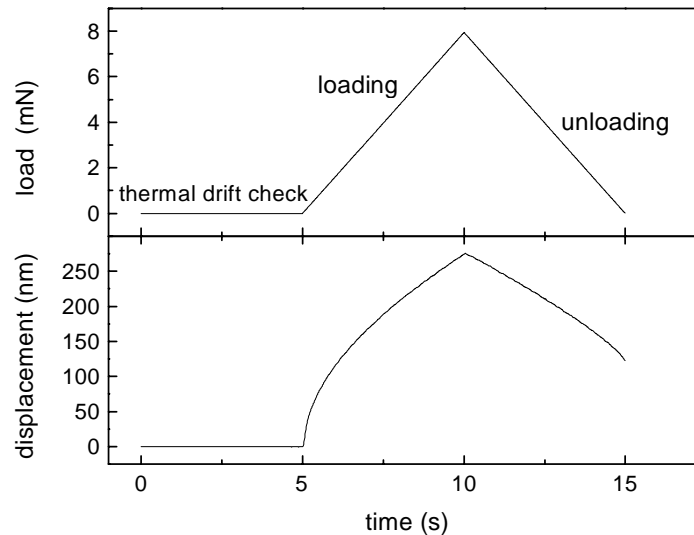
Figure 1.4: Typical load-time scheme of an indentation experiment (above) and the corresponding displacement measured as a function of time.

More details about structure and operation of the Hysitron TriboScope can be found in Refs. 10 and 12.

1.2.2   The load-displacement curve as a mechanical-property fingerprint

Two extremes limit the mechanical behaviour of materials: the ideal elastic and the rigid-plastic behaviour. The stress-strain diagrams, together with the corresponding load-displacement curves and schematic presentations of the surface deformations, are given in Fig. 1.6. In case of an ideal elastic behaviour, no plastic deformation within the sample takes place. The stress induced by the indenter is stored in the sample in form of elastic strain energy, which is completely recovered during unloading: the loading and unloading curves coincide and, thus, no permanent imprint remains in the sample after the indenter has been removed.

When a rigid-plastic material is indented, no elastic deformation occurs. The induced stress is completely relieved by plastic deformation. As no elastic strain within the sample is developed, no recovery during the unloading cycle takes place: the displacement at maximum load equals the displacement after complete unloading.

Most engineering materials, however, exhibit an elastoplastic behaviour and their load-displacement curves lie in between the extremes of ideally elastic and rigid-plastic materials (see Figs. 1.6 and 1.7). The loading curve of an indentation into an elasto-plastic material is determined by both elastic and plastic deformation of the specimen. Several attempts have been made to separate the influence of both to obtain hardness and modulus from the loading curve [13–15]. Others [13, 16, 17], for characterization
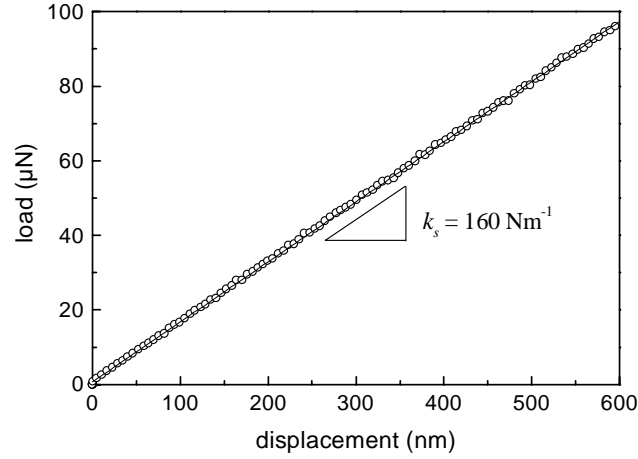
Figure 1.5: Loading curve of an indentation made in air.

of the mechanical properties of the specimen, use the work necessary for the creation of the indent and the work released by the specimen during unloading, given by the area under the loading and under the unloading curve, respectively. Most of the time, however, the unloading behaviour of the specimen is used for the analysis of load-displacement curves [2, 13, 18]. In this work, the analysis method proposed by Oliver and Pharr [2] is used.

1.2.3   Analysis of a load-displacement unloading curve: the method of Oliver and Pharr

Foundations
The roots of the Oliver and Pharr (O&P) analysis method go back to a work of Sneddon [19], who derived the relation among load, displacement, and contact area for a contact of an isotropic elastic half space by rigid indenters of various geometries. The contact stiffness, S, is defined as an increment in load divided by the resulting increment in displacement in absence of plastic deformation,

$$S \equiv \frac{dP}{dh}\bigg|_{elastic} , \tag{1.2a}$$

i.e. it corresponds with the slope of the initial unloading curve and can be calculated from [19]:

$$S = \frac{2}{\sqrt{\pi}} \cdot \frac{E}{1 - \nu^2} \sqrt{A_c} . \tag{1.2b}$$

Here, E is Young's modulus and ν is the Poisson ratio of the investigated material; A_c is the projected contact area at maximum load. Eq. (1.2b) is only valid if an ideally rigid
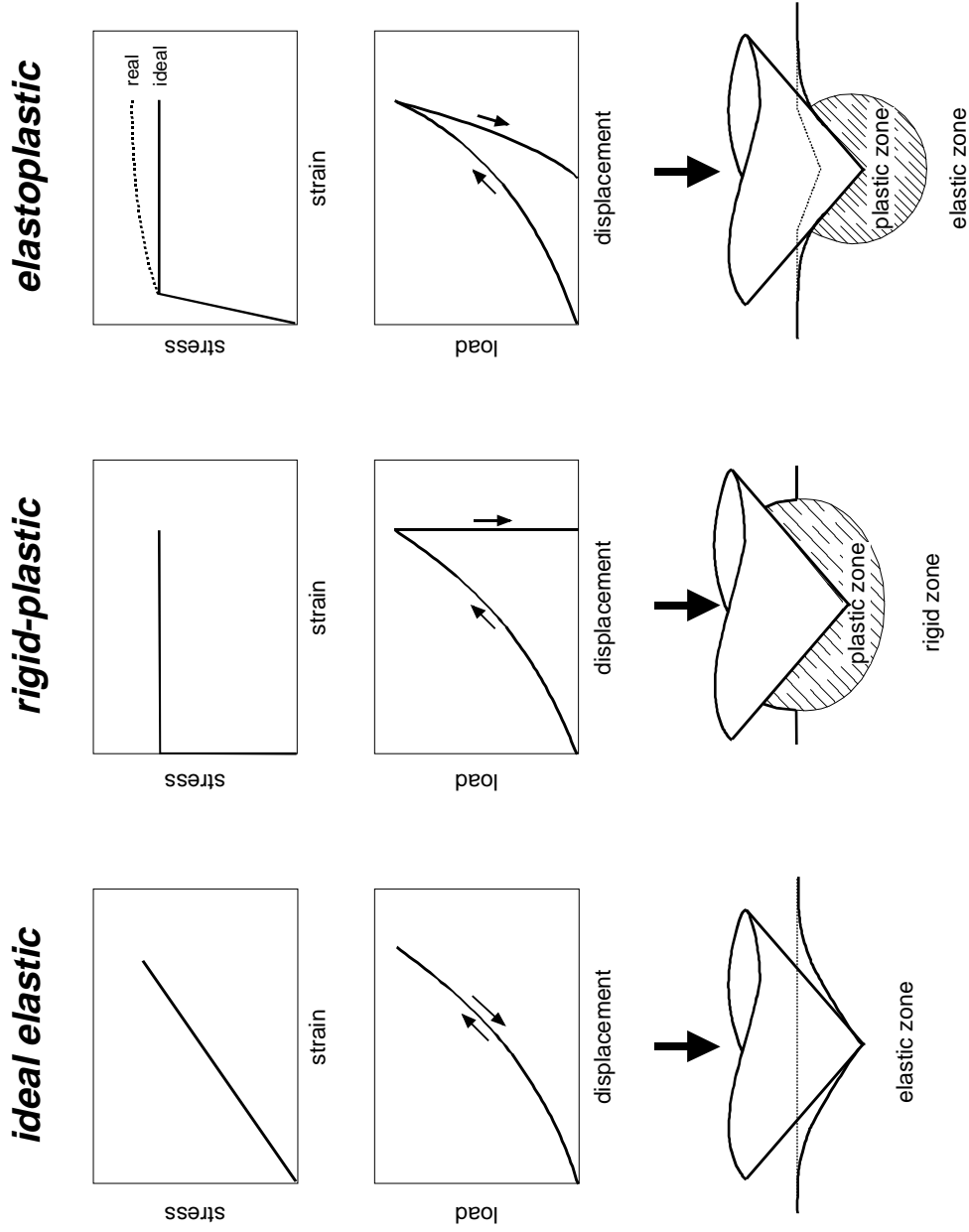
Figure 1.6: Schematic presentation of stress-strain diagrams, load-displacement curves, and surface profiles at maximum load (full lines) and after complete unloading (dotted lines) for ideal elastic, rigid-plastic, and elastoplastic materials. Plastic deformation is a volume-conservative process. Thus, all of the material displaced by the indenter must be accommodated either by an upward extrusion ("pile-up") around the indent (rigid-plastic materials) and/or by elastic compression (elastoplastic materials).
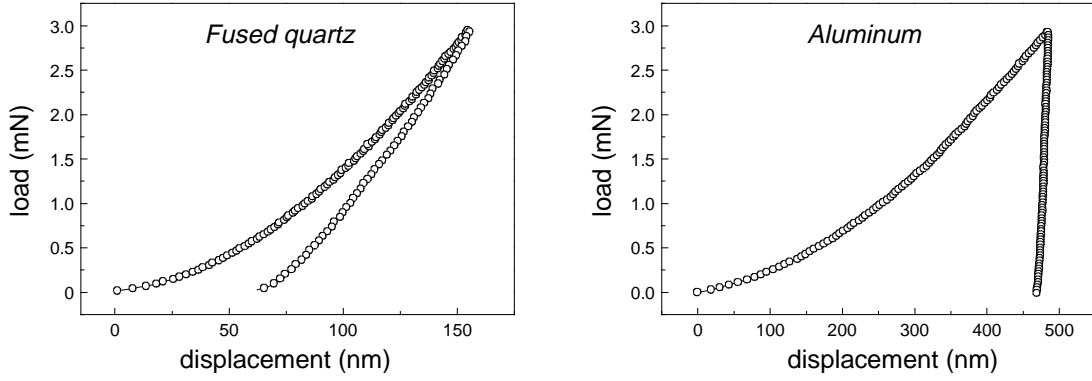
Figure 1.7: Load-displacement curves for fused quartz, showing a pronounced elastic recovery, and for an easily plastically deformable material like aluminum

indenter is assumed. This assumption does not hold, in particular if very stiff materials, like *e.g.* ceramics, are investigated. To account for the finite elastic deformation in the indenter, an additional term is necessary. Assuming that indenter and specimen behave like springs in series, the elastic deformation of both can be characterized by a single "reduced modulus", E_r [20]:

$$\frac{1}{E_r} = \frac{1 - \nu_i^2}{E_i} + \frac{1 - \nu^2}{E} \; , \tag{1.3}$$

where E_i and ν_i are Young's modulus and Poisson ratio of the indenter material, respectively. For the diamond indenters used in this work $E_i = 1141$ GPa and $\nu_i = 0.07$ were taken [2]. Using Eq. (1.3), the tip-sample contact can now be modelled as one between a rigid indenter and an isotropic half space with the modulus E_r, and the stiffness can be calculated using [19]:

$$S = \frac{2}{\sqrt{\pi}} \cdot E_r \cdot \sqrt{A_c} \; . \tag{1.4}$$

This equation is called the *canonical Sneddon stiffness equation.* Together with Eq. (1.3) it can be used to evaluate elastic properties of the specimen: the Young modulus, E, if the Poisson ratio is known, or the indentation modulus, $I = E/(1 - \nu^2)$, if not.

The hardness, H, is defined as [18]:

$$H \equiv \frac{P_{max}}{A_c} \; , \tag{1.5}$$

where P_{max}, the maximum applied load, is read off directly from the load-displacement curve.

Thus, two quantities remain to be determined for the evaluation of hardness and Young's/indentation modulus of the specimen: the contact stiffness, S, and the projected contact area at maximum load, A_c. It is the aim of the Oliver and Pharr analysis
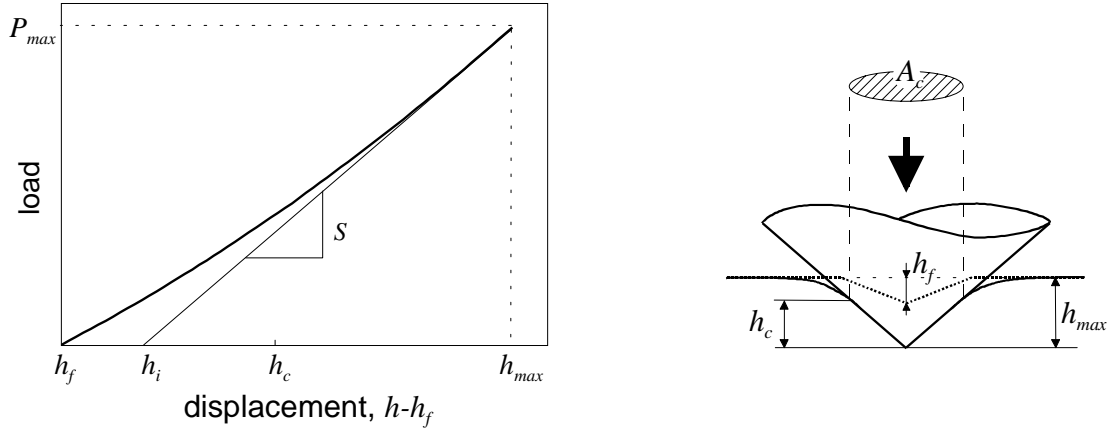
Figure 1.8: An unloading curve showing quantities used in the analysis and a schematic of the section through an indentation at maximum load (full lines) and after removing the load (dotted lines) (h_f = residual imprint depth, h_i = intercept depth, h_c = contact depth, h_{max} = maximum indentation depth, P_{max} = maximum applied load, S = contact stiffness).

method to provide a comprehensive tool for the estimation of both these quantities from the unloading curve of a DSI experiment.

Contact stiffness

The contact stiffness, S, is determined in two steps:

(1) A fraction of the unloading curve is fitted with $P = \alpha (h - h_f)^m$, where h_f is the residual imprint depth, and α and m are fitting parameters. In this work the unloading data from 40–95% of the maximum load were used for fitting [21]. At higher loads creep effects can influence the shape of the unloading curve and at lower loads geometry (tip shape) effects may come into play.

(2) The unloading curve fit is differentiated analytically to determine the slope at maximum load: $S = (dP/dh)_{P=P_{max}}$.

Projected contact area

The projected area of a contact between indenter and sample at maximum load is determined by the geometry of the indenter and the depth of contact, h_c, *i.e.* the distance along the indenter axis that the indenter is in contact with the sample (see Fig. 1.8). Sneddon's analysis for the elastic displacement of the surface outside the contact perimeter, $h_{max} - h_c$, gives [19]:

$$h_{max} - h_c = \varepsilon \cdot \frac{P_{max}}{S} \, , \tag{1.6}$$

where the constant ε depends on the geometry of the indenter. By rewriting Eq. (1.6) the contact depth, h_c, is obtained [2]:

$$h_c \;=\; h_{max} - \varepsilon \cdot \frac{P_{max}}{S} \;, \tag{1.7a}$$

or equivalently

$$h_c \;=\; h_{max} - \varepsilon \cdot (h_{max} - h_i) \;. \tag{1.7b}$$

Here, h_i is the intercept of the initial unloading slope with the displacement axis. For the geometry factor, ε, O&P observed that for a Berkovich indenter and a wide range of materials, a value of about 0.75 is appropriate [2]. Therefore, this value of ε is used throughout this dissertation.

From Eq. (1.7) we know the depth of contact at maximum load, but what we need is the corresponding projected area. The relation between these values is described by the so-called tip shape area function $A_c = f(h_c)$. However, before determining the tip shape area function, remember that the measured displacement of the indenter consists of three parts: the elastic and/or plastic deformation of the specimen, the elastic deformation of the indenter, and the elastic deformation of the load frame of the apparatus. The elastic deformation of the indenter has been accounted for by introducing the reduced modulus, E_r. To obtain the response of only the specimen, the elastic deformation of the load frame must also be subtracted from the measured displacements. To determine the compliance[3] of the load frame, we assume that load frame and specimen can be modeled as two springs in series. The total compliance, c_{tot}, is then

$$c_{tot} = c_f + c_s \;, \tag{1.8}$$

where c_s is the compliance of the specimen and c_f is the compliance of the load frame. Using $c_s = 1/S$ and Eq. (1.4), Eq. (1.8) can be rewritten:

$$c_{tot} = c_f + \frac{\sqrt{\pi}}{2} \cdot \frac{1}{E_r \cdot \sqrt{A_c}} \;. \tag{1.9}$$

From this equation it follows that a plot of c_{tot} *vs.* $1/\sqrt{A_c}$ gives a straight line if E_r is assumed to not depend on the indentation depth. The slope of this line is proportional to $1/E_r$, and the intercept of the line with the ordinate defines the load-frame compliance. It is obvious from Eq. (1.9), that the contribution of the load-frame compliance to the total compliance increases as the value of the second term on the right hand side decreases. This is achieved either by increasing the contact area (*i.e.* by increasing the maximum load) or by investigating very stiff materials.

For the determination of the load-frame compliance, large indentations are made in a single crystal of aluminum, which was chosen because of its elastic isotropic behaviour. The projected contact area of these indentations was determined in two ways:

---

[3] For purely elastic deformation, the compliance is just the inverse of the stiffness.
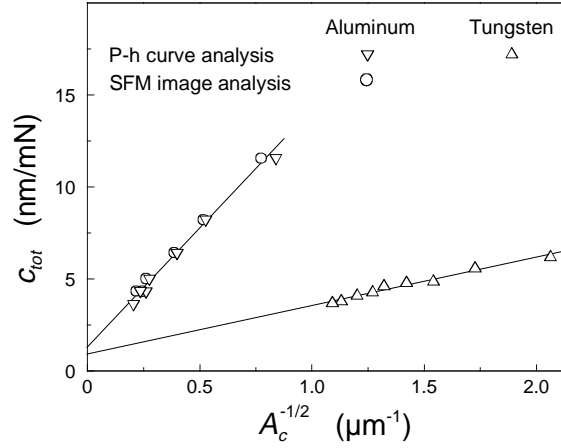
Figure 1.9: Plot of the total compliance, c_{tot}, *vs.* the reciprocal square root of the projected contact area, $1/\sqrt{A_c}$, for aluminum and tungsten

(1) The projected contact area was determined using the O&P-method described above and assuming an ideal tip shape, *i.e.* $A_c = 24.5 \cdot h_c$ for a Berkovich indenter (see appendix, p. 30). The assumption of an ideal tip shape is reasonable for large indentations (*cf.* section 1.5.1).

(2) The residual imprints were imaged using scanning force microscopy and the projected areas were directly obtained from these images. The difference between the projected contact area at maximum load and the projected area of the imprints after unloading, for large indentations in pure aluminum, is negligible.

The areas determined using the two methods agree well with each other (see Fig. 1.9). The load-frame compliance of our TriboScope/MultiMode system is $1.24 \cdot 10^{-6}$ m/N. A similar small value ($1.005 \cdot 10^{-6}$ m/N) was obtained with a single crystal of tungsten.

Once the load-frame compliance is known, the tip shape area function can be determined. To do so, a series of indentations at various maximum loads are performed on a fused quartz specimen. For the tip shape calibration, fused quartz is preferred to aluminum, because the latter is much softer (250 MPa as compared to 9.5 GPa for fused quartz [2]) and small indentations in aluminum are difficult to obtain. Furthermore, fused quartz behaves elastically isotropically and its elastic constants are well known ($E = 72$ GPa, $\nu = 0.170$; *i.e.* for diamond indenters: $E_r = 69.6$ GPa). The projected contact areas of the indentations are determined by rearranging Eq. (1.9):

$$A_c = \frac{\pi}{4} \cdot \frac{1}{E_r^2 \cdot (c_{tot} - c_f)^2} \ , \tag{1.10}$$

and are plotted versus the contact depth. Then, the tip shape area function is obtained by fitting the (A_c, h_c) data to a polynomal of the form

$$A_c = a_0 h_c^2 + a_1 h_c + a_2 h_c^{1/2} + a_3 h_c^{1/4} + a_4 h_c^{1/8} + a_5 h_c^{1/16} \ , \tag{1.11}$$

where a_i are fitting constants. Now, by inserting the contact depth from Eq. (1.7) into the determined tip shape area function (Eq. (1.11)) the projected contact area of a particular indentation is obtained. The corresponding hardness is derived by substitution of A_c into Eq. (1.5) and the Young's or indentation modulus can be calculated from Eq. (1.4).

In the last sections we have seen how an indentation is performed and how the experimental result of such an indentation, the load-displacement curve, is analyzed to yield modulus and hardness of the specimen. In the next section the meaning of the such derived hardness value will be discussed.

1.3   The meaning of indentation hardness

The indentation hardness of a solid is usually understood to mean its local resistance to plastic deformation [22]. This is true as long as the traditional definition of hardness is used, *i.e.* the definition introduced by Brinell. In this traditional definition, the hardness is obtained by dividing the applied maximum load by the remaining surface area of the imprint *after* unloading. Accordingly, the indentation hardness of an ideal elastic material, for which the remaining imprint area is zero, would be infinite.

If, instead, the definition given in Eq. (1.5) is used for determination of the indentation hardness, the restriction to only plastic deformations is lifted. Since this definition uses the contact area *at maximum load*, all materials, including ideal elastic ones, will have a finite value of indentation hardness. Unfortunately, this "contact" hardness does not have a clear meaning regarding the kinds of deformation involved in the analysis; rather it depends on the ratio of the Young modulus (E) to the yield stress (σ_y) of the material investigated. For materials with large E/σ_y (*e.g.* pure metals) the contact between the indenter tip and the deformed sample surface may be purely plastic, for materials having small E/σ_y (*e.g.* rubber) purely elastic contacts may occur, and the contact with materials having moderate E/σ_y (*e.g.* ceramics) may be of mixed elasto-plastic nature [21].

The value and the meaning of the "contact" hardness may, for a given elastoplastic material, also change with the applied load. Imagine a spherical indenter being pressed into the surface of a sample[4]. At small applied loads and thus small stresses the resulting strain in the sample and, hence, the contact between indenter and sample are of purely elastic nature. When the load is increased beyond a certain value, the stresses induced by the indenter will exceed the critical shear stress of the specimen and a part of the strain is relieved by plastic deformation. An elasto-plastic state is reached. At this stage the plastic flow is constrained, *i.e.* the plastically deformed zone is surrounded by elastic material that impose a certain constraint on the plastically deformed zone. To further expand the plastic boundary into the elastically deformed material the applied

─────────────────────

[4] As will be shown in section 1.5.1 all real indenter tips are rounded to some extent at their apexes.

stress needs to be maintained[5] and thus the load on the indenter must be increased. Doing this, the plastically deformed zone grows and, eventually, it breaks out to the free surface. Then, the indenter is completely in contact with plastically deformed material; a plastic contact is formed. Obviously, there is a transition from a purely elastic to a fully plastic contact and hence the hardness obtained from the projected *contact area* at maximum load characterizes the local resistance of the investigated material against elastic *and/or* plastic deformation.

If the state of a completely plastic contact is reached, the indentation hardness of a material is directly proportional to its uniaxial tensile yield stress [22]:

$$H = c \cdot \sigma_y \,, \tag{1.12}$$

where c, the constraint factor, depends on the ratio E/σ_y of the material. For small E/σ_y, *e.g.* for polymers ($E/\sigma_y \approx 10$), the constraint imposed by the surrounding elastic material on the expansion of the plastically deformed zone is small and the indentation hardness is only a little greater than the yield stress: $c \lesssim 1.5$ [23]. For most metals, for which $E/\sigma_y \gtrsim 100$, the constraint factor has a value of $c \approx 3$ [22]. It should be emphasized here, that the above Tabor relation holds only if a completely plastic contact is reached. Only in this case, the value of the "contact" hardness can be related to the uniaxial tensile yield stress and is comparable with hardness values obtained from traditional hardness tests.

The above discussion made clear that the indentation hardness is not a fundamental material property. Rather it depends on the way it is obtained (testing technique, evaluation, ...). Despite of this, the indentation hardness is widely used as a parameter for characterizing the mechanical properties of materials, in particular of metals, for several reasons: indentation hardness tests are relatively easy to perform and provide a value that gives a direct measure for the load-bearing capacity of the investigated material. Moreover, for completely plastic contacts the hardness of a material also gives an indirect measure of its uniaxial tensile yield stress. Another reason for the widespread application of hardness tests is closely connected with the definition of indentation hardness as a *local* measure of the mechanical properties: currently, there is no other method that is able to quantitatively determine the mechanical properties of a sample with a local resolution that is comparable with that of, in particular, DSI tests. In the next section we, therefore, will take a look on what determines the resolution of an indentation experiment and will provide some means for its estimation.

Remark: In this work mainly the "contact" hardness of a material has been determined. Therefore, unless not otherwise noted, the term hardness will be used as synonym for the "contact" hardness throughout this dissertation.

---

[5] If work hardening is crucial the applied stress even needs to be increased.

1.4   The volume sampled during an indentation hardness test

From the description of the expansion of the plastically deformed zone during an indentation (see last section) it is obvious that the measured hardness characterizes the mechanical properties of a certain volume of material. The knowledge of the extent of this sampled volume is important for all indentation experiments. For example, the lateral extent of the influence zone determines the minimum distance between two indentations that is necessary to avoid an influence of the first indentation on the second one. Sometimes the extent of the influence zone has to be adjusted to the measuring problem, *e.g.* if the hardness of a single grain is to be determined without being influenced from the grain boundaries, the sampled volume must be smaller than the size of the grain. On the other hand, if the effect of the grain size on the strength of a material is the matter of investigation, of course, the influence zone should be large enough to include several grains.

Unfortunately, the stress field that develops underneath the indenter is very complex and an analytic solution has not been achieved. However, the evolution of the plastic zone during an indentation resembles the expansion of a spherical cavity in an infinite elastic-plastic solid by an internal pressure, a problem for which a solution is available [26]. Based on this solution, several models have been developed to estimate the dimension of the plastically deformed zone [24, 27–29]. A widely accepted analysis is based on the core model devised by Johnson [24]. In this model, the spherical cavity is replaced by a hemispherical core that encases the surface of the indenter (see Fig. 1.10). Within the core a hydrostatic pressure is assumed. The stresses and displacements outside the core are assumed to have radial symmetry. With these assumptions the ratio of the plastic zone radius to the contact radius, r_{pl}/r_c, is determined [24, 30]

$$\frac{r_{pl}}{r_c} = \left[\frac{E \cdot \tan\beta}{6\sigma_y(1-\nu)} + \frac{2(1-2\nu)}{3(1-\nu)} \right]^{1/3} .   \tag{1.13}$$

Here β is the angle between the indenter face and the surface. In case of a fully plastic contact ($E \cdot \tan\beta/\sigma_y \gtrsim 40$ [30, p. 178]) and for a material with a Poisson ratio of $\nu = 0.3$, Eq. (1.13) locates the elastic-plastic boundary at $r_{pl}/r_c \approx 2.2$. This value has been shown to give reasonable values for the plastic zone size of indentations in materials with $E/\sigma_y \gg 200$ [31–33]. For materials with smaller values of E/σ_y, however, deviations from the model behaviour have been reported [29]. A particular limitation of the model is the uncertain nature of the hydrostatic core underneath the indenter. If the pressure within this core were truly hydrostatic, no plastic deformation within the core region would occur. This, in turn, would imply that hardness measurements can never sample the outermost surface layers [23]. The situation is well characterized by Tabor [23, p. 141] who pointed out that "the expanding cavity model ... is an extremely helpful and fairly realistic description of the indentation process ... It must, however, not be pushed too far."
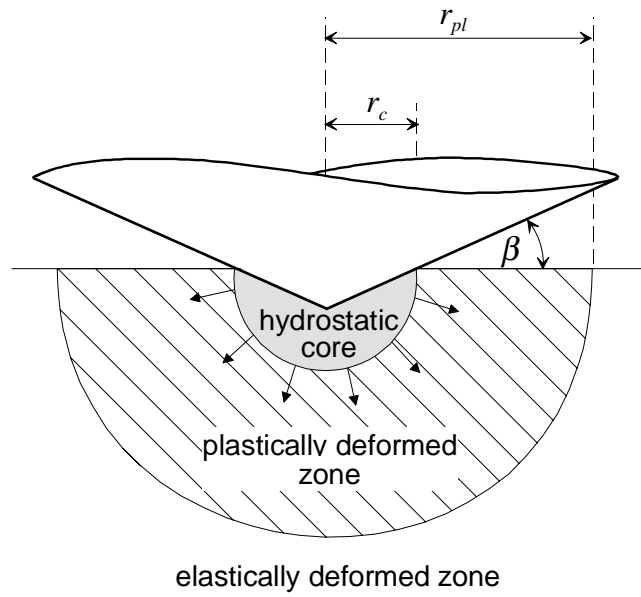
Figure 1.10: Cavity model of an elastic-plastic indentation by a cone [24]. (r_{pl} = radius of the plastically deformed zone, r_c = core radius, β = inclined indenter face angle)

Figure 1.11: (a) Computed cross sections of the plastic zones for elastic-perfectly plastic (solid line) and elastic-work hardening (dotted line) materials for $E = 70\,\text{GPa}$, $\nu = 0.25$, and $\sigma_y = 840\,\text{MPa}$ ($E/\sigma_y = 83$) and (b) the ratio r_{pl}/r_c in dependence of E/σ_y [25].

Figure 1.12: Computed plastic zone of indentations into an aluminum alloy having different states of stress [34].

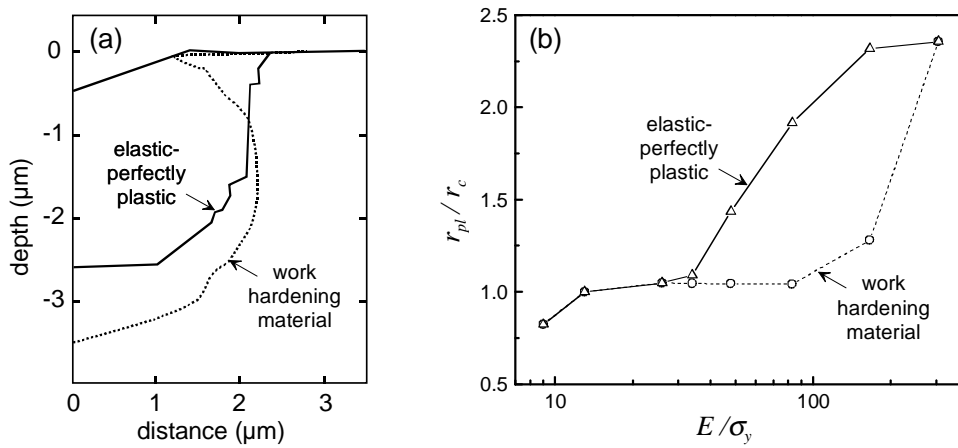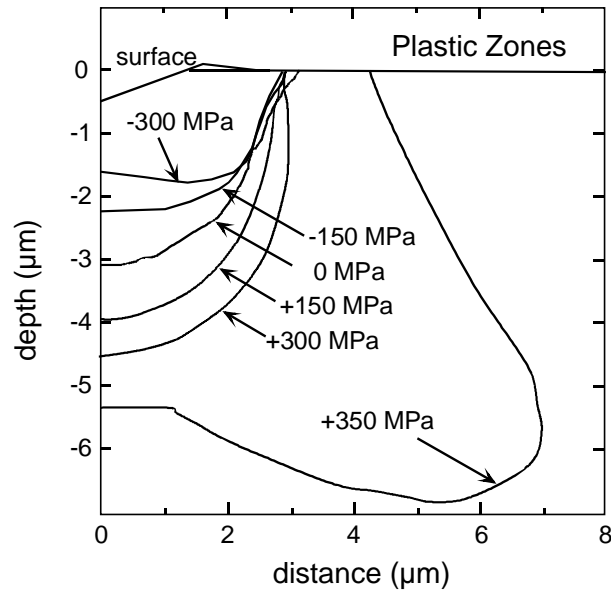Another approach to the analysis of an elastoplastic indentation is the finite element technique. Performing such an analysis, Bolshakov [25] found distinct differences in the lateral as well as in the vertical extent of the plastically deformed zone for elastic-perfectly plastic materials and for materials that undergo work hardening during indentation (Fig. 1.11). For work-hardening materials, the plastic zone does not extend beyond the radius of contact in the surface ($r_{pl}/r_c \leq 1$) if $E/\sigma_y \lesssim 100$. For elastic-perfectly plastic materials, the plastic zone radius becomes larger than the contact radius ($r_{pl}/r_c > 1$) if $E/\sigma_y \gtrsim 30$ (see Fig. 1.11b). At the same time, the vertical extent of the plastic zone is smaller for the elastic-perfectly plastic material as compared with the material that work hardens for all ratios E/σ_y investigated (see Fig. 1.11a). Thus, the shape of the plastic zone for a given material depends on the history of the sample, *e.g.* is it in a cold worked or in an annealed state, is it mechanically ground and polished or electrochemically polished, . . .

In another finite element study [34], the influence of the state of stress on the shape of the plastic zone has been investigated. The results are shown in Fig. 1.12. The depth of the plastic zone increases as the state of stress changes from large compressive to smaller compressive to tensile. The lateral dimension of the plastic zone, however, does not change until the yield stress of the sample ($\sigma_y = 350\,\text{MPa}$) is approached [34]. Again, the shape of the plastic zone for a given material depends on the history of the sample through the residual stress state present. The state of stress in particular affects the vertical extent of the plastic zone and thus the depth resolution of an indentation test. The latter is especially important for indentation testing of thin films (see section 1.5.3).

From the above discussion it became obvious that the estimation of the plas-

tic zone size is difficult even for homogeneous materials. However, for soft metals ($E/\sigma_y > 200$) the upper limit of the Johnson model ($r_{pl}/r_c \approx 2.2$) gives reasonable values (see above, [31–33]). For materials with smaller E/σ_y an estimate of the plastic zone radius can be obtained by relating the projected contact area of the indentation to the equivalent area of a circle, *i.e.* for an ideal Berkovich indenter (see appendix) $A_c = 24.5 \cdot h_c^2 = \pi \cdot r_{pl}^2$ and thus $r_{pl} \approx 2.8 \cdot h_c$ [35]. This corresponds to a ratio r_{pl}/r_c of approximately 1.

For a deeper understanding of the evolution of the plastic zone during an indentation and thus for the development of better analysis models, further investigations are necessary. A particularly promising approach should be the combination of indentation testing and TEM investigations of the indentations made [36–39] or, even better, in-situ indentation tests [40].

1.5 Some features of hardness testing in small dimensions

Hardness values of homogeneous materials have been reported to depend on the depth of indentation [41, 42]. This effect may have several reasons. Some of them are due to experimental difficulties that arise for hardness testing at smaller indentation depths (*e.g.* the surface roughness or the tip shape at the apex); others originate in the change of characteristic length scales of the investigated material (*e.g.* the thickness of the natural oxide layer or the spacing between dislocations) relative to the dimensions of the indentations.

1.5.1 Tip shape of the indenter

Indenters with different tip shapes are used in indentation testing: spheres (in the Brinell and in the Rockwell hardness test), several 4-sided pyramids (Vickers, Knoop) and cones (Rockwell). In nanoindentation testing 3-sided pyramids are usually used, because they are easier to fabricate with sharp tips than 4-sided pyramids[6]. A compilation of some useful data of the indenter types used in this dissertation (Berkovich, cube corner) can be found in the appendix (p. 30).

Generally, all indenter tips can be assigned either to indenters with a self-similar geometry, *i.e.* indenters for which the inclined face angle β is independent of the indentation depth (cones, pyramids), or to indenters which are not self-similar (spheres). For spherical indenters the induced strain increases with increasing indentation depth. Thus, for strain hardening materials, the hardness scales with the indentation depth through strain [22]. Ideally sharp cones or pyramids produce plastic deformation in the surface for the smallest loads. Once penetration has commenced the shape of the indentation remains unchanged during the course of indentation whatever the indentation

---

[6] Three faces always meet at a point; in case of four faces the opposing sides inevitably meet at a line.
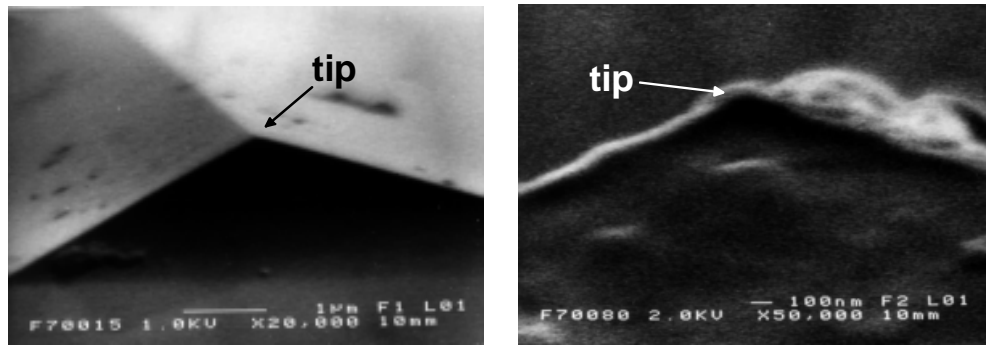
Figure 1.13: SEM images of a diamond Berkovich indenter. The image on the right hand side clearly shows a blunt indenter tip having a tip radius of approximately 100 nm.

depth is. Therefore, the hardness of homogeneous samples obtained using self-similar indenters does not depend on the indentation depth.

No indenter tip, however, is ideally sharp but is rounded to some extend at the apex (see Fig. 1.13). Well ground indenters have tip radii of order 100 nm. Thus, if indentations are made in the depth range of some nanometers the real tip shape differs considerably from the ideal one. One consequence of the deviation of the ideal tip geometry has already been discussed in section 1.3: for very small indentations the meaning of the indentation hardness may change with the indentation depth or load even for nominal self-similar indenters.

Besides the effect on the elastic-plastic transition, the tip rounding also affects the evaluation of the hardness. As illustrated in Fig. 1.14a, the assumption of an ideal tip shape leads to an underestimation of the projected contact area, and thus to an overestimation of the hardness (*cf.* Eq. (1.5)). This is shown exemplary in Fig. 1.14b: DSI experiments in fused quartz were evaluated (a) assuming an ideal tip shape and (b) accounting for the tip imperfections by using the calibrated tip shape area function. At large indentation depths, both hardnesses are equal; at these depths the tip can be considered to be of ideal shape. At smaller indentation depths, however, the hardnesses begin to deviate due to differences in the projected contact areas of the ideal and the real tip (Fig. 1.14a); the deviation increases with decreasing indentation depth. This clearly shows that for obtaining meaningful hardness values at small indentation depths, a careful calibration of the tip shape is necessary.

1.5.2   Surface roughness

The elastic contact model used for evaluation of the load-displacement curves is based on the assumption of a *single* contact between the indenter tip and a homogeneous, perfectly elastic material having a smooth surface [19]. If the surface is rough, multiple-area contacts between the indenter tip and asperities of the surface are formed instead of a single contact (see Fig. 1.15). Because the contact area of a single asperity-tip contact is small, the stress in this area is high even at a small load. As a result, the
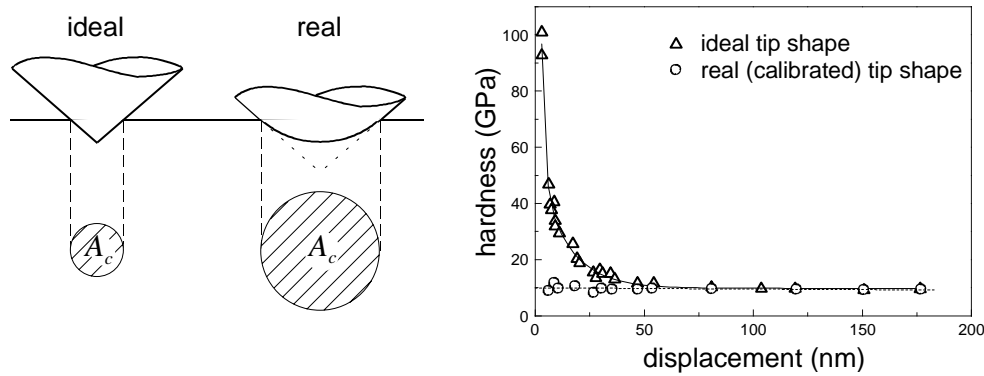
Figure 1.14: (a) Schematic presentation of the differences in projected areas for an ideal and a real tip shape. (b) Hardness of fused quartz in dependence of contact depth as obtained by assuming an ideal tip shape ($\triangle$) and by using a calibrated tip shape area function ($\circ$). The importance of a careful tip shape calibration for measurements at small indentation depths is obviously.

asperity deforms plastically at a very early stage of the indentation experiment, *i.e.* at a low load of the loading cycle, causing the load-displacement curve to cover larger displacements than in the case of a sample with a smooth surface (see Fig. 1.15). As a result, the projected contact area is overestimated and the values for hardness and indentation modulus calculated from Eqs. (1.5) and (1.4), respectively, are too small [43]. To counteract influences due to surface roughness, the indentation depth must be large relative to the roughness [22].

Characterization of the surface roughness

The topographic structure of a surface, *i.e.* the surface texture, consists of two components: roughness and waviness [44]. The roughness describes the closely spaced irregularities that are characteristic for the production process of the sample, *e.g.* the grit spacing in case of a ground surface. The waviness is often due to machine or sample vibrations during the preparation process and comprises the surface irregularities of greater spacing than roughness [44]. When considering the surface texture as a source of error in the evaluation of nanoindentation experiments, only the roughness has to be taken into account.

Analysis of the surface roughness is usually performed either by stylus profilometry or by scanning probe microscopy. In this work the latter technique, in particular scanning force microscopy, is used. For the quantification of surface roughness, several parameters have been applied in literature [45]. Most commonly, height parameters as the roughness average, R_a, or the root-mean-square (rms) roughness, R_q, are utilized.
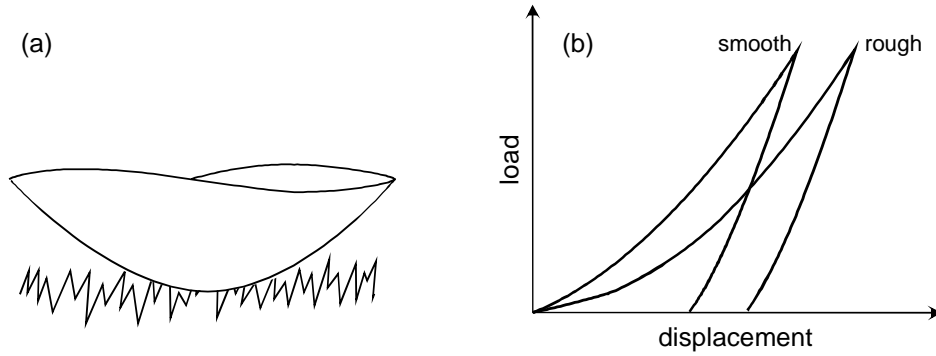
Figure 1.15: Schematic presentation of the influence of surface roughness on the contact between indenter and sample formed in an early stage of the indentation experiment (a) and on the load-displacement curves (b).

In this dissertation, the rms roughness is used. It is defined as [46]

$$R_q = \left[\frac{1}{n} \sum_{i=1}^{n} (y_i - \bar{y})^2 \right]^{1/2} , \tag{1.14}$$

where n is the number of data points in the profile, y_i are the data points that describe the relative vertical height of the surface, and $\bar{y}$ is the mean height of the surface. The latter is given by

$$\bar{y} = \frac{1}{n} \sum_{i=1}^{n} y_i . \tag{1.15}$$

1.5.3   Sample inhomogeneities

Homogeneity of a sample is a relative concept — it depends on the length scale investigated. For example, when performing *macro*hardness tests with an impression diagonal of some millimeters a two-phase alloy having a duplex microstructure with a mean grain size of some micrometers can be considered to be homogeneous. For hardness measurements on nanometer scale, however, the same sample is inhomogeneous in both the lateral and in the vertical directions.

Vertical inhomogeneities. Inhomogeneities in the vertical direction of the sample are due to surface layers that may originate from sample preparation (*e.g.* surface damage due to polishing, segregation zones formed during annealing) or from atmospheric influences (*e.g.* oxidation) [42, 48]. To counteract the influence of such unwanted surface layers on the measured hardness of the specimen, the indentation depth must be large relative to the thickness of the surface layer.

On the other hand, often, the source of the vertical inhomogeneity, simultaneously, is the matter of investigation. A prominent example is the hardness measurement of deliberately applied thin films [49–52]. To determine the genuine properties of such a
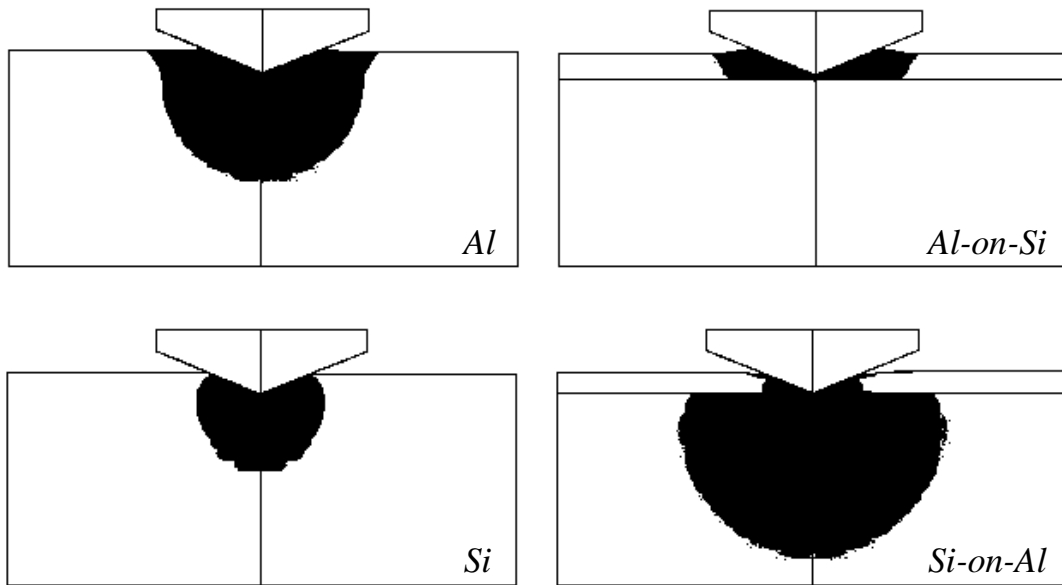
Figure 1.16: Plastically deformed zones as computed using the finite element technique for bulk aluminum, bulk silicon, an 1 µm thick Al film on Si substrate, and for an 1 µm thick Si film on Al substrate. The indentation depth in all cases is 1 µm [47].

film the indentation depth must be smaller than a critical indentation depth, which is determined by the depth of the sampled volume. For homogeneous materials, the latter has been shown to depend, among others, on the ratio E/σ_y of the material and on the state of stress of the specimen (see section 1.4). For layered materials, the critical indentation depth depends on the *combination* of the elastic and plastic properties of the film and the substrate[7]. This is illustrated in Fig. 1.16, where the results of a finite element analysis of the size of the plastic zone of a soft-on-hard system (Al-on-Si) is compared with that of a hard-on-soft system (Si-on-Al) [47]. For the homogeneous materials (Al, Si) the dimension of the computed plastic zones (also shown in Fig. 1.16) agree with the expectations: it is larger for the material with the larger ratio E/σ_y $\big((E/\sigma_y)_{Al} = 156, (E/\sigma_y)_{Si} = 29\big)$. For the layered systems it appears that in case of the soft-on-hard system the induced plastic deformation is confined exclusively in the soft layer. In case of the hard-on-soft system, however, the hard layer behaves as a transmitter of the indenter load and plastic deformation occurs mainly in the softer substrate. Obviously, the measured hardness is more affected by the substrate in a hard-on-soft system than in the opposite arrangement [47], and a general rule for the estimation of the critical indentation depth can not be given. One should also keep in

---

[7] For a detailed analysis of the deformation behaviour of thin films also the properties of the film/substrate interface as well as the possibility of elastic flexure of the film, film detachment or film fracture have to be taken into account [50, 53]
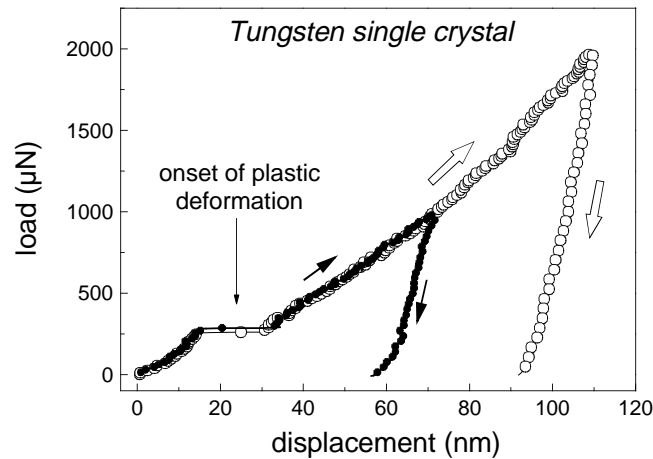
Figure 1.17: Two load-displacement curves for an electrochemically polished single crystal of tungsten. The discontinuity in the loading curve is due to the emission of dislocations. Note the good reproducibility of the "pop-in".

mind that the adhesion strength between film and substrate, which was assumed to be perfect in the above study, may change the situation greatly.

An easy test to check whether the measurements are influenced by the substrate or by an unwanted surface layer is to perform indentations to different indentation depths: if a constant value for the elastic or the plastic parameters is obtained over some depth range *and* one can neglect influences of surface roughness, thermal drift, tip shape, . . . than the genuine property of the film or the specimen is measured. It should only be noted here that a number of models have been developed to extract the genuine hardness of thin films from the usually measured compound hardness, *i.e.* the hardness that is influenced by the substrate (see Ref. 50 for an overview).

Lateral inhomogeneities. The largest lateral inhomogeneity is a free vertical surface. If the volume probed by an indentation approaches such a free vertical surface, the strain, and thus the constraint on the expansion of the plastically deformed zone, approaches zero. As a result, the hardness measured near free vertical surfaces is decreased and characterizes the (unconstrained) resistance of the material to plastic flow and the stiffness of the vertical free surface [54]. The same effect, although less pronounced, is expected to occur nearby phase- and grain boundaries.

Another source of lateral inhomogeneities are dislocations that emerge at the surface of the specimen. The dislocation density of a metal single crystal is of order 10^7 cm^{-2}. This corresponds to a mean dislocation spacing of about 3 µm. When indentations are performed in the depth range of some nanometers, the lateral size of the indentation is much smaller than the mean dislocation spacing. As a result, dislocations have first to be created during indentation before they can carry the plastic deformation. The onset of plasticity manifests itself in a discontinuity ("pop-in") in the loading curve, as shown for an electrolytically polished single crystal of tungsten in Fig. 1.17.

Such a pop-in is not observed if the surface is polished mechanically [55]. Thus for very small indentations, where dislocations are still to be produced, the loading behaviour characterizes the theoretical (defect free) strength of the material. Meanwhile, similar yield point phenomena as shown for tungsten in Fig. 1.17 have been found for many materials ranging from metals (Au, Ni, Cu, ...) to semiconductors (Si, GaAs) to oxides (Al_2O_3) (see [56] and Refs. therein). For tungsten it has first been reported in Ref. 55.

1.6 Combining nanoindentation and scanning probe microscopy

When performing indentation tests on nanometer scale with a classical nanoindenter, information on the specific sites of the indentations are hardly obtained. This may cause considerable difficulties in interpretation of the results. For example, when investigating multiphase alloys or specimens with inhomogeneous precipitate distributions, one gets a certain distribution of the hardness values — a correlation between the specific phases and the hardness values, however, is usually not obtained. Of course, with larger marker indentations the site of interest can be relocated and imaged afterwards using SEM or SPM. However, this procedure is very time consuming and not suitable for routine measurements [57]. This limitation could be overcome if an apparatus were available that provides both highly resolved load-displacement curves and high-resolution images of the topography of the sample[8]. Topography on nanometer scale is usually assessed by SPM and indentation testing on this scale is only achieved by high-resolution DSI-apparatuses. Thus the aim was to combine the imaging capability of a SPM and the indentation capability of a nanoindenter. Two approaches were followed: (i) the combination of a conventional SPM and a nanoindentation device such that the sample can easily be moved from one stage to the other [58] and (ii) the combination of a SPM and a nanoindenter in a single apparatus. The latter can be achieved either by adapting a conventional SPM ("indenting SPM": [59–61]) or by extending a conventional nanoindentation device in the capability of obtaining topographic images with a high resolution ("scanning nanoindenter" [57]: [56, 62]).

1.6.1 Indenting scanning probe microscopes

In a conventional SFM[9] (see Fig. 1.18) a fine probe tip mounted to the end of a small spring (cantilever) is brought into contact with the sample surface and is moved across

---

[8] Phases with different mechanical properties usually exhibit also different polishing behaviour. Surface topography of polished samples may therefore serve as a first criterion to distinguish between different phases.

[9] Although also scanning tunneling microscopy (STM) has been used for performing indentations and imaging of imprints [63, 64], here only the contact mode of a SFM will be considered.
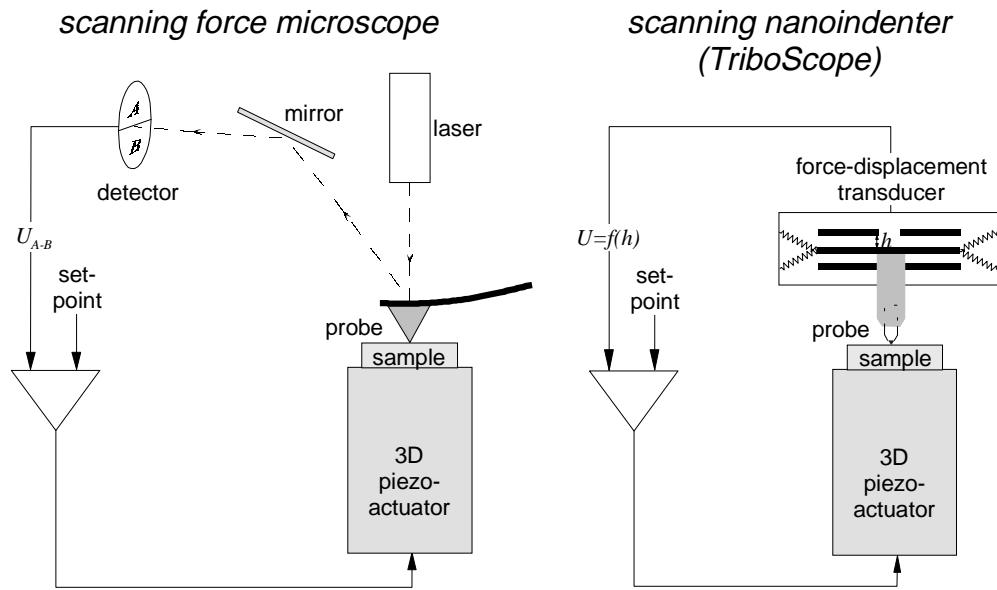
scanning force microscope *scanning nanoindenter (TriboScope)*

Figure 1.18: Comparison of a conventional scanning force microscope (left) and a scanning nanoindenter in imaging mode (right).

the surface in a raster pattern. Due to the topography of the surface, the tip and the cantilever move up and down. This movement is measured by a laser detection system and is used to control the piezoelectric actuator to which the sample is mounted. This piezo, by a corresponding contraction or expansion, keeps the movement, *i.e* the deflection, of the cantilever as small as possible and guarantees thereby a constant force between the probe tip and the sample surface. The up and down movement of the sample due to the contraction/expansion of the piezo, finally, represents the topography of the sample surface. Clearly, for high-resolution images of the topography a very compliant cantilever (high force sensitivity) and a quick response of the feedback loop are needed.

If indentations are to be performed the cantilever must be very stiff[10]. As a result, the force between the probe tip and the sample surface needed to deflect the cantilever is larger than in conventional SFM: deformation of the probed surface becomes possible and the height resolution is reduced. Moreover, accurate load-displacement curves are extremely difficult to achieve with an indenting SFM due to artifacts caused by the piezoelectric ceramic (creep, hysteresis, history dependent displacement [61]) and nonlinearities of the laser detection system. Also, when larger loads are applied to the tip-cantilever system, the cantilever may deflect, causing the tip to move laterally across the surface during indentation. Thus, the compromise between imaging and

---

[10]Commercial cantilevers for indenting have spring constants of 100–300 N/m, those for imaging only 0.01–1 N/m. The spring constant of the TriboScope transducer has been determined to be 160 N/m (*cf.* section 1.2.3).
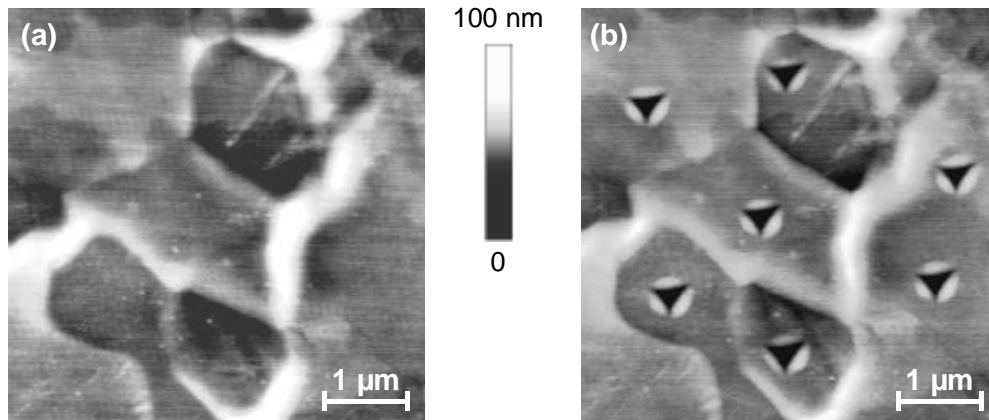
Figure 1.19: Surface topography of a Ti-6Al-4V alloy sample as obtained using the scanning nanoindenter (TriboScope) before (a) and after (b) indentations have been performed. The indentations, made to a maximum load of 2 mN, could easily be located in the middle of each grain. Note that the indentation in the center and on top of the image was moved out of the middle of the grain to avoid the tiny step which is visible there. The height is indicated by grey scaling.

indentation for an indenting SFM leads to both a reduced imaging performance and a reduced indentation capability as well.

1.6.2 The Hysitron TriboScope : Part II. A scanning nanoindenter

In this work a commercial scanning nanoindenter (TriboScope) was used. The indentation aspects of the TriboScope have been described in section 1.2.1; in this section the imaging aspects of this apparatus will be discussed. For imaging, the TriboScope makes use of the SPM to which it is mounted (see Fig. 1.18): the cantilever-laser detection system of the SFM is replaced with the load-displacement transducer and the same diamond tip that is used for indentation serves as probe tip in the imaging mode. The imaging principle is the same as for a conventional SFM: the tip is brought in contact with and is rastered over the sample surface. The feedback signal is now obtained from the displacement of the center pick-up electrode relative to the outer electrodes (Fig. 1.18). As in case of the indenting SFM the imaging performance of the scanning nanoindenter suffers from the larger spring constant and the larger inertia of the detection system as compared with a conventional SFM. However, the imaging capability of the scanning nanoindenter allows (i) to position an indentation with an accuracy of some nanometers and (ii) to obtain an image of the residual imprint of the indentation. The latter can be used to quantitatively determine the position of an indentation. In contrast with indenting SPMs, the indentation capability of the scanning nanoindenter is not affected by combining indentation and imaging capabilities. Accurate load-displacement curves can be measured and, thus, quantitative values of hardness and elastic modulus can be determined. A typical experiment with the TriboScope con-
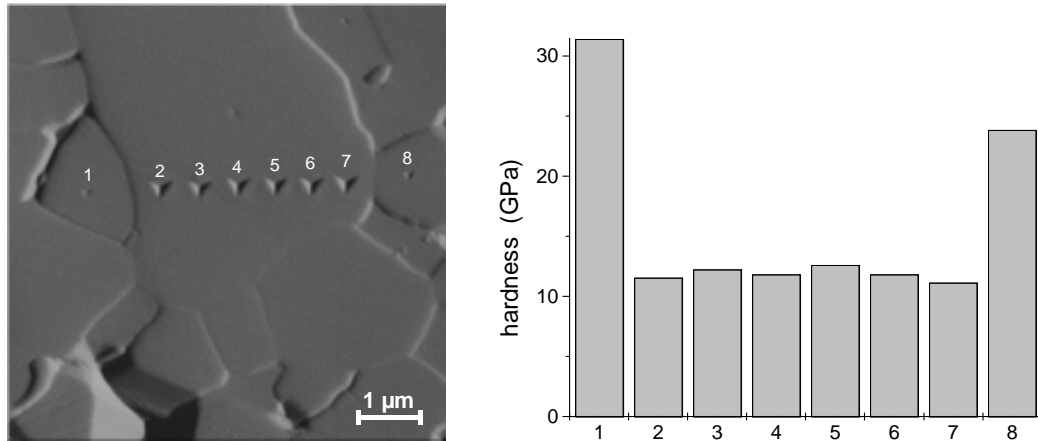
Figure 1.20: Indentations made using the same maximum load (750 µN) into a cermet alloy. The residual imprints in the harder ceramic phase (1, 8) are smaller than those in the softer metallic phase (2–7) of the sample. The corresponding hardness values are displayed in the column plot.

tains three steps: (i) Imaging of the area of interest, searching for, and selecting of, an appropriate site for the indentation (see Fig. 1.19a). (ii) Performing the indentation[11]. (iii) Imaging the area of interest including the residual imprint of the indentation (see Fig. 1.19b).

An example for the use of the scanning nanoindenter for the investigation of multiphase alloys is shown in Fig. 1.20. The image of the residual imprints may serve as a qualitative tool to distinguish between the plastically harder and the plastically softer phase. Since furthermore the load-displacement data are obtained for each indentation the mechanical properties of the individual phases/grains can be determined quantitatively and, if necessary, a profile of the mechanical properties within a grain or across a phase/grain boundary can be obtained.

Sometimes the determination of the local roughness of the specimen, *i.e.* of the roughness at exactly that place where the indentation is to be performed, or the quantification of the piled-up material around the indentation[12] serves as a motivation for the development and the use of scanning nanoindenters [62]. Although there is indeed a need to understand the influence of roughness and piling up of material on the measurement and evaluation of mechanical properties on nanometer scale, these information can not be obtained as long as the same tip is used for indenting and for imaging (see Fig. 1.21). That is because the lateral distance of the roughness asperities that is relevant for indentation is usually smaller than the tip radius and can therefore only be

---

[11]To do so, of course, the microscope feedback must be turned off before.

[12]In some cases an upward extrusion (pile-up) of displaced material forms around an indentation [22]. This pile-up effect results in an underestimation of the contact depth and thus in an overestimation of the hardness. The effect is known to occur especially for materials with small ratios E/σ_y and for soft films deposited on hard substrates [58, 65].
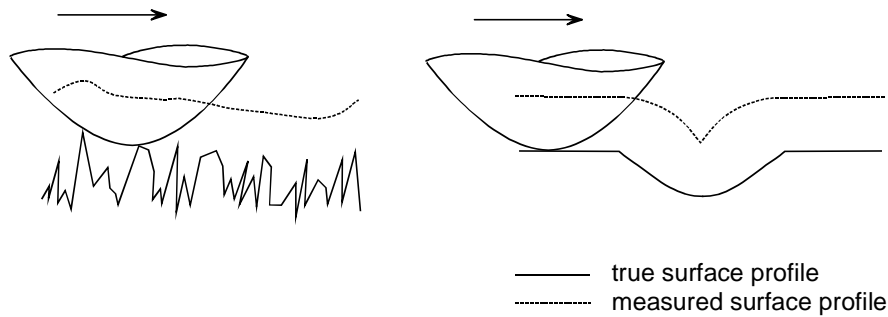
true surface profile
measured surface profile

Figure 1.21: Influence of the geometry of the probe tip on the measured profiles of a rough surface (left) and of an residual imprint of an indentation (right)

measured with a probe tip having a smaller tip radius and a smaller included tip angle. The same is true for the image of the residual imprint of an indentation: it does not reflect the "true" size or shape of the imprint but corresponds with the convolution of the "true" profile of the imprint with the geometry of the probe tip (Fig. 1.21). Therefore, information on the influence of roughness or pile-up on nanoindentation can only be obtained by using another approach of combining SPM and nanoindentation: the combination of a conventional SPM with a conventional nanoindenter such that the sample can easily be moved from one stage to the other. Only in that case no restrictions apply neither to the imaging capability of the SPM nor to the indentation capability of the nanoindenter. The major difficulty in this approach is the sample translation stage. Up to now a positioning accuracy of order 1 µm has been achieved [58]. For investigations where a nanometer scale positioning accuracy of the indentations is crucial this is not sufficient, for investigating the influence of surface roughness or of the pile-up effect on nanoindentation, however, it is.

Appendix: Comparison of a Berkovich and a cube corner indenter
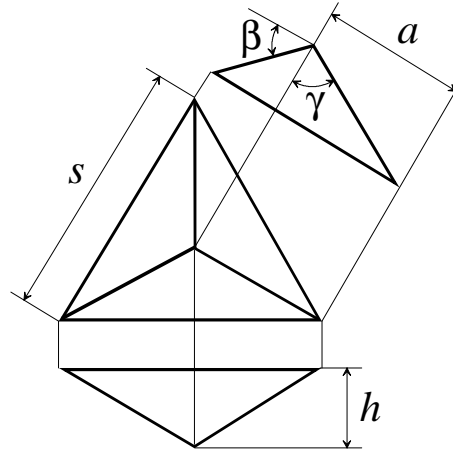
		Berkovich	*cube corner*
inclined face angle	β	$24.7°$	$54.7°$
apex angle	γ	$77.1°$	$54.7°$
projected area	$A_{\text{projected}}$	$24.5\,h^2$	$2.6\,h^2$
ratio of the projected to the surface area	$A_{\text{projected}}/A_{\text{surface}}$	0.91	0.58
ratio side length to depth	s/h	≈ 7.5	≈ 2.45
included half angle of the equivalent cone[a]	ψ	$70.3°$	$42.3°$
projected edge length	a	$2\,h/\tan\beta$

[a] The "equivalent" cone is the cone that displaces the same volume as the pyramidal indenter at a given depth.

Chapter

2

Hardness-depth profiling on nanometer scale

M. Kunert, B. Baretzky, S. P. Baker, and E. J. Mittemeijer

Abstract: Three methods for hardness-depth profiling were applied to a 200 nm thick TiC film deposited onto a Ti-6Al-4V substrate. The methods were evaluated and compared with regard to their capability to detect local changes in hardness with a depth resolution of the order of a few nanometers. In the cross-section method (CSM), the indentations are performed on a cross section of the sample, *i.e.* in a direction perpendicular to the hardness gradient. In the load-variation method (LVM) and in the constant-load method (CLM), the indentations are made in the direction of the hardness gradient, *i.e.* perpendicular to the as-prepared surface. In the LVM, the hardness-depth profile is assessed using a stepwise increase of the maximum load applied to the surface. In the CLM, sublayers are removed successively by ion sputtering and hardness measurements are performed at each newly exposed surface using the same low maximum load. The CSM revealed a nearly constant hardness across the TiC film and a sharp transition from the TiC film to the Ti-6Al-4V substrate. The hardness profile obtained using the LVM and the CLM is smeared out because the recorded response is due to both the TiC film and the underlying, softer Ti-6Al-4V substrate. The application of the CSM for the assessment of the intrinsic hardness of thin layers is further demonstrated on a TiN/Ti-multilayer.

2.1   Introduction

The mechanical properties of the near-surface region of a component often determine its service life in tribological applications. This motivates the development and the application of new surface-modification techniques and new surface layers/coatings. For example, multilayers [66, 67], gradient coatings [68], and surface regions modified by ion implantation [69, 70] can be used to tailor the tribological properties of a component. In order to optimize the process treatment to arrive at the desired properties, a fundamental understanding of the relations among processing parameters, microstructure generated, and resulting properties is required. The mechanical properties within those surface layers or modified surface regions can change drastically over depths as small as 10 nm. Hence, if a "real" hardness-depth profile of the near-surface region is to be determined a measurement method with a depth resolution on this order, or better, is needed.

To characterize the mechanical properties on such a small scale, depth-sensing *nano*indentation testing (DSI) can be performed [2, 21]. In DSI, while increasing the load, a diamond tip is pushed into the material to be probed and, subsequently, after having reached a given maximum depth or load, the tip is removed. During this procedure, the load on, as well as the displacement of, the indenter are recorded. This load versus displacement behaviour represents a fingerprint of the mechanical properties of the material averaged over a certain volume, the size of which depends on the properties of the material investigated and the shape of diamond tip used [71]. In any case, this volume and thereby the probed depth increases strongly with increasing load. Therefore, to obtain a high depth resolution, a small maximum load should be applied.

Hardness-depth profiles are usually assessed by gradually increasing the maximum load. Accordingly, the depth resolution of this load-variation method (LVM; Fig. 2.1a) is reduced severely as the maximally probed depth is increased. For thin films or modified surfaces this method measures the combined response of the film/modified surface and the substrate underneath, in particular at larger indentation depths. A number of models have been developed to extract the "true" film hardness, *i.e.* the film hardness not influenced by the substrate, from the measured composite hardness obtained using the LVM [49, 50, 72–76]. These simple models do not, however, apply to multilayers, gradient coatings, or ion-implanted surfaces where large hardness gradients can occur [77, 78]. The aim of this work was therefore to define a measurement method that reveals a more direct picture of the "true" hardness-depth profile, *i.e.* a method with a very high depth resolution. To this end two other methods were evaluated: the constant-load method (CLM; Fig. 2.1b) and the cross-section method (CSM; Fig. 2.1c). In both a small and constant maximum load was applied for all indentations — in contrast with the above LVM. In the CLM, a depth profile is achieved by successively removing thin surface layers and performing indentations at each newly exposed surface in the direction of the hardness gradient. In order to trace the hardness-depth profile using

the CSM, indentations are made normal to a cross section of the sample, *i.e.* in the direction perpendicular to the hardness gradient to be investigated.

The three methods (LVM, CLM, and CSM) were applied to a model system consisting of two materials with a sharp interface in between: a 200 nm thick TiC film on a Ti-6Al-4V substrate. The results were evaluated and compared with regard to their capability to detect changes in hardness and elastic behaviour with a depth resolution of the order of a few nanometers.

2.2 Experimental procedures and data evaluation

2.2.1 Sample preparation

The substrate (diameter 10 mm; thickness 2 mm) was cut from a bar of Ti-6Al-4V cast alloy (Ti-11.2 at% Al-3.8 at% V). The surface was prepared by grinding and mechanical polishing; the final polishing step was performed using 0.25 µm Al_2O_3. Prior to the deposition of the TiC film the substrate was cleaned ultrasonically in alcohol and, in the film deposition chamber, sputter etched for 2 min using Ar^+ ions.

A TiC film was deposited onto the substrate surface by reactive sputtering in a plasma beam sputtering apparatus (SPUTRON, Balzers). The base pressure was lower than $1 \cdot 10^{-4}$ Pa; the substrate temperature was below 393 K; the argon pressure was 0.2 Pa and the sputtering power was 40 W·cm^{-2}. Acetylene (C_2H_2) was used as reaction gas; its partial pressure was $6.7 \cdot 10^{-2}$ Pa. The film was deposited without applying a bias voltage.

To determine the thickness of the TiC film, an additional, partly covered sample was deposited. The height of the sharp step that occurred between the coated and the uncoated part of the sample surface corresponds to the film thickness. It was determined using a stylus profilometer (Taylor Hobson Talysurf 2) and was found to be (210 ± 10) nm.

After film deposition, the sample was cut into halves perpendicular to the surface using a wire saw. One half was used for the LVM and the CLM measurements; the other part was used to prepare a cross section for the CSM measurements. A protective TiN film, approximately 1 µm thick, was reactively sputtered onto the as-deposited TiC film of the latter. This TiN layer avoids rounding off of the edges of the TiC film during polishing of the cross section and counteracts the influence of the vertical free surface of the TiC film during hardness measurements on the cross sectional specimen. The cross section was ground (SiC paper, grid 3000) and mechanically polished (diamond paste; final step: 0.25 µm Al_2O_3).

2.2.2 Analysis of the composition-depth profile

The composition-depth profile of the TiC film was determined using Auger electron spectroscopy (AES) in combination with ion sputtering performed in a scanning Auger
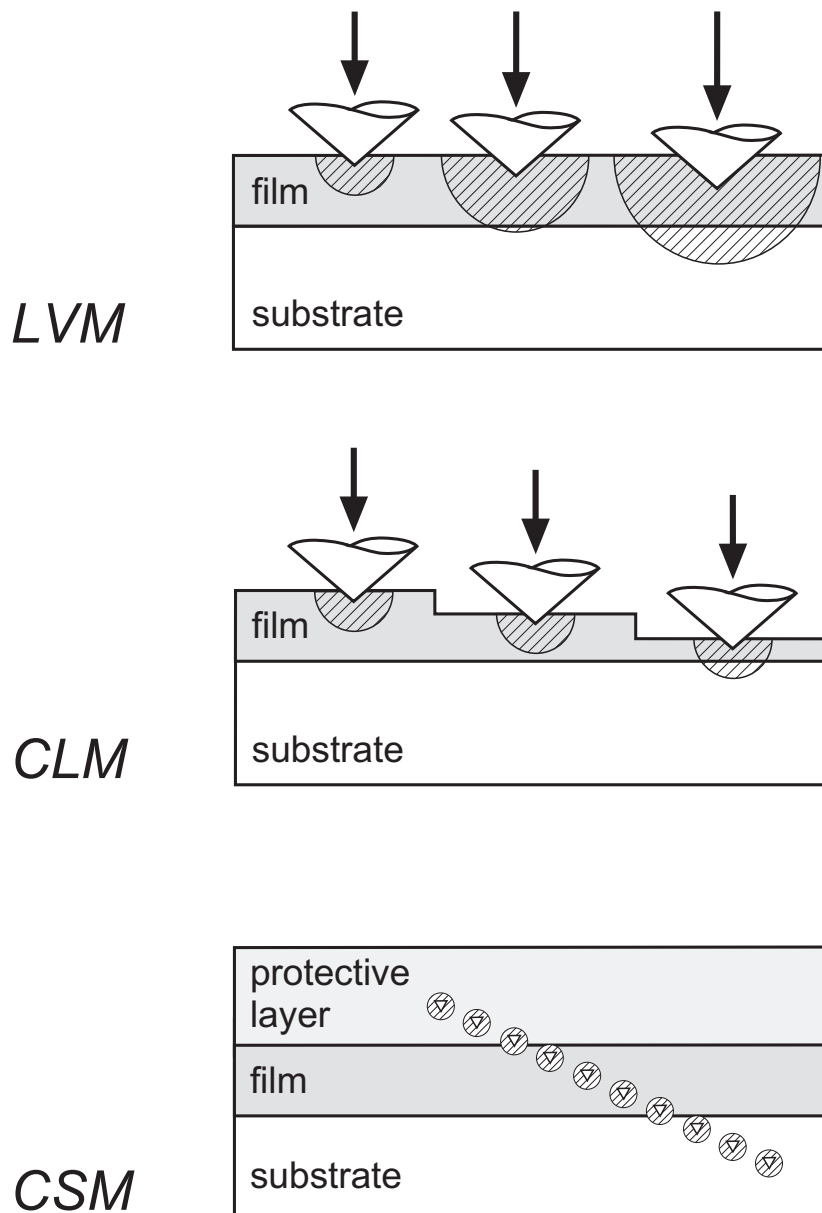
Figure 2.1: Schematic presentation of different methods of hardness-depth profiling: load-variation method (LVM), constant-load method (CLM), and cross-section method (CSM). The cross-hatched areas symbolize the dimension of the probed volume, for which a hemispherical shape is assumed.

multiprobe (SAM PHI 600): thin surface layers were successively removed by ion sputtering, and, after time intervals of one minute of sputtering, Auger spectra were recorded.

Ion sputtering. Removal of a surface layer was realized by ion sputtering using a beam of Ar^+ ions with an energy of 3 keV, rastered over an area of 2×2 mm^2. The argon pressure was $5 \cdot 10^{-3}$ Pa. To minimize roughening and damage of the surface, the angle of incidence was set as small as possible: $10°$ with respect to the surface.

Auger electron spectroscopy. Auger spectra for titanium (418 eV; Ti LMM), carbon (271 eV; C KLL), and oxygen (503 eV; O KLL) were recorded using an electron beam with a primary energy of 10 keV and a current of 1 μA. Quantitative analysis was performed by evaluating the peak to peak intensities of the differentiated spectra using a Physical Electronics software package [79]. The sensitivity factor for carbon in titanium carbide (0.295) was determined from a specially prepared TiC film, the composition of which was determined using X-ray photoelectron spectroscopy. The sensitivity factors for the other elements were taken from the software manual [79]. Values for the composition in atomic per cent were obtained by normalizing the sensitivity-corrected intensities to 100%.

Twice, after 12 min and after 24 min of sputtering, the sample was taken out of the vacuum chamber to perform hardness measurements according to the CLM.

2.2.3   Surface topography

To characterize the roughness of the surfaces to be probed by DSI, areas of 1×1 μm^2 were analyzed using Scanning Force Microscopy (SFM) in contact mode using a commercial scanning probe microscope (NanoScope III MultiMode, Digital Instruments) equipped with a standard silicon nitride tip. From these SFM images the root mean square (rms) roughness [80] was determined using a software package [81]. A 1×1 μm^2 SFM image of the cross sectional specimen contained the TiC film and parts of the TiN protective layer and the Ti-6Al-4V substrate (Fig. 2.5). To determine the rms roughness of the TiC film in the cross section, line scans about 500 nm long were made along the TiC film and the height data of these scans were used.

2.2.4   Hardness measurements and data evaluation

Hardness measurements were performed using a "scanning nanoindenter" [57] consisting of a depth-sensing force transducer (Hysitron TriboScope) combined with a commercial scanning probe microscope (NanoScope III MultiMode). With this combination, the indenter tip can also be used as a probe for contact-mode SFM imaging. This makes it possible to select the area of interest, and to position the tip before indentation with an accuracy on the order of ten nanometers, and to image the residual imprint of the indentation afterwards. The latter possibility was necessary in the CSM to determine the distance of the indentations to the TiN/TiC interface.

The high load and displacement resolutions (≈ 100 nN and ≈ 0.2 nm, respectively) of the force transducer used allows analysis of indentations with very shallow indentation depths. The indentations for the CLM and the CSM (see section 2.2.4.1) were made applying the same maximum load, chosen such that indentation depths were about 20 nm. To prevent disturbance by thermal drift, indentations were performed using a load-time cycle that was relatively short (5 s for loading and 5 s for unloading) as compared with the drift rate (< 0.1 nm/s).

For comparison, the hardness of the Ti-6Al-4V substrate in the cross section was also measured by Vickers microhardness testing (Durimet, Leitz Wetzlar) using a load of 4.9 N.

2.2.4.1   Hardness-depth profiling

The hardness-depth profile was evaluated using the three methods shown in Fig. 2.1:

(1) *Load-variation method (LVM; Fig. 2.1a):* all indentations were made in the original, as-deposited surface of the TiC film. Hardness as a function of depth was traced by increasing the maximum applied load from 250 μN to 10 mN. A total of three indentations were made at each maximum load using a three-sided pyramidal Berkovich diamond tip [82].

(2) *Constant-load method (CLM; Fig. 2.1b):* the hardness-depth profile was measured in a stepwise manner. After each hardness measurement a thin sublayer (thickness approximately 60 nm) of the TiC film was removed by ion sputtering (for details see section 2.2.2). In this way, the surface at which the hardness was measured migrated through the TiC film. Indentations were made in each new surface using the same low maximum load of 250 μN. As for the LVM measurements, three indentations were made at each step using the Berkovich indenter.

(3) *Cross-section method (CSM; Fig. 2.1c):* hardness measurements were performed on the cross section of the sample, applying a constant maximum load of 200 μN. In contrast with the LVM and the CLM measurements, a cube corner diamond tip was used to enhance the lateral resolution, and thus the depth resolution of the CSM hardness-depth profile. For a Berkovich tip — as used in the LVM and the CLM — the side length, *i.e.* the length of one side of a residual indentation in the surface plane, equals approximately 7.5 times the maximum indentation depth. Thus, for a 200 nm thick film the side length of a 25 nm deep indentation already spans the whole width (thickness) of the film. The cube corner tip is much more acute as compared to the Berkovich indenter: its ratio of side length to depth equals approximately 2.5. For comparison, indentations were also made with the Berkovich tip, applying maximum loads of 250–2000 μN, both in the center of the cross-sectioned TiC film and in the cross section of the Ti-6Al-4V substrate.
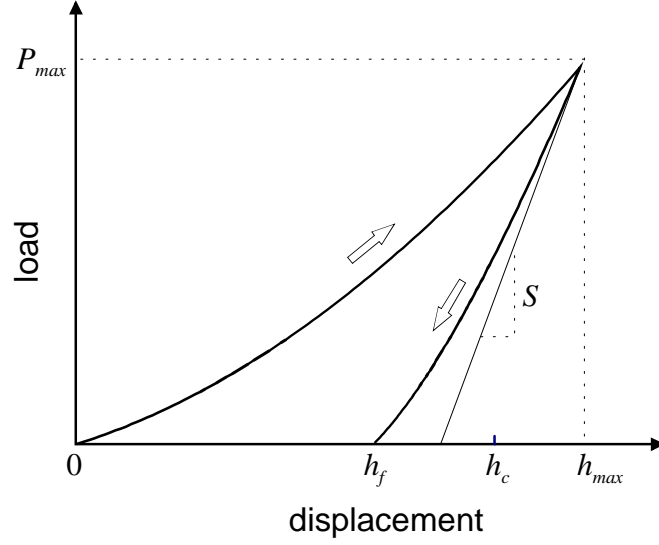
Figure 2.2: Schematic representation of a load (P)-displacement (h) curve measured by depth-sensing indentation testing. The parameters shown are explained in the text.

2.2.4.2   Data evaluation

The load (P)-displacement (h) curves (*cf.* Fig. 2.2) obtained using the different methods were analyzed as follows.

The hardness is defined as the mean contact pressure underneath the indenter at maximum load, P_{max}, [2]:

$$H \equiv \frac{P_{max}}{A_c} \ . \tag{2.1}$$

The projected contact area, A_c, is determined from the so-called area function of the indenter tip, $A_c = f(h_c)$, where h_c is the contact depth, *i.e.* the distance along the indenter axis that the indenter is in contact with the sample. The area functions of both indenters used in the experiments have been determined using the calibration procedure described in Ref. 2. The contact depth is related to the maximum indentation depth, h_{max}, by [2]

$$h_c = h_{max} - \varepsilon \cdot \frac{P_{max}}{S} \ . \tag{2.2}$$

Here S is the contact stiffness, defined as an increment in load divided by the resulting increment in displacement in the absence of plastic deformation, and $\varepsilon = 0.75$ for both indenters used. To determine the contact stiffness, S, the unloading curve was first fitted using $P = \alpha (h - h_f)^m$ (h_f = residual imprint depth; α and m are fitting parameters) from $0.95 \cdot P_{max}$ to $0.4 \cdot P_{max}$ [21]. Then, the unloading curve fit was differentiated analytically to determine the slope at maximum load: $S = (dP/dh)_{P=P_{max}}$. Using Eq. (2.2), the contact depth is calculated and is used to determine A_c, the projected contact area, from the area function. The hardness is then obtained by substitution of A_c in Eq. (2.1). Note that the definition for the "contact hardness" given in Eq. (2.1) is different from

the traditional definition of indentation hardness [22] in using the projected contact area at maximum load instead of the residual area of the imprint after unloading. Thus, for materials having a high ratio of yield stress (σ_y) to Young's modulus (E), *e.g.* rubber, the elastic properties will dominate the "contact hardness" rather than the plastic properties, in contrast with the traditional hardness, where the elastic properties do not influence the hardness value determined. For metals, however, the ratio σ_y/E and thus the elastic contribution to the net deformation is small and a comparison of the "contact hardness" and the traditional hardness is possible.

If the initial deformation upon unloading is purely elastic, the reduced elastic modulus, E_r, can be described by [19]:

$$E_r = \frac{\sqrt{\pi}}{2} \cdot \frac{S}{\sqrt{A_c}} \; , \tag{2.3a}$$

and

$$\frac{1}{E_r} = \frac{1 - v_i^2}{E_i} + \frac{1 - v^2}{E} \; . \tag{2.3b}$$

Here, E is Young's modulus and v is the Poisson ratio of the sample material; and E_i and v_i are the corresponding values of the indenter. For a diamond indenter: $E_i = 1141$ GPa and $v_i = 0.07$ [2]. The indentation modulus, I, that describes the elastic response of the sample, is just the inverse of the second term at the right hand side of Eq. (2.3b):

$$I \equiv \frac{E}{1 - v^2} \; . \tag{2.4}$$

Using the elastic constants of the indenter material and the measured reduced elastic modulus, E_r, the indentation modulus can easily be determined from Eq. (2.3b).

2.3 Results

2.3.1 Composition-depth profile

The composition-depth profile of the TiC film obtained by Auger analysis in combination with ion sputtering shows a homogeneous composition of the film (Fig. 2.3). The carbon to titanium ratio is constant and equals approximately 0.92. The oxygen content of the film is about 4 at.-%; at the interface film/substrate a slight increase occurs. The large oxygen contents at sputter times of 12 and 24 min indicate the presence of a thin oxide layer that had formed while the sample was outside the vacuum chamber to perform the hardness measurements according to the CLM (see section 2.2.2).
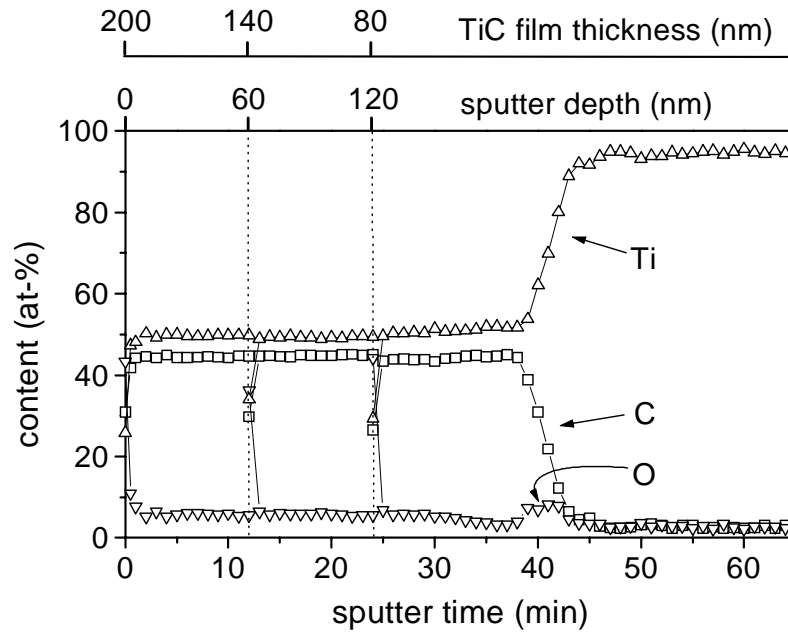
Figure 2.3: AES depth profile of the TiC film on the Ti-6Al-4V substrate showing the normalized intensities of titanium, carbon, and oxygen as function of sputter time. The corresponding sputter depths are indicated at the top of the figure.

2.3.2 Roughness

The SFM analyses allowed the determination of the roughness of the surface to be indented, in particular its evolution with sputter depth in the CLM, and the determination of the surface topography of the cross sectional sample.

The surface of the as-deposited TiC film exhibits a fine-grained appearance (Fig. 2.4a). The rms roughness as determined from Fig. 2.4a is 0.8 nm. Note that this roughness is relevant to the LVM.

In the CLM, thin surface layers are removed successively by ion sputtering after the hardness measurements at a given sputter depth have been performed. Therefore, the topography and the roughness of the surface probed can vary from step to step [83]. At the original as-deposited surface, the roughness for the CLM is the same as for the LVM. Proceeding to larger sputter depths, the roughness was found to increase to 1.1 nm at a sputter depth of 60 nm and to 1.2 nm at a sputter depth of 120 nm. At this sputter depth the surface exhibits grooves, resulting from the directional bombardment with Ar^+ ions during sputtering (see Fig. 2.4b).

The topography of the cross sectional sample is shown in Fig. 2.5a. The associated line scans across the cross section (x-direction) and along and within the TiC film (y-direction) are presented in Fig. 2.5b. The rms roughness of the TiC film at the cross section, determined from line scans along the film, is about 1.2 nm. The line scan in the x-direction (Fig. 2.5b) exhibits the topography of the cross section formed due to
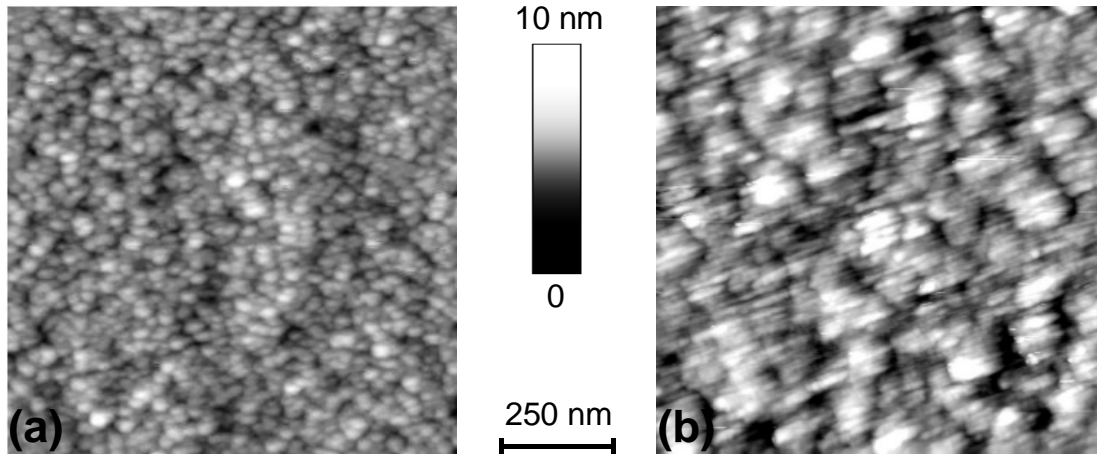
Figure 2.4: SFM images showing the topography of the surface: (a) of the as-deposited film and (b) after 24 min of Ar$^+$ ion sputtering, *i.e.* at a sputter depth of 120 nm. The height in the surface is indicated by grey scaling.
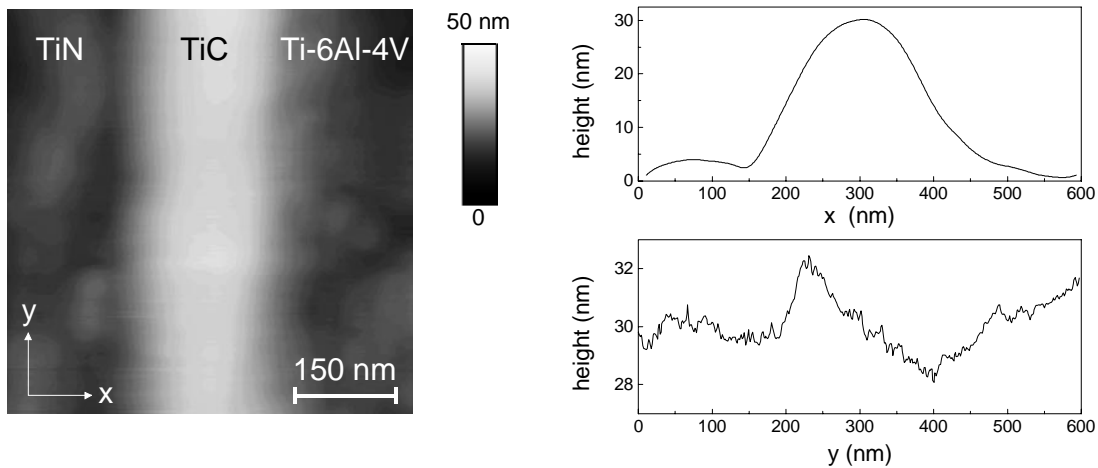

Figure 2.5: (a) SFM image (left) showing the topography of the cross-sectioned sample and (b) line scans in x- and y- directions (right). The line scan in the x-direction illustrates the topography across the cross section, while the line scan in the y-direction indicates the roughness of the TiC film at the cross section. Note the difference in ordinate (height) scales.

differences in polishing behaviour between the materials present: TiN, TiC, Ti-6Al-4V are traversed consecutively from left to right in Fig. 2.5b. Apparently, the TiC film is less affected by the mechanical polishing than both the substrate and the protective layer, as shown by the about 30 nm high protrusion in Fig. 2.5b.

2.3.3   Hardness-depth profiles

The hardness-depth profiles obtained using the LVM, the CLM, and the CSM have been presented in Fig. 2.6. In this figure the parameter labeled "depth" has different meanings (see Fig. 2.7): in case of the LVM and the CLM, the depth, t, equals the sum of the indenter displacement at maximum load, h_{max}, and the sputter depth, h_{sp}; for the LVM: $h_{sp} = 0$. In the case of the CSM, the depth, t, is defined as the (lateral) distance of the indent from the original surface of the TiC film, *i.e.* from the TiC/TiN interface. The results obtained using the three methods are distinctly different (Fig. 2.6).

Hardness. At small depths (up to $t \approx 45$ nm), the hardness-depth profile obtained using the LVM exhibits a plateau in hardness at 29 GPa. Beyond this depth the measured hardness falls off rapidly. This drop in hardness correlates with a distinct change in the slope of the loading curve observed at a load of approximately 800 µN and a displacement of approximately 45 nm (see Fig. 2.8). Below this depth the loading curves of the 2.5 mN and the 750 µN indentations coincide. At higher depths, however, a clear deviation from the low-load loading behaviour occurs, indicating the appearance of pronounced plastic deformation in the Ti-6Al-4V substrate [53, 84].

The first data point of the CLM hardness-depth profile is, of course, identical to that of the LVM-profile. In contrast with the LVM results, the CLM still exhibits the plateau hardness at a depth of $t \approx 80$ nm. (For the LVM, the measured hardness at this depth had already dropped to a value of 20 GPa.) At larger depths, the CLM also exhibits a significant decrease in hardness. However, the hardness value obtained at a depth of $t \approx 140$ nm is still larger for the CLM (23 GPa) than for the LVM (13 GPa).

The results of the CSM indicate a plateau in hardness across the entire width of the TiC film. The plateau value of 33 GPa is somewhat larger than the hardness values obtained for small depths using the LVM and the CLM (29 GPa). This CSM plateau value as obtained by using the cube corner tip agrees well with the hardness values obtained in the middle of the cross sectioned TiC film by using the Berkovich tip for small indentation depths (Fig. 2.9). In case of the Ti-6Al-4V substrate, the CSM cube corner value of 7.5 GPa (Fig. 2.6) is slightly larger than the value obtained using the Berkovich tip (6.3 GPa; Fig. 2.9). Note that the CSM data presented in Fig. 2.6 correspond to single measurements. The error bars represent a deviation of ±10%, which is typical of the scatter in the experimental data. The LVM and the CLM data shown in Fig. 2.6 each represent the mean of three measurements and the error bars indicate plus/minus one standard deviation.

Indentation modulus. In contrast to the hardness data, neither the LVM nor the CLM exhibits a plateau value for the indentation modulus. Furthermore, also the CSM data do not reveal a constant level for the indentation modulus. Instead, a peak value occurs at the center of the film. The indentation moduli obtained from the cross section specimen using the Berkovich indenter (Fig. 2.9) agree well with the cube corner CSM data (Fig. 2.6) for small indentation depths for both the TiC film and the Ti-6Al-4V substrate.
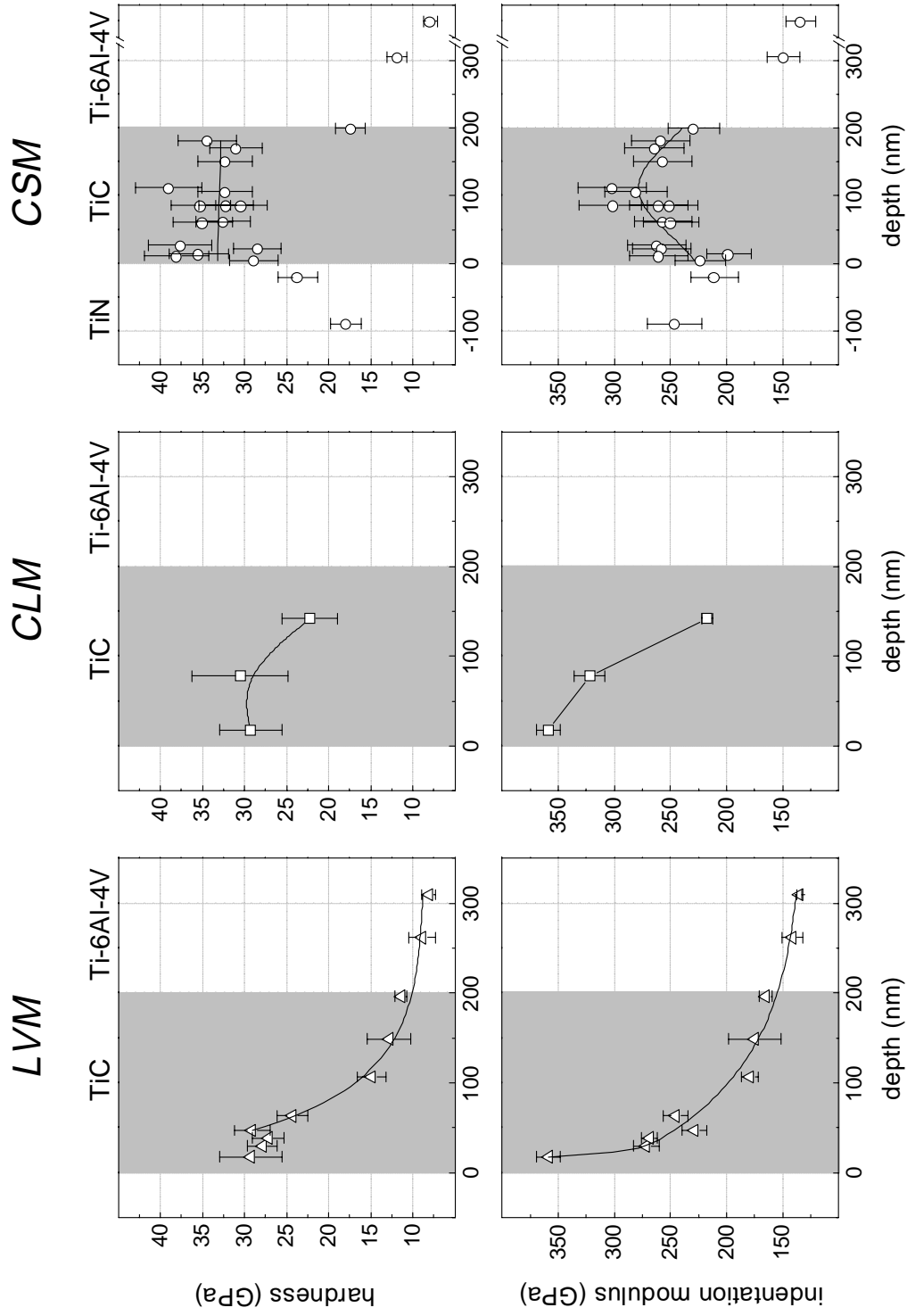
Figure 2.6: Depth-profiles of hardness and indentation modulus obtained using three different methods: load-variaton method (LVM), constant-load method (CLM), and cross-section method (CSM).
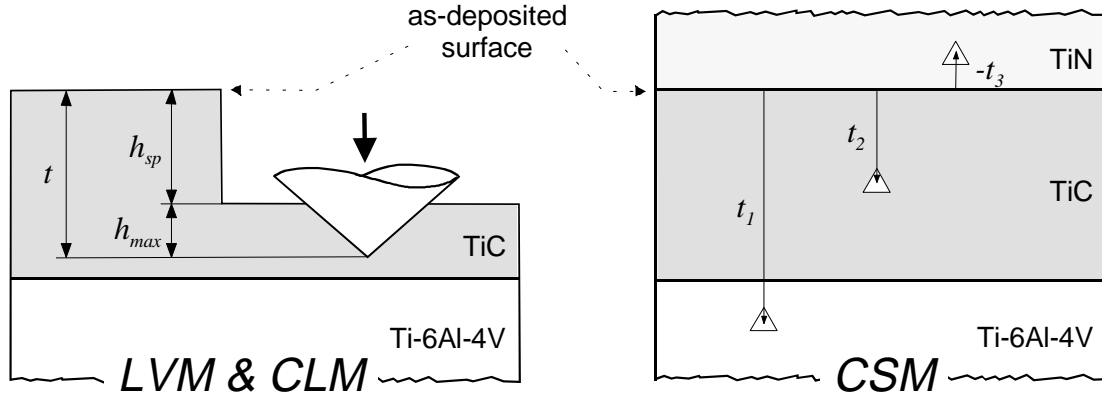
Figure 2.7: Schematic presentation of the definitions of the parameter "depth", t, used in Fig. 2.6. (h_{sp} = sputter depth, h_{max} = maximum indentation depth)

2.4   Discussion

The elastic contact model used for evaluation of the load-displacement curves is based on the assumption of a single contact between the indenter tip and a homogeneous, perfectly elastic material having a smooth surface [19]. These assumptions become more difficult to meet as the size of the indentations decreases, because of the following reasons.

Surface roughness. If the surface is rough, multiple asperity-tip contacts are formed simultaneously instead of a single contact between the indenter tip and the sample surface (see Fig. 2.10). Because the contact area of a single asperity-tip contact is small, the stress in this area is high even at a small load. As a result, the asperity deforms plastically at a low load, the displacements are larger than in the case of a sample with a smooth surface, and the projected contact area is overestimated. Thus, the values for hardness and indentation modulus calculated from Eq. (2.1) and Eq. (2.3a), respectively, are too small [43]. To counteract these problems, the indentation depth must be large relative to the roughness of the surface.

Sample inhomogeneity. Whether a sample can be conceived as homogeneous or inhomogeneous depends on the length scale that is relevant to the hardness measurements. In the present case, this length scale is a few tens of nanometers. At this scale, inhomogeneities in the direction normal to the sample can be caused by surface layers originating from sample preparation (surface damage due to polishing or ion sputtering) or from atmospheric influences (*e.g.* oxidation [48]). To counteract the influence of such surface layers on the measured substrate hardness, the indentation depth must be large relative to the thickness of the surface layer. On the other hand, a deliberately applied thin film also represents an inhomogeneity — an inhomogeneity that is the subject of investigation. In this case, the maximum indentation depth is determined by the depth to which the properties of the film can be measured without being influenced by the substrate. Unfortunately, this maximum indentation depth is usually not
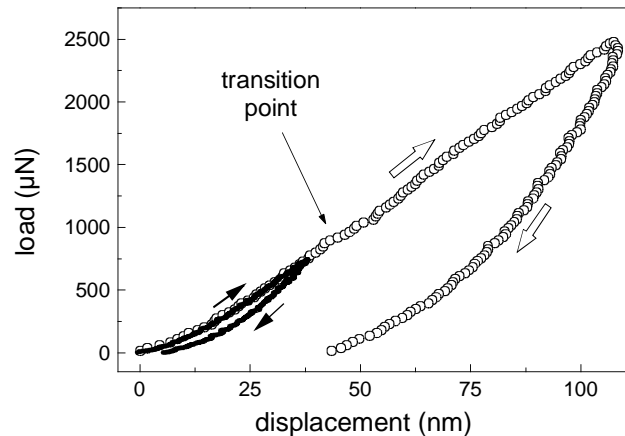
Figure 2.8: Load-displacement curves of indentations made at the as-deposited TiC film and using maximum loads of 2500 μN (○) and 750 μN (—). The change in the slope of the loading curve at approximately 45 nm indicates appearance of pronounced plastic deformation in the Ti-6Al-4V substrate.

known. It is often stated arbitrarily that for maximum indentation depths smaller than 10% of the film thickness, the "true" hardness of the film would be measured [41]. In fact, such a critical indentation depth depends on the combination of the properties of the film and substrate material [49, 50, 72–77]; it also varies with the properties of the film/substrate interface, *e.g.* with film adhesion. Hence, if the mechanical properties of thin films (hardness and elastic modulus) are to be determined by DSI, the maximum indentation depth should be (i) large enough to avoid influences from roughness and/or undesired surface layers and (ii) small enough to avoid the influence of the substrate. As the elastic strain field is more extended than the plastic one, elastic deformation is induced in the substrate at smaller indentation depths than plastic deformation.

In the following, the possible virtues of the three methods of hardness-depth profiling are discussed in view of the limitations indicated above.

Load-variation method (LVM)

For the TiC film on the Ti-6Al-4V substrate investigated, a hardness plateau up to a maximum depth of $t \approx 45$ nm was obtained (*cf.* Fig. 2.6). Such a plateau, that reflects the "true" film hardness, is not usually observed for very thin hard films on soft substrates [50] because of the effects discussed above. For the as-deposited TiC film investigated here, the maximum indentation depth of the smallest indentation exceeds the rms roughness by a factor of 22 and it can be assumed that the hardness values obtained using the LVM are not significantly affected by surface roughness. Apparently, for depths smaller than $t \approx 45$ nm plastic deformation occurs only in the TiC film. The plateau hardness value of 29 GPa lies well within the range of hardness values of 25–32 GPa, as reported for a single crystal of $TiC_{0.96}$ [85].

The indentation modulus corresponds to a weighted mean of the *elastic* properties of the film and the substrate material even at the smallest maximum indentation depth.
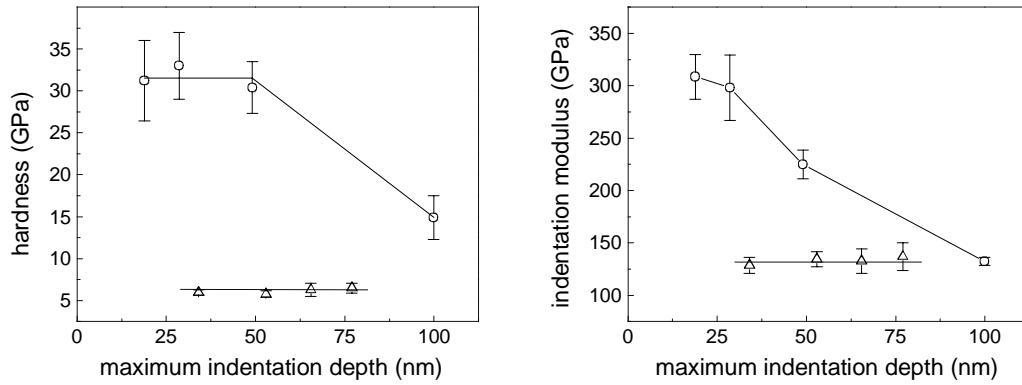
Figure 2.9: Hardness and indentation modulus in dependence of the maximum indentation depth obtained from indentations made in the center of the cross-sectioned TiC film (○) and in the cross section of the Ti-6Al-4V substrate (△) using a Berkovich indenter

Because the elastically deformed zone is much larger than the plastically deformed zone, a "film-only" indentation modulus is not observed using the LVM (*cf.* Fig. 2.6).

Constant-load method (CLM)
The CLM is a first attempt to determine the hardness-depth profile with a higher depth resolution than possible with the LVM, by keeping the volume probed both small and of constant size for each data point of the depth profile (*cf.* section 2.2.4.1).

Sublayer removal by ion sputtering led to an increased surface roughness (see section 2.3.2). However, for the CLM measurements presented here, even for the highest surface roughness (*i.e.* for the hardness measurements at a sputter depth of $h_{sp} = 120$ nm), the maximum indentation depth exceeds the rms roughness by a factor of about 17. Hence, the roughness of the indented surfaces is assumed to not markedly influence the hardness values obtained.

Physically vapour deposited coatings often exhibit high macroscopic residual stresses [86]. Upon removing sublayers of the stressed coating successively, at each step a redistribution of the residual stress in substrate and coating takes place in principle. The TiC film investigated here has been deposited at a low substrate temperature (393 K) and without applying a bias voltage. Thus, the residual stresses in the TiC film are expected to be small [87] and, therefore, effects of a change in residual macrostress upon sublayer removal on the hardness profile are considered to be negligible.

The depth resolution of the CLM is higher than that of the LVM (see results in Fig. 2.6). However, since both the LVM and the CLM measure the hardness perpendicular to the surface, the depth resolution of both suffers from the same restriction: the measured data represent a combined response of the TiC film and the Ti-6Al-4V substrate. In the CLM, the thinner the remaining film thickness is, the larger is the influence of the substrate. This effect leads to a smearing of the CLM depth profile in particular at larger sputter depths near the film/substrate interface.
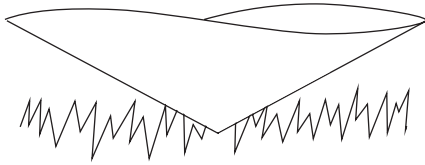
Figure 2.10: Schematic presentation of multiple tip-asperity contacts between an indenter tip and a rough sample surface

Cross-section method (CSM)

The hardness-depth profile obtained using the CSM (*cf.* section 2.3.2) shows a constant hardness across the TiC film (see Fig. 2.6). The transitions to both the Ti-6Al-4V substrate and to the protective TiN film are characterized by sharp drops in hardness.

The separation between an indentation and nearby interfaces that is required to measure the "bulk" hardness values depends on the lateral size of the volume probed in the hardness measurement. The size of this volume depends, for a given indenter tip, on the mechanical properties of the material. The sizes of the indentations made in the cross section of the TiC film are approximately equal and small with respect to the width of the film, whereas the size of the indent made in the Ti-6Al-4V substrate at the same load, at a distance of approximately $t = 300$ nm from the TiN/TiC interface in the cross section, is much larger, as expected for a softer material. For that indentation, a pronounced pile-up of plastically deformed substrate material developed near the interface to the TiC film as observed in the SFM image: the hard TiC film acted as a barrier for the spreading of the plastically deformed zone. Consequently, the corresponding hardness value of the substrate is influenced by the TiC film even for the indentation 300 nm from the interface. Also the indentation made in the protective TiN film near the TiN/TiC interface ($t = -20$ nm) appears affected by the presence of the interface with TiC. The hardness values of the TiC film obtained from indentations made very close to the interfaces, however, seem to be little (if at all) influenced by the adjacent materials. One might expect the TiC film hardness to drop near the interfaces due to plastic deformation in the adjacent softer materials, inparticular in the Ti-6Al-4V substrate. This may be understood recognizing that the maximum shear stress produced during an indentation occurs underneath the indenter tip, which is in the TiC film. Further, since the substrate is more compliant than the coating, the same displacements (along the coating/substrate interface) are associated with lower stresses in the substrate than in the film, and thus plastic deformation in the substrate might not need to occur, although the absolute value for the critical shear stress of Ti-6Al-4V is smaller that that of TiC. Thus, one may get very close to the interface without "seeing" the substrate.

The value for the indentation modulus, representing elastic behaviour, originates from a much larger volume of material. As a result, a maximum value for the indentation modulus is observed in the middle of the film (Fig. 2.6), where the least influence of the adjacent materials is experienced. This peak value for the indentation modulus agrees well with the value obtained for the smallest indentations made with the Berkovich indenter in the middle of the cross sectioned TiC film (*cf.* Figs. 2.6 and 2.9). It does not, however, represent the "true" indentation modulus of the TiC film. The

Young's moduli for a single crystal of $TiC_{0.96}$ vary between 430 and 480 GPa , depending on crystallographic orientation [85].

Both the values of hardness and those of indentation modulus as obtained from the Berkovich (for small indentation depths) and the cube corner indentations in the cross section of the TiC film agree with each other. The differences between the *maximum* values of hardness and indentation modulus observed in the depth profiles determined using the LVM/CLM and using the CSM are, therefore, not attributable to differences in the indenter tips used. A similar difference in *micro*hardness values observed on measuring perpendicular to the film surface (LVM, CLM) and parallel to it (CSM) has been reported for a (W,Ti)C film, 20 μm thick [87]. Possible reasons for this apparent hardness anisotropy could be the presence of a crystallographic texture of the TiC film, or different states of stress of the TiC film for the as-deposited and the cross sectioned sample.

Mechanical polishing can introduce strain-hardening in the material adjacent to the polished surface. The amount of affected material depends on the mechanical properties of the material. Generally, relatively soft materials are affected more strongly. Thus, the absolute differences in hardness between TiC, TiN, and Ti-6Al-4V, as observed using the CSM, may be reduced by strain hardening. Indeed, the Berkovich hardness value of 6.3 GPa recorded for the Ti-6Al-4V substrate in the cross section (Fig. 2.9) is higher than the Vickers microhardness obtained for the same sample: $HV_{0.5} = 380$ kg/mm^2 (≈ 4 GPa). This may suggest that the CSM DSI measurements are influenced by strain hardening due to preparation of the cross section. It should however be recognized that this effect is small as compared to the differences in hardness between Ti-6Al-4V and TiC.

2.5 Conclusions

Three methods for hardness-depth profiling were performed and evaluated: the load-variation method (LVM) and the constant-load method (CLM), both measuring the hardness in the direction of the hardness gradient, and the cross-section method (CSM), measuring the hardness in a cross section perpendicular to the hardness gradient.

(1) Only the CSM allows determination of changes in hardness with depth with a depth resolution of a few nanometers.

(2) Because the LVM and the CLM perform measurements in the direction of the hardness gradient to be investigated, the corresponding hardness-depth profiles become more (LVM) or less (CLM) smeared. The CSM does not suffer from this aberration.

(3) The depth resolution of the CLM is better than that of the LVM because the same low maximum load was used for all indentations. The LVM is the only method

that measures the properties of the sample in the as-prepared condition of the film. This may be of use in practical applications.

(4) For very thin films, the depth profile of the indentation modulus, an elastic parameter, cannot be determined accurately with even the CSM. This is because the elastic deformation field is larger than the plastic deformation field, and thus the indentation modulus observed is more strongly affected by the substrate than the observed hardness value.

(5) The CSM is very well suited for assessing the intrinsic, *i.e.* the "true" hardness of very thin layers, as for example in multilayer systems.

Acknowledgements

Appendix: Application of the CSM to a multilayer system

Beyond the application of the CSM as a method for direct measurements of changes in hardness with depth, the CSM may also be used to determine the intrinsic hardness of very thin layers. For multilayers, the CSM is the only method to measure directly the hardness of each single layer. This is demonstrated here for a TiN/Ti-multilayer.

Experimental

A five layer structure (TiN/Ti/TiN/Ti/TiN) was reactively sputter deposited onto a 100Cr6 tool steel substrate. The deposition was carried out at a temperature of 453 K in a Sputron (Balzers) apparatus. (For more details about the layer deposition, see Ref. 88.) The total thickness of the coating is 1.55 μm, each layer having a thickness of 0.3 μm. The composition-depth profile was determined by Auger electron spectroscopy in combination with ion sputtering. Auger spectra of the Ti (LMM), C (KLL), N (KLL), Fe (LMM), and O (KLL) transitions were taken using the same measuring conditions as described in section 2.2.2. The cross section for the hardness measurements according to the CSM was prepared by grinding (SiC paper; 1200 grid) and mechanical polishing (last step: 0.25 μm Al_2O_3). To measure the hardness of each layer three indentations in the middle of the layer were made using the cube corner tip. For the TiN layers a maximum load of 250 μN was used, whereas the indentations in the Ti layers and the substrate were made using a maximum load of 150 μN. Because of edge effects the outermost TiN layer was excluded from the analysis.

Results and discussion

The composition and hardness data obtained are shown in Fig. 2.11.

Composition. The composition-depth profile clearly reflects the five layer structure of the sample. Apart from the substrate adjacent TiN layer, the oxygen content within a single layer is almost constant; it changes somewhat from layer to layer and is generally larger for the TiN layers.

Hardness. The hardness values determined for the Ti- and the TiN layers demonstrate that the CSM is capable of determining the hardnesses of the individual layers of a multilayer composite. The minor differences in hardness between the two TiN layers and between the two Ti layers are ascribed to the small differences in oxygen content. For TiN a higher oxygen content reduces the covalent nature of the bonding and is therefore expected to decrease the hardness. For Ti, oxygen acts as a strong lattice hardener, and thus, increases the hardness [89]. Both these predictions agree well with the observations.
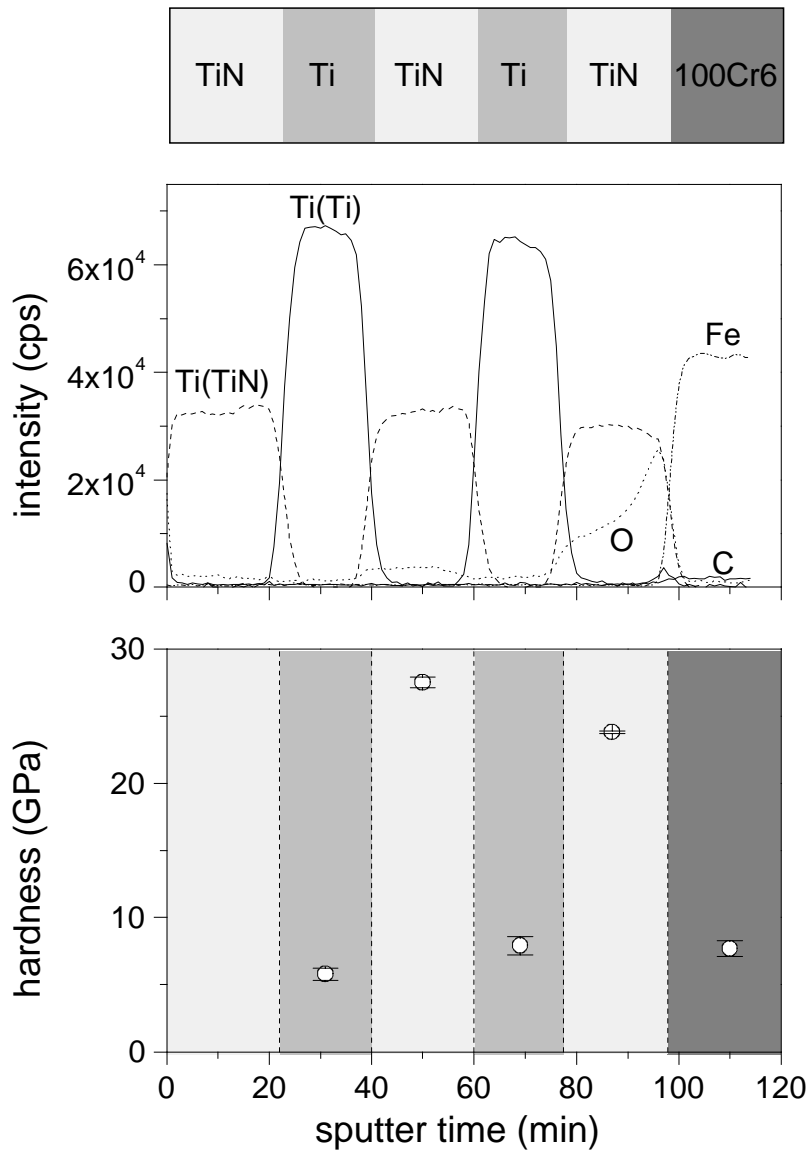
Figure 2.11: Presentation of the composition-depth profile of the TiN/Ti/TiN/Ti/TiN multi-layer and of the hardnesses of the individual layers

Chapter

3

Hardness-depth profile of a carbon-implanted Ti-6Al-4V alloy and its relation to composition and microstructure

M. Kunert, O. Kienzle, B. Baretzky, S. P. Baker, and E. J. Mittemeijer

Abstract: The mechanical properties (hardness, indentation modulus) within a carbon implanted region of a Ti-6Al-4V alloy — about 350 nm thick — were, for the first time, related with the microstructure and the chemical composition with a depth accuracy as small as ± 20 nm. Microstructure, chemical composition, and mechanical properties of the implanted alloy were determined using transmission electron microscopy, Auger electron spectroscopy, and nanoindentation, respectively. The microstructure within the implanted region can be characterized by TiC precipitates, the density of which changes with depth in accord with the carbon content. The hardness depends on the precipitate density: the maximum hardness occurs at the depth where the largest amount of carbon had accumulated and where the TiC precipitate density is such high that an almost continuous TiC layer had formed. The depth profiles of hardness and indentation modulus were measured using three different methods: the cross-section method (CSM), the constant-load method (CLM), and the load-variation method (LVM). Only the hardness-depth profile obtained using the CSM, in which the indentations are performed perpendicular to the hardness gradient on a cross section of the specimen, reflects the microstructural variations present in the implanted region. The hardness-depth profiles from the CLM and the LVM, in which the indentations are performed in the direction of the hardness gradient, are smeared. The results of the CSM were used for correlation with microstructure and composition within the implanted region.

3.1 Introduction

Ion implantation generates a complex microstructure over a depth range less than one micrometer from the sample surface. Large gradients of composition and defect concentration, as well as formation of compounds of the implanted species and elements of the original alloy can occur. As a result, pronounced changes of properties in the near-surface region are induced. Therefore, in order to achieve improvement of specific properties by ion implantation an understanding of both the effect of implantation parameters on composition and microstructure, and the relation among property, composition, and microstructure, is required. The latter is the subject of the present work.

Carbon implantation has been shown to improve the wear behaviour of Ti-6Al-4V [1]. This is often attributed to hardening of the surface region by titanium carbide precipitates [7]. Until now, hardness measurements of such ion implanted alloys have been made on a depth scale that is comparable with the depth scale of the implanted zone. These measurements therefore represent some average over the microstructural inhomogeneities present in the entire implanted zone. However, knowledge of local changes of hardness with composition and microstructure, *i.e.* as a function of depth, in the implanted region is needed for a fundamental understanding of the effect of carbon implantation on the wear behaviour. Such analysis has not been made until now.

The depth range of the microstructural variations requires that the measurements have to be made with a depth resolution on the order of 10 nm. Current methods of Auger electron spectroscopy and transmission electron microscopy provide means for assessing changes in composition and microstructure with depth on the nanometer scale, respectively. The measurement of hardness with a depth resolution on this scale has only recently become possible with the development of the depth-sensing nanoindentation (DSI) technique [2]. In DSI, a diamond tip is pushed into the material to be probed and, after having reached a given maximum depth or load, is removed. During this procedure, the load on as well as the displacement of the indenter are recorded. This load versus displacement behaviour represents a fingerprint of the mechanical properties of the material averaged over a certain volume, the size of which strongly increases with increasing load. Therefore, to obtain a high depth resolution (small probed volume), a small maximum load should be applied. Hardness-depth profiles, however, are — until now — usually assessed by gradually increasing the maximum load and thereby increasing the probed depth. Hence, the depth resolution of this load-variation method becomes continuously smaller as the maximum load increases.

Two other methods have been shown to exhibit a higher depth resolution than the LVM [90]: the constant-load method (CLM), in which the maximum load (and therefore, approximately, the probed volume) is held constant and a depth profile is obtained by successively removing thin (≈ 30 nm) layers of the surface between indentations, and the cross-section method (CSM), in which a cross section of the sample is prepared and indentations are performed to a constant maximum load along the cross section.

Using these methods, the hardness-depth profile of a doubly carbon-implanted Ti-6Al-4V alloy was determined. The dependence of hardness on depth can be explained in terms of the compositional and microstructural variations within the implanted region. The Ti-6Al-4V alloy was chosen because surgical prostheses made of this alloy are known to benefit from ion implantation [1, 69].

3.2   Experimental

3.2.1   Sample material and preparation

The material investigated was a commercial Ti-6Al-4V cast alloy bar (Vakucast Feinguß GmbH & Co KG). The average composition of the alloy is given in Tab. 3.1.

Table 3.1: Chemical composition of the Ti-6Al-4V alloy (wt-%)

Ti	Al	V	Fe	N	C	O	H
Bal.	6.0	4.0	<0.06	<0.01	<0.01	<0.17	<0.005

At room temperature, this alloy consists of a hexagonal α-phase and a cubic (bcc) β-phase [91]. The grain morphology is characterized by large primary β-grains, one to three millimeters in diameter, and secondary α-plate colonies having a size from 10 to 100 μm. The α platelets are surrounded by retained β-phase and the size of the individual α platelets varies between two and ten micrometers.

Disk-shaped specimens, 10 mm in diameter and 2 mm thick, were cut from the bar. Two sets of Ti-6Al-4V samples were prepared. Both sets were ground and mechanically polished. The last polishing step was performed using a slurry containing 70 ml OPS-suspension (Struers), 500 ml distilled water, and a small addition of H_2O_2. Then, one set of samples was doubly implanted with carbon ions using implantation energies of 120 keV and 60 keV and ion doses of $3 \cdot 10^{17}$ cm^{-2} and $4 \cdot 10^{17}$ cm^{-2}, respectively. The temperature of the samples during implantation was kept below 373 K, and the vacuum in the implantation chamber was better than 10^{-4} Pa. Details about the implanter and the implantation procedure have been described elsewhere [92, 93]. The other set of samples was used to investigate the as-polished state.

3.2.2   Depth profiling of elemental and phase composition

The composition-depth profile of the implanted region was determined using Auger electron spectroscopy (AES) in combination with ion sputtering performed in a scanning Auger multiprobe (SAM PHI 600): Thin surface layers were successively removed by ion sputtering and Auger spectra were recorded after each layer was removed.

Ion sputtering. Removal of a surface layer was realized by ion sputtering using a beam of Ar^+ ions with an energy of 3 keV, rastered over an area of 2×2 mm^2 for 90 seconds. To minimize roughening and damage of the surface, the sputtering angle was set as small as possible: $10°$ with respect to the surface. The sputter depth was determined by multiplying the measured sputter time with the previously determined sputter rate of TiC (2.49 nm/min). The sputter rate of TiC was determined by sputtering a TiC film of known thickness and composition using the same conditions as in the current experiments. The sputter rate within the implanted zone is not constant, but changes continuously with depth due to changes in composition and microstructure. Yet, the sputter rate of TiC has been found to be a good estimate for that of the carbon implanted region of Ti-6Al-4V, which partly consists of TiC (see section 3.3.1).

Auger electron spectroscopy. For assessing the composition-depth profile, Auger spectra for titanium (LMM, 418 eV), carbon (KLL, 271 eV), aluminum (LMM, 68 eV), vanadium (LMM, 473 eV) and oxygen (KLL, 503 eV) were recorded using an electron beam with a primary energy of 10 keV and a current of 1 μA. Quantitative analysis of the elemental composition-depth profile was performed by evaluating the peak-to-peak intensities of the differentiated Auger spectra using a Physical Electronics software package [79]. The sensitivity factor for carbon (0.295) was determined from a specially prepared TiC film, the composition of which has been verified by X-ray photoelectron spectroscopy. The sensitivity factors for the other elements were taken from the software manual [79].

To evaluate changes in the state of chemical bonding with depth (related to phase composition), the titanium peak was analyzed using the factor analysis method [94, 95]. In contrast with the elemental analysis, the direct (not differentiated) spectra were used for the factor analysis. Before performing the analysis, the background in the spectra (taken as Shirley-type [96]) was subtracted. Factor analysis was carried out using the Physical Electronics software package [79]. The shape of the carbon peak did not vary with depth; only a change of the peak intensity was observed (see section 3.3.1). Therefore, a factor analysis of the carbon peak was not performed.

3.2.3   Transmission electron microscopy (TEM)

3.2.3.1   Sample preparation

For TEM investigations, cross-sectional specimens were prepared using two techniques (Fig. 3.1): a conventional sandwich technique using Ar^+ ion-milling in the final thinning step [97] and a focused ion beam apparatus [98].

Sandwich technique. The specimen was cut perpendicular to the surface into pieces of $2 \times 4 \times 2$ mm^3 using a diamond wire saw. Two of those pieces were glued together (using "M Bond 610" at 423 K for 2 h) such that the as-implanted surfaces faced each other. The sandwich was ground on both sides to a thickness of about 0.5 mm and was then glued (using "M Bond AE 15" at 393 K for 2 h) into an cylinder-shaped Al_2O_3 sample holder. After completed hardening of the epoxy, the sample holder (including
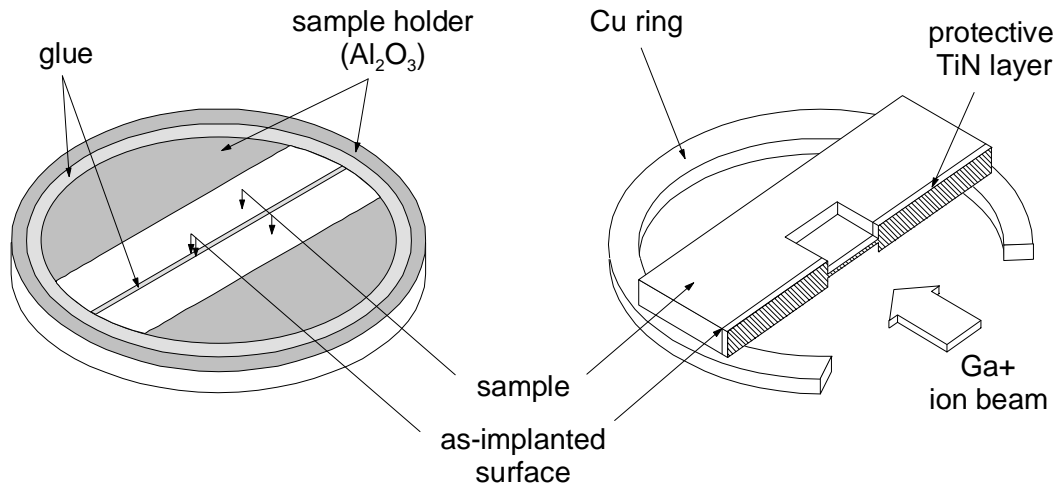
Figure 3.1: Schematic representation of the preparation of TEM cross-sectional specimens by the sandwich technique (left) and by ion milling using a focused ion beam apparatus (right)

the sandwiched specimen) was cut into discs — 300 μm thick — perpendicular to the cylinder axis using a diamond wire saw. Such a disc is shown in Fig. 3.1. Subsequently, the thickness of the discs was reduced to about 150 μm by grinding on a diamond impregnated polishing plate, and, finally, to a thickness of about 30 μm in the center of the disc by dimple grinding from both sides. Thinning to electron transparency was achieved by ion-milling the disc from both sides using Ar^+ ions (acceleration voltage 5 kV) at an angle of 10° with respect to the surface (see [97] for details). The electron-transparent area produced using this technique has the shape of a wedge. Owing to the thickness variation of the specimen, clear TEM micrographs of the complete implanted region were not obtained. Therefore, a TEM cross-sectional specimen was also prepared using a focused ion beam apparatus.

Ion milling using a focused ion beam. Prior to sample preparation, a thin (about 1 μm thick) TiN protective layer was reactively sputter deposited onto the as-implanted surface of the Ti alloy. To guarantee adhesion of this TiN film, a very thin (5–10 nm) titanium interlayer was deposited first. The TiN film protects the surface from erosion during ion milling. Then, in the first preparation step, plates of dimensions of $3 \times 1.5 \times 0.3$ mm^3 were cut from the sample perpendicular to the surface using a wire saw. The plates were ground on both sides (SiC paper: 3000 grit) to a final thickness of about 80 μm. Each plate was glued with one of its sides onto a (partially open) copper ring having an outer diameter of 3 mm (see Fig. 3.1). Thinning to electron transparency was achieved by ion milling in a focused ion beam apparatus (FIB xP, FEI Inc.). In this apparatus, a focused Ga^+ ion beam is rastered perpendicular to the TiN layer surface over designated areas and removes the material in only this area, layer by layer, by ion sputtering. Thus by rastering in areas on the original surface adjacent to both plate sides a thin, electron transparent sheet of material remains, which is oriented perpendicular to the original surface (see Fig. 3.1). The energy and the current of the ion beam were
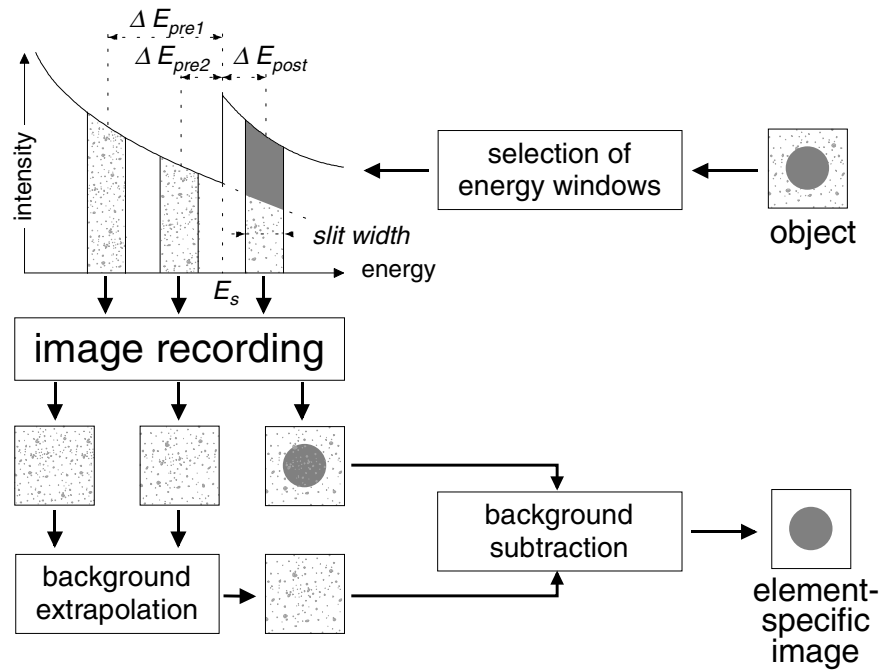
Figure 3.2: Schematic of the procedure for background subtraction (after [100]) in electron spectroscopic imaging (see also Table 3.2).

changed during the preparation: First, for removing large sample volumes, an ion beam with 30 keV and 10 nA was used; later, for "polishing" the surfaces of the cross section, the current and energy of the ion beam were reduced to 70 pA and 6 keV, respectively (see [98] for details). As a result of this procedure, a large electron-transparent area of homogeneous thickness was obtained.

3.2.3.2   Conventional TEM

Microstructural characterization was achieved by transmission electron microscopy using bright-field (BF) imaging, dark-field (DF) imaging, and selected area diffraction (SAD). The thinned cross sections were examined in a JEM 2000 FX electron microscope operated at an acceleration voltage of 200 kV. The software package EMS was used for electron diffraction analysis [99].

3.2.3.3   Electron spectroscopic imaging

Electron spectroscopic imaging (ESI) was performed using a Zeiss EM 912 Omega TEM, operated at an acceleration voltage of 100 kV. This microscope contains an integrated Omega (Ω) imaging filter, which was originally developed to increase the image quality of TEM images by removing the inelastically scattered electrons [101]. It can, however, also be used to image the spatial distribution of electrons which suffered a specific energy loss [102]. Intensity edges found in the electron

Table 3.2: Parameters of the ESI experiments. Their meaning is given in Fig. 3.2.

| element	E_s (eV)	slit width (eV)	ΔE_{post} (eV)	ΔE_{pre1} (eV)	ΔE_{pre2} (eV)
Ti	456(L)	30	15	45	15
C	284(K)	30	15	45	15
V	513(L)	30	15	50	20

energy loss spectrum (EELS) of a sample originate from inner-shell excitations and, thus, are specific for a given atomic species. Through selection of an energy window for the transmitted electrons at such an intensity edge, an image of the distribution of the specific element can be obtained. To eliminate the contribution from the background, the three-window technique was applied [103]: two ESI images are acquired in the background region in front of the intensity edge. This background intensity is extrapolated to the energy of the third ESI image, which was taken above the intensity edge, and is subtracted from the third ESI image to get an element-specific image of the illuminated area (see Fig. 3.2).

For the ESI investigation, a cross sectional specimen prepared using the FIB was used. The specific parameters used for imaging the spatial distribution of titanium, carbon, and vanadium are given in Table 3.2. The images were acquired using a Gatan 1024×1024 pixel slow-scan CCD camera. After acquisition the images were averaged over 2×2 pixels with respect to the original images, resulting in 512×512 pixel images.

3.2.4 Hardness-depth profiling

Hardness measurements were performed using a "scanning nanoindenter" [57] consisting of a depth-sensing force transducer (Hysitron TriboScope) combined with a scanning force microscope (NanoScope III MultiMode, Digital Instruments). The high resolutions of load and displacement ($\approx 100\,\mathrm{nN}$ and $\approx 0.2\,\mathrm{nm}$, respectively) of the force transducer allow analysis of indentations with very shallow depths. Additionally, because of its combination with a SFM, the same diamond tip used for performing the indentations can be used to take atomic force images before and after the indentation has been made. Use of this instrument makes it possible to select the site for an indentation with a lateral accuracy on the order of 10 nm. This positioning accuracy allowed us to make indentations exclusively within the α-phase of the alloy. The imaging capability was also used in the cross section experiments (CSM method, see below) to determine the distance of the indentations from the original (as-implanted) surface.

To obtain a hardness-depth profile of the implanted sample, three methods were used (see Fig. 3.3). A detailed description of these methods is given elsewhere [90]. Here the basic traits are summarized.

Load-Variation Method (LVM)

Constant-Load Method (CLM)
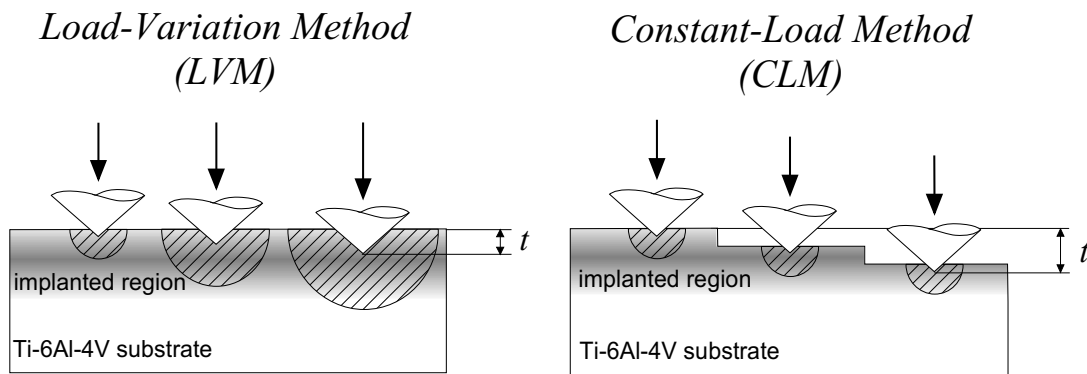
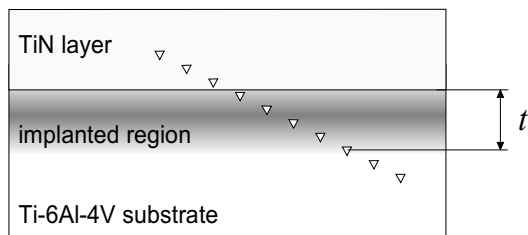## Cross-Section Method (CSM)

Figure 3.3: Schematic of the different methods used for measuring a hardness-depth profile of the carbon-implanted Ti-6Al-4V alloy. The cross-hatched areas symbolize the probed volume, for which a hemispherical shape is assumed. Whereas in the LVM this volume increases with increasing the maximum load on the indenter, it is approximately equal for all indentations in case of the CLM and the CSM (see text). The value of t represents the "depth" used to compare the results obtained using the different methods (see Fig. 3.14).

(a) *Load-Variation Method (LVM):* Hardness in dependence of depth was measured by making indentations perpendicular to the as-implanted surface, *i.e.* in the direction of the hardness gradient, at maximum applied loads ranging between $250\,\mu N$ and $11.8\,mN$. A total of 10 indentations were made at each maximum load using a Berkovich indenter, the area function of which is shown in Fig. 3.4.

(b) *Constant-Load Method (CLM):* As in the LVM, the indentations were made perpendicular to the as-implanted surface, *i.e.* in the direction of the hardness gradient. However, in this case all indentations were made using the same maximum load of $250\,\mu N$. To assess a depth profile, layers were removed successively by ion sputtering as described in section 3.2.2. Auger analysis performed at interruptions of the sputtering process made it possible to stop layer removal at chosen carbon contents. At each of the 9 chosen depths, 10 indentations were made using the same Berkovich indenter as in the LVM measurements (Fig. 3.4).

(c) *Cross-Section Method (CSM):* In this case, the hardness measurements were performed in a cross section of the specimen *i.e.* perpendicular to the hardness gra-
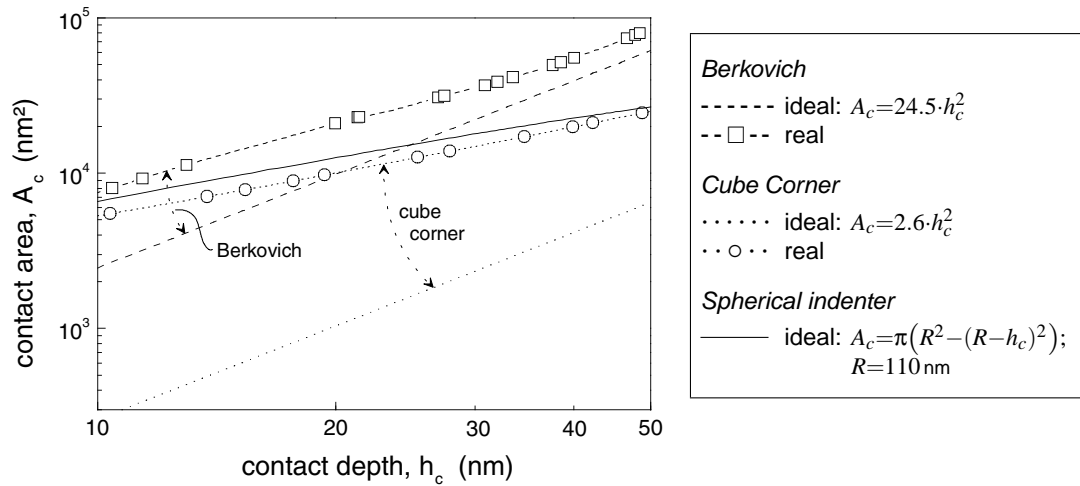
Figure 3.4: Tip-shape area functions of the different tips used for the hardness measurements. The data for the real tip shapes have been determined by performing indentation experiments on fused quartz (see Ref. 2 for details). The theoretical curves for ideally shaped Berkovich and cube corner indenters, and for a spherical indenter, have been plotted as well.

dient. To prepare the cross sections, samples having a protective TiN layer on top of the as-implanted surface (see section 3.2.3.1) were cut perpendicular to the surface using a diamond wire saw. The TiN protective layer avoids rounding off of the edges of the implanted region during polishing of the cross section and counteracts the influence of the vertical free surface during hardness measurements on the cross sectional specimen. The cross section was ground (SiC paper, grid 3000) and mechanically polished (diamond paste). The final polishing step was performed using an aqueous slurry of $0.25\,\mu m$ Al_2O_3 having a pH value of 10. To provide a high lateral and, thus, a high depth resolution, the indentations were made using a cube corner indenter (Fig. 3.4) and applying a small maximum load of $150\,\mu N$. A cube corner indenter is much more acute than a Berkovich indenter [104].

The maximum loads for the CLM and the CSM were chosen such that maximum indentation depths were large relative to the roughness of the surface to be indented. This required that the maximum indentation depths of the smallest indentations were about 20 nm. The comparison of the tip shape area functions of ideal Berkovich and cube corner indenters with that of the real indenters in Fig. 3.4 reveals that the indenters used in the experiments for small contact depths (< 20 nm) (i) deviate significantly from the ideal tip shape and (ii) can be approximated by a spherical indenter with a radius of 110 ± 10 nm.

To prevent disturbances by thermal drift, indentations were performed using a load-time cycle that was relatively short (5 s for loading and 5 s for unloading) as compared with the measured drift rate (< 0.1 nm/s).

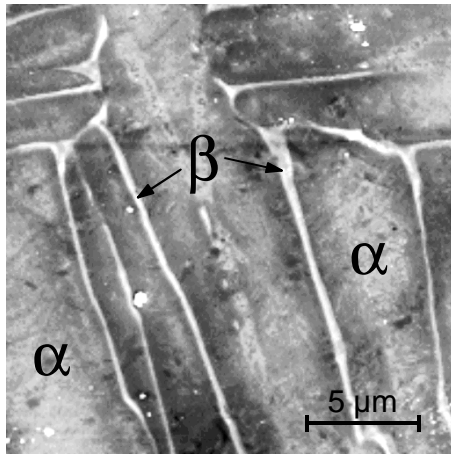Hardness and indentation modulus were obtained by analyzing the load-

Figure 3.5: Topography of the as- implanted Ti-6Al-4V alloy surface. The bright regions correspond with the interlamellar β-phase that protrudes from the surface (α-phase, dark regions) by about 20–40 nm.
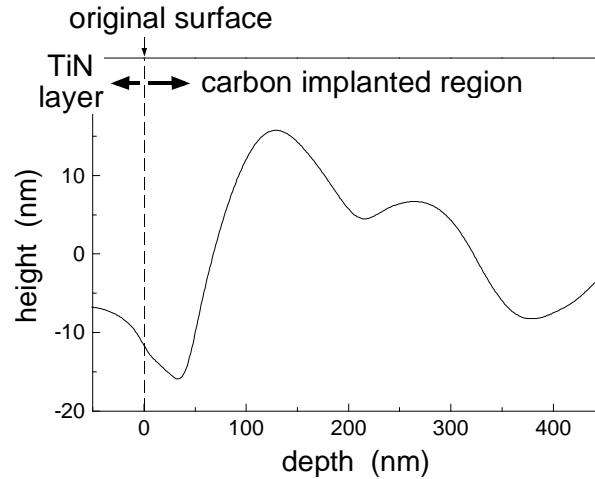
Figure 3.6: Height profile of the as-polished cross section of the carbon implanted sample.

displacement curves according to the method described in Ref.2. For this analysis, a power law was fitted to the unloading data over the range from 40 to 95% of the maximum load. At higher loads creep effects can influence the shape of the unloading curve, and at lower loads tip geometry effects may come into play [21].

3.2.5   Surface topography and surface roughness

Surface topography and roughness of the specimens were investigated using Scanning Force Microscopy (SFM) in contact mode using a NanoScope III MultiMode (Digital Instruments) equipped with a standard silicon nitride tip.

The topography of the as-implanted surface is shown in Fig. 3.5. During the implantation of ions into a substrate, surface material is removed due to ion sputtering [105]. Since different materials or phases sputter at different rates, the internal grain and phase structure of the Ti-6Al-4V alloy become visible as height differences in the surface: the β-phase (bright interlamellar regions) protrudes from the surface (α-phase) by about 20–40 nm. A height profile of the as-polished cross section of the carbon implanted sample is shown in Fig. 3.6. The line profile across the sample indicates different polishing behaviour in the different parts of the sample: TiN/Ti/C-implanted Ti-6Al-4V/Ti-6Al-4V substrate (from left to right).

The overall rms roughness [80] of the as-implanted surface is relatively high (15.9 nm; see Fig. 3.5). The roughness that affects the hardness measurements, however, is defined by the size of the indents made [43], and, because of the high posi-
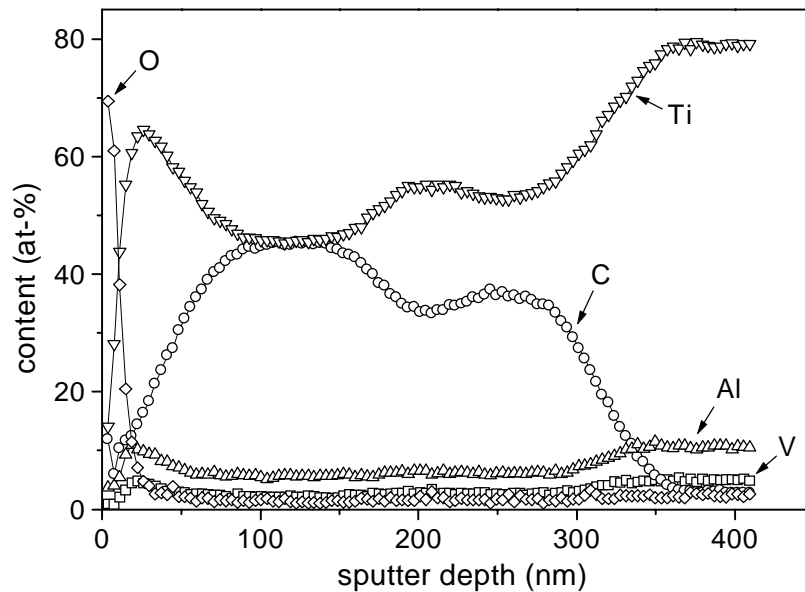
Figure 3.7: Elemental concentrations of C-implanted Ti-6Al-4V as a function of sputter depth as determined using Auger electron spectroscopy.

tioning accuracy of the "scanning nanoindenter" [57], is only related to the roughness within the α-phase platelets of the sample (see section 3.3.3). To characterize the roughness of the surfaces to be probed by DSI, areas of $1 \times 1\ \mu m^2$ within individual α-grains were recorded and the root mean square (rms) roughness [80] was determined using a Digital Instruments software package [81]. In case of the cross sectional specimen, a $1 \times 1\ \mu m^2$ SFM image contains the whole implanted region and parts of the protective TiN layer and of the Ti-6Al-4V substrate. The rms roughness determined from such an image would therefore characterize the overall roughness rather than the roughness that affects the hardness measurements. To determine a value for the latter, line scans about 500 nm long, were made within the implanted region parallel to the original surface, and the height data of these lines were evaluated.

3.3 Results and discussion

3.3.1 Depth profiles of elemental composition and phase constitution

Elemental composition. The contents of the main alloy elements (Ti, Al, V), of carbon, and of oxygen in dependence of sputter depth as determined using AES are given in Fig. 3.7. The large oxygen content at the as-implanted surface indicates the presence of an oxide layer. Upon sputtering the oxygen content decreases rapidly; at a sputter depth of approximately 30 nm it falls below the detection limit (*cf.* appendix). The
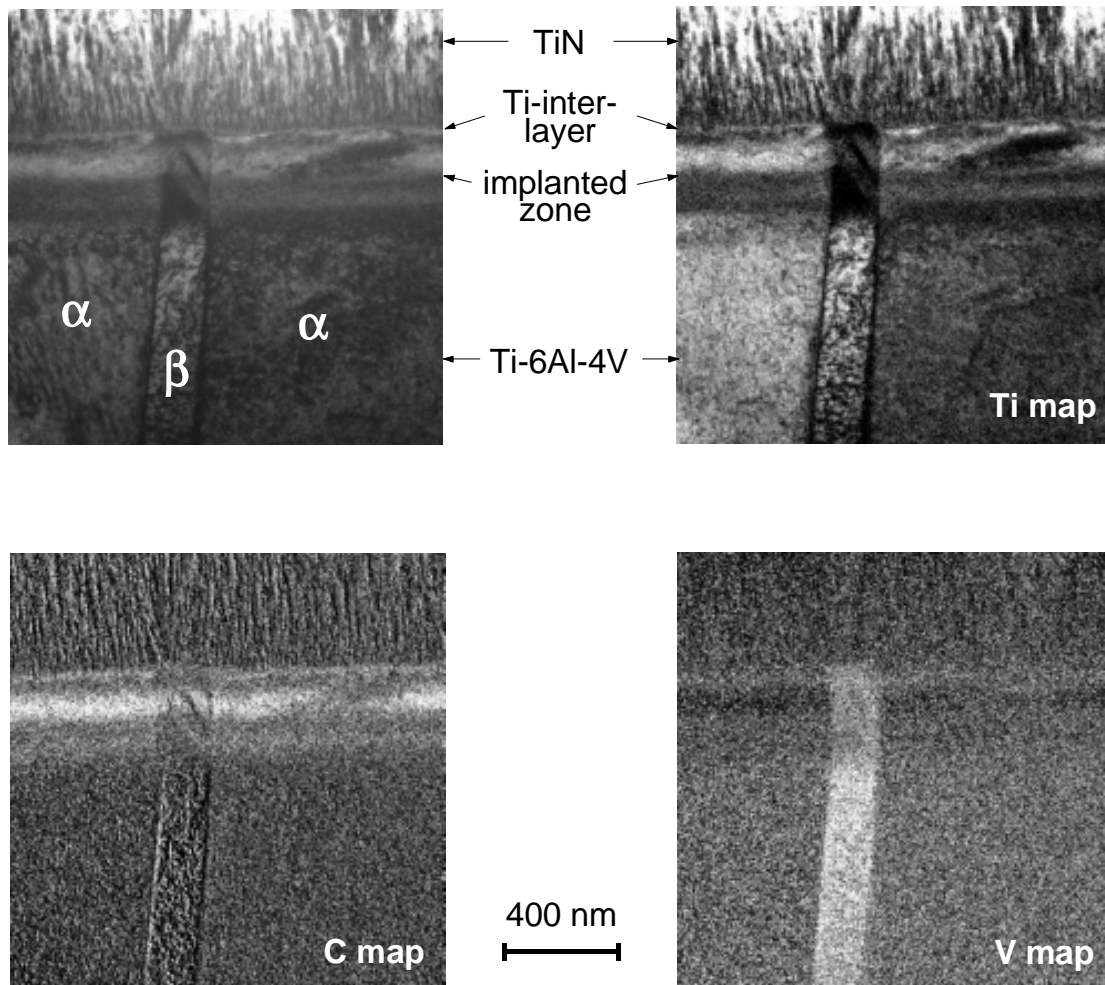
Figure 3.8: Bright field TEM-image and element maps of titanium, carbon, and vanadium taken at the same sample location of a carbon implanted Ti-6Al-4V alloy. In the elemental maps, bright regions correspond to relatively large concentrations of the element concerned. The two-phase structure is clearly visible in the higher vanadium content of the β-phase of the alloy.

carbon-depth profile is characterized by a superposition of two flat topped distributions, reflecting the double implantation applied to the sample. The higher carbon content of the near-surface peak corresponds with the higher dose ($4 \cdot 10^{17}$ cm^{-2}) and the lower implantation energy (60 keV) used in the second implantation process.

ESI was used to investigate the extent to which the elemental depth distribution is laterally homogeneous (see Fig. 3.8). As indicated in the bright field TEM-image, an area in the cross section exhibiting α- and β-phase regions was chosen. The intensities (grey-scaling) in the element maps depend on the concentration of the specific element. They may, however, also vary with sample thickness and crystallographic orientation of the grains [102]. Thus, as the thickness of the examined area is expected to be homogeneous, the different grey values of the α-platelets in the titanium map suggest
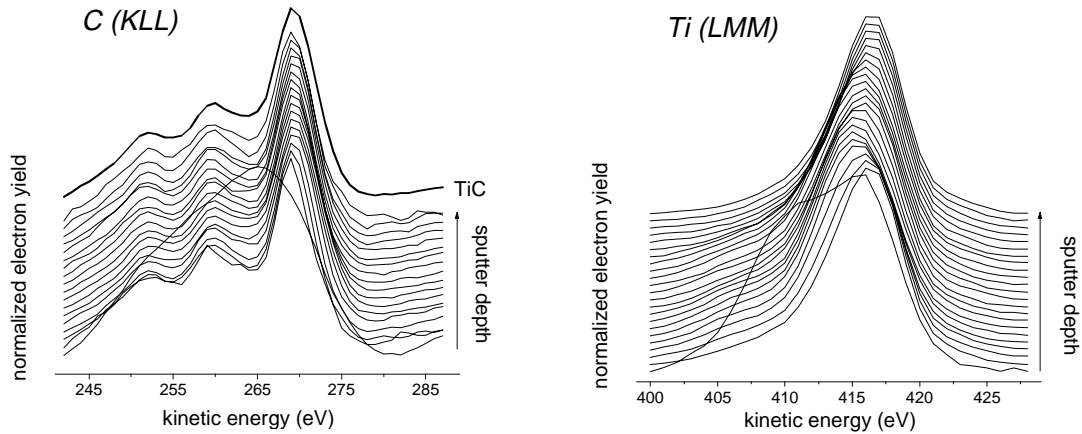
Figure 3.9: Auger peaks of carbon (KLL) and titanium (LMM) of the C-implanted Ti-6Al-4V alloy in dependence of sputter depth. While the shape and kinetic energy of the carbon peak do not change with the sputter depth, variations of the titanium peak are clearly observed. For comparison, also a C (KLL) Auger peak for pure TiC is shown (dark line on top).
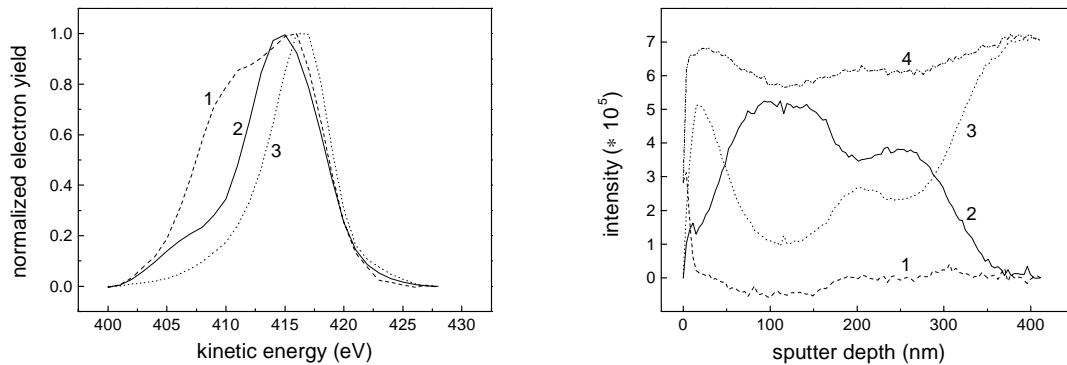

Figure 3.10: The three component spectra used for target factor analysis of the Ti (LMM) peak (a) and their contributions to the total intensity of the measured Ti peak (4) as function of sputter depth (b): (1) surface (oxidic) Ti, (2) carbidic Ti (TiC), and (3) metallic Ti (Ti-6Al-4V).

different crystallographic orientations of these platelets. The carbon map shows that the lateral distribution of the carbon-depth profile is relatively homogeneous in the α- and in the β-phase of the alloy. Furthermore, the depth range of the carbon enrichment in the implanted Ti-6Al-4V alloy indicated by the Auger analysis (Fig. 3.7) agrees well with that indicated by the ESI carbon map (Fig. 3.8). This indicates that the sputter rate of TiC indeed is a good estimate for the sputter rate of the implanted region of the Ti-6Al-4V alloy. The vanadium ESI map clearly reveals the difference in the vanadium content of the α- and β-phases.

Phase constitution. Changes in the state of chemical bonding result in variations of the shape and the position of Auger peaks [106]. The shape and the position of the carbon peaks do not change significantly with depth (Fig. 3.9). Only the carbon Auger peak directly at the as-implanted surface has a distinctly different shape, probably due

to the presence of adsorbed hydrocarbons. The shape of all the other C-peaks indicates the presence of titanium carbide, as is evident from comparison with the carbon peak from a TiC sample also given in Fig. 3.9. The invariance of peak shape and peak position of the carbon peak with depth agrees with what can be expected on basis of the Ti-C phase diagram [107]: the occurrence of elemental carbon is expected for carbon contents larger than approximately 48 at-% (experimentally it has been observed for carbon contents larger than 50 at-% [1]) or for very low carbon contents (the solubility of carbon in α-Ti is less than 1 at-%). In the present samples the maximum carbon content within the implanted region is less than about 45 at-% (see Fig. 3.7), while the solubility of carbon in α-Ti is too small to lead to experimentally detectable data.

In contrast with the carbon peaks, the titanium peaks do exhibit variations in peak shape and position with increasing depth (Fig. 3.9). This is due to the occurrence of three bonding states of titanium in the surface-adjacent region and their varying contributions to the measured Auger peak with depth: oxidic (near-surface), carbidic (TiC), and metallic titanium (see Fig. 3.10). At the as-implanted surface, titanium is present in the form of titanium oxide. With increasing sputter depths, the oxidic contribution rapidly vanishes. Simultaneously, the contribution of the carbidic component increases; it runs in parallel with the elemental depth profile of carbon, which is consistent with the notion that the implanted carbon is chemically completely bonded to titanium. In the depth range between about 80 and 150 nm, the carbidic contribution is nearly constant and forms a plateau, the intensity of which reaches approximately 5/6 of the total intensity of the measured Ti peak in this depth range (denoted as "4" in Fig. 3.10).

3.3.2 Microstructure as a function of depth

To analyze the microstructure of the implanted region, a conventional TEM study was performed on cross-sectional specimens using bright-field (BF) and dark-field (DF) imaging techniques. A TEM-BF image of the specimen prepared using the FIB apparatus (*cf.* section 3.2.3.1) is shown in Fig. 3.11a. Several zones with different thicknesses are clearly visible within the implanted region. The prominent spots of the selected area diffraction (SAD) pattern of the implanted region shown in Fig. 3.11b correspond to the diffraction pattern (DP) of α-Ti in a $[41\bar{5}3]$ zone axis. However, a splitting is observed for the $\bar{1}013$ and the $10\bar{1}3$ α-Ti spots: "extra" reflections occur at lower scattering angles. The TEM-DF images shown in Fig. 3.11c and d were recorded using the $\bar{1}013$ α-Ti and the "extra" reflection, respectively. The images show practically complementary contast. The DF image recorded with the "extra" reflection (Fig. 3.11d) exhibits two bright fringes: one at thicknesses between about 50–180 nm (including a very intense bright region between about 100–170 nm) and a second between about 230–280 nm. As follows from a comparison with the depth profile of the carbon content shown in Fig. 3.7 it can be concluded that the intensity in the DF image is closely related to the carbon content, *i.e.* bright regions correspond to regions with high carbon content. Hence, the implanted carbon is responsible for the "extra" reflection. One may suggest that at regions with high carbon content, TiC has formed either as nanometer-
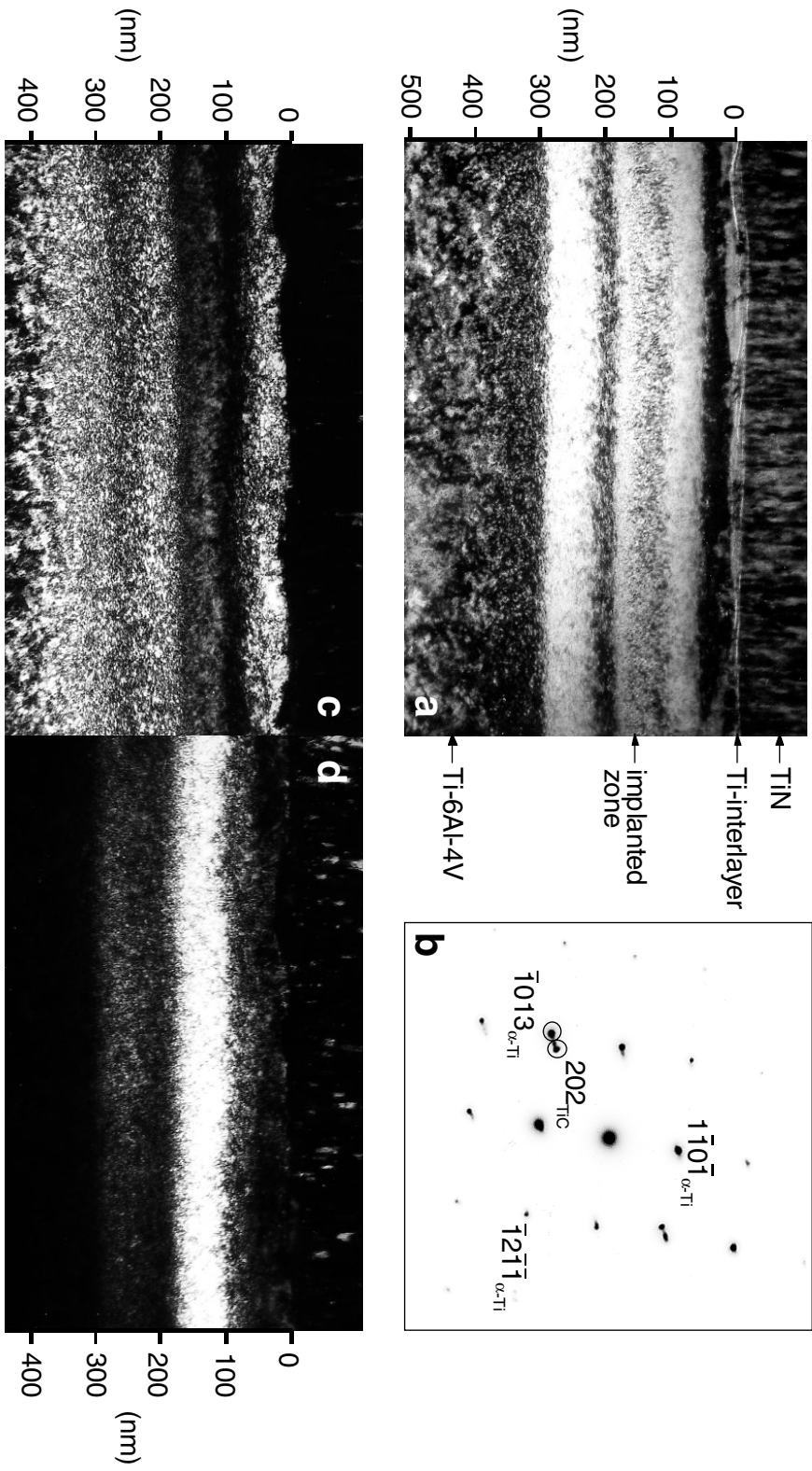
Figure 3.11: Bright field (a) and dark field (c, d) electron microscopy micrographs of the cross section of the C-implanted Ti-6Al-4V specimen, taken at the same location of the sample. The spots used for dark field imaging have been marked in the diffraction pattern corresponding to a [41$\bar{5}$3] α-Ti zone axis (b); the $\bar{1}$01$\bar{3}$ α-Ti diffraction spot is used for micrograph (c) and a 202 TiC diffraction spot is used for micrograph (d).

sized precipitates embedded in α-Ti or as single phase regions. Indeed, the high carbon content with almost stoichiometric Ti:C ratio (Fig. 3.7) within the most intense bright fringe in Fig. 3.11d supports this interpretation. Also, when using the known lattice spacings of α-Ti ($a = 0.293$ nm and $c = 0.467$ nm [108]) as an internal standard, the lattice spacing corresponding to the "extra" spots, which was determined to be 0.149 nm, is very close to the lattice spacing of the $\{202\}$ planes in TiC (0.153 nm). Thus, the more bright a depth zone in the DF image shown in Fig. 3.11d appears, the larger is the density of TiC precipitates. The above interpretation of the DF image shown in Fig. 3.11d is also consistent with the results of the factor analysis (Fig. 3.10), and with findings in literature: at smaller carbon doses ($2 \cdot 10^{17}$ cm^{-2}/75 keV) TiC has been found in form of precipitates [1, 109] and at higher doses ($6 \cdot 10^{17}$ cm^{-2}/50 keV and $7 \cdot 10^{17}$ cm^{-2}/75 keV) the formation of single phase TiC layer was reported [1].

At depths larger than 300 nm the density of TiC precipitates is quickly reduced, in accordance with the decreasing carbon content. At these depths, still affected by the ion implantation, the α-Ti matrix appears to have a very fine cell structure, which is ascribed to the formation of a dense network of dislocation loops by coalescence of implantation-induced vacancies. This cell structure is still present, but is coarser at depths larger than 400 nm, *i.e.* at depths that are larger than the thickness of the actually carbon-implanted layer. Such an effect has been referred to as a "long-range effect" of ion implantation [110].

A region of twinned TiC has been found in the sample prepared using the sandwich technique (*cf.* section 3.2.3.1): see the BF image shown in Fig. 3.12a. The corresponding SAD pattern in Fig. 3.12b can be interpreted as a superposition of a DP of the α-Ti matrix with $[2\bar{1}\bar{1}0]$ zone axis (Fig. 3.12c) and that of TiC with a $\langle 110 \rangle$-type zone axis twinned at a $\{111\}$ plane (Fig. 3.12d). The twinning operation involves the formation of a $\Sigma 3 (111)$ grain boundary, which can be considered as a pure tilt-boundary, with a $\{111\}$ grain boundary plane, characterized by a rotation of 70.5° about an $\langle 110 \rangle$ tilt-axis (Ref. 111). The DP shown in Fig. 3.12b also indicates an orientation relationship between the α-Ti matrix and the TiC, where the close-packed planes are parallel: $(0001)_{\alpha\text{-Ti}} \parallel (111)_{\text{TiC}}$ and $[2\bar{1}\bar{1}0]_{\alpha\text{-Ti}} \parallel [101]_{\text{TiC}}$.

It is noted that in the DF image from the α-Ti shown in Fig. 3.11c a black fringe appears between about 50–100 nm, whereas there is no complementary intense bright fringe in the DF image from the TiC reflection shown in Fig. 3.11d. This suggests the occurrence of TiC with a *different* crystallographic orientation in this depth range, consistent with twinning. TiC twinning was not observed directly in the TEM analysis of the FIB specimen. This appears to be due to unfavorable orientation of the TiC; *i.e.* a $\langle 110 \rangle$-type zone axis does not occur in Fig. 3.11.

3.3.3 Hardness-depth profile

Small indentation depths are a prerequisite in order to measure a hardness-depth profile with a high depth resolution. The interpretation of such hardness-depth profiles can be
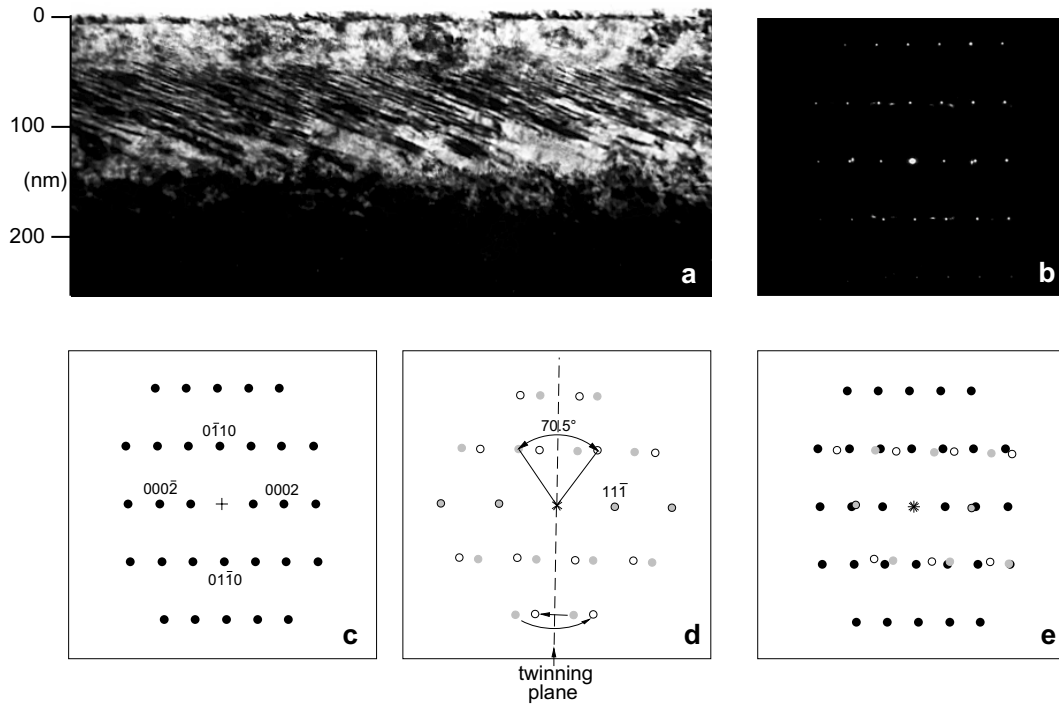
Figure 3.12: Bright field electron micrograph (a) and corresponding selected area diffraction pattern (b). The observed diffraction pattern (b) consists of contributions from three components indicated schematically in (c) and (d): (c) diffraction pattern from α-Ti-6Al-4V (with zone axis [$2\bar{1}\bar{1}0$]), (d) diffraction pattern from TiC (○, with zone axis [101]) and its twin obtained by twinning on a {111} plane (●). The diffraction pattern in (e) is the superposition of (c) and (d) and is identical to (b).

complicated due to the roles of surface roughness and sample inhomogeneities [57, 90]. First, such effects will be discussed for the present results.

Surface roughness. Surface roughness may result in seemingly low values of hardness and indentation modulus. To counteract surface roughness effects, the indentation depth must be large relative to the roughness [57, 90]. The rms surface roughness of the α-phase of the Ti-6Al-4V alloy increased upon carbon implantation from 0.14 nm (as-polished) to 0.47 nm (as-implanted). These roughness values are relevant for the hardness measurements according to the LVM. In the CLM, thin surface layers are removed by ion sputtering after the hardness measurements at the given sputter depth were performed. Therefore, the roughness of the surface to be indented changes from step to step as shown in Fig. 3.13. At the original as-implanted surface, the roughness for the CLM is the same as for the LVM. Then, proceeding to larger sputter depths, the roughness increases slightly up to about 2 nm. After a slight decrease at a sputter depth of 350 nm, a sharp rise in roughness occurs, reaching a value of 4 nm. The rms roughness of the cross section of the implanted sample did not show significant differences between different positions on the cross section. This roughness was found to be
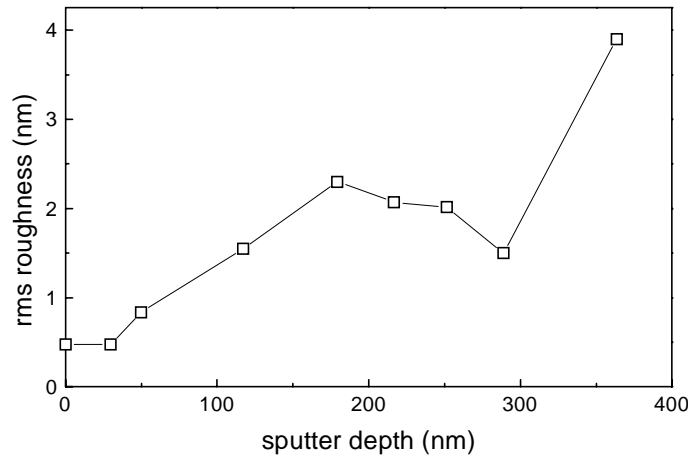
Figure 3.13: Change in rms roughness of the surface to be indented with sputter depth in the CLM

at most 0.6 nm. For the cross section of the not implanted sample, a value of 0.8 nm was measured.

From the above it can be concluded that in the LVM and the CSM, in view of the indentation depths, the roughness is too small to influence the measured values of hardness and indentation modulus. For the CLM, the highest ratio of rms roughness to maximum indentation depth occurs at a sputter depth of about 180 nm, where the rms roughness amounts to approximately 9.5 % of the maximum indentation depth (*c.f.* section 3.2.4). However, even then the loading curves did not reveal any effect of surface roughness.

Inhomogeneities. Whether a sample is taken to be homogeneous or inhomogeneous depends on the length scale considered. Here the relevant length scale is that pertaining to the size of an indentation, *i.e.* a few tens of nanometers. At this length scale, the implanted Ti-6Al-4V alloy must be considered to be inhomogeneous both in the lateral directions and in the vertical direction.

The lateral inhomogeneity is determined by the two-phase structure of the alloy (see Fig. 3.5). The mechanical properties of the hexagonal α-phase differ from those of the cubic (bcc) β-phase, *e.g.* the Young modulus of the β-phase (72 ± 25 GPa) is smaller than that of the α-phase (100–145 GPa, depending on the crystallographic orientation) [89]. For the LVM and the CLM measurements, the effect of such inhomogeneity was minimized by making the indentations exclusively in the α-phase of the alloy. Of course, β-phase lying underneath the surface might be "hit" as well, especially in case of indentations performed using larger maximum loads in the LVM. In the CSM, it was not possible to select only α-platelets for indentation because polishing as surface preparation (as compared to sputtering in the LVM and the CLM; *cf.* section 3.2.5) did not lead to height differences between the α- and β-phases in the surface of the cross section.
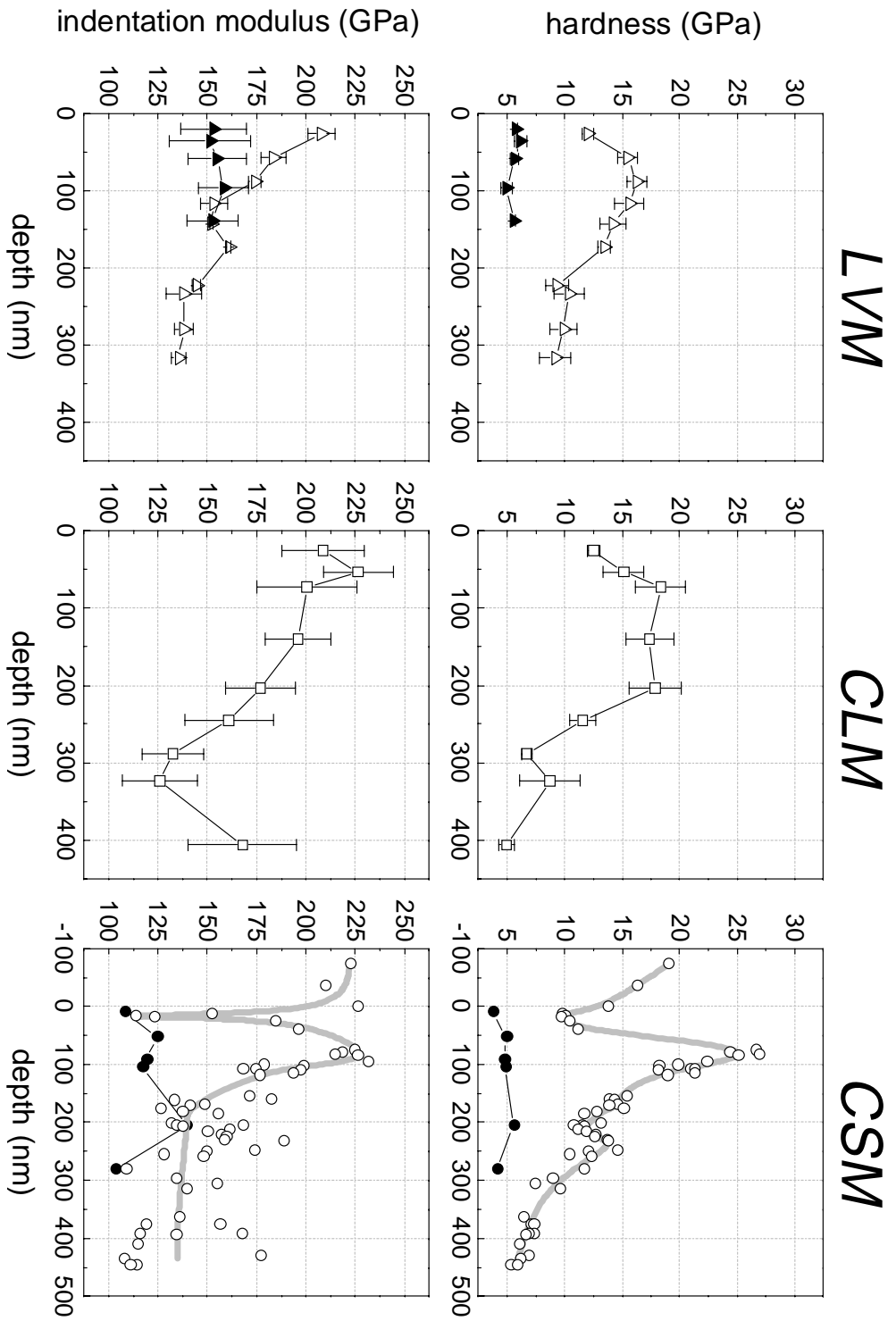
Figure 3.14: Hardness and indentation modulus as a function of depth for carbon implanted and for not implanted Ti-6Al-4V obtained using the LVM (△-implanted, ▲-not implanted), the CLM (□-implanted), and the CSM (○-implanted, ●-not implanted). The grey lines drawn in the CSM plots are meant to guide the eye.

The main inhomogeneity in the vertical direction originates from the implantation process and is the subject of this investigation : the large gradient of composition and the large changes of microstructure that cause the mechanical properties to change greatly with depth. Two other additional vertical inhomogeneities may be oxide layers and hardened surface layers resulting from polishing or ion sputtering. As holds for the roughness, the thickness of the oxide layer relevant for the LVM is the same for all indentations made. For the CLM, however, it varies with depth and depends on the carbon content of the surface at which the oxide was formed (see appendix). Then, for the CSM, one would expect the oxide thickness to vary across the cross section. However, even for an unimplanted sample, the surface of which is expected to be covered with a relatively thick oxide layer (see appendix), the hardness determined using the LVM does not change with the probed depth (see Fig. 3.14). Hence, it is concluded, that the surface oxide layers do not significantly influence the hardness values measured.

The same reasoning can be applied concerning the influence of a possible strain-hardened surface layer on the LVM results. Its influence appears to be negligibly small, since the hardness value of 5 GPa obtained for the not implanted sample agrees well with the macrohardness value of 4 GPa [112]. The slightly smaller value of the macro-hardness may be due to averaging over the α- and the softer β-phase, whereas the nanohardness data presented here pertain to the α-phase of the alloy only. In the CLM and the CSM, ion sputtering and polishing, respectively, are applied as surface treatments. As the hardness obtained at the cross section for both the not implanted specimen as well as for the not implanted region of the implanted specimen exhibits the same value (5 GPa) as that obtained using the LVM for the not implanted specimen (Fig. 3.14), it can be concluded that the surfaces of the cross sectioned samples are not heavily strain hardened; at least, they are in a condition comparable with the surfaces of the LVM samples. The effect of ion sputtering on the CLM results is expected to be negligible in any case because of the low sputtering angle used.

Hardness and indentation modulus data. The hardness and indentation modulus data obtained in this work, using the LVM, the CLM, and the CSM (*cf.* section 3.2.4) are gathered in Fig. 3.14 as a function of depth beneath the original surface (see Fig. 3.3). Only the CSM, where the indentations are made perpendicular to the hardness gradient, allows a direct determination of local changes in hardness with depth, with a depth resolution of a few nanometers, as shown previously [90]. In the LVM and the CLM, the measurements are performed in the direction of the hardness gradient. Therefore, the depth profiles obtained using these methods become more (LVM) or less (CLM) smeared, due to a combined response of the surface engineered region (film, implanted region) and the underlying (softer) substrate. The depth resolution of the CLM is better than that of the LVM because the same low maximum load is used for all indentations. The implanted region investigated here differs from the model system used in Ref. 90 (a thin TiC film on a Ti-6Al-4V substrate): (i) the implanted region consists of several zones over the implanted depth range, which (ii) are not separated by sharp interfaces. In particular, as indicated by all three methods (see Fig. 3.14), a soft layer exists adjacent to the surface of the implanted sample. Upon proceeding to

larger depths, the hardness increases and, for all three methods, reaches a maximum at a depth of approximately 80 nm.

For the LVM, the hardness value at this depth of maximal hardness ($H_{max}^{LVM} \approx$ 16 GPa) represents a combined response of the soft zone at the surface, of the harder layer underneath, and of the substrate as well [113]. Accordingly, for LVM hardness measurements made at higher loads, the hardness values obtained do not become equal to the pure substrate value.

In case of the CLM, the softer zone is successively removed upon proceeding to larger depths and, thus, it does not influence the hardness value measured at 80 nm. Furthermore, the maximum load applied in the CLM was 8 times smaller than that in the LVM at this depth. As a result, $H_{max}^{CLM} > H_{max}^{LVM}$: in the CLM, a hardness plateau at the level of H_{max}^{CLM} ($\approx$ 18 GPa) has been found, extending from approximately 80–200 nm, whereas $H_{max}^{LVM} \approx$ 16 GPa (see above).

In the CSM data a zone of homogeneous hardness is not observed. Instead, a sharp peak in hardness exists at the depth of 80 nm ($\approx$ 27 GPa), followed by a second peak at $\approx$ 230 nm, less sharp and having a smaller maximum value ($\approx$ 15 GPa). Thus, qualitatively *and* quantitatively, the CSM reflects variations of the hardness within the implanted region that reflect the compositional and microstructural variations within the implanted region (see sections 3.3.1 and 3.3.2), and that could not be measured with either the CLM or the LVM. The hardness value of the soft layer directly at the as implanted surface is lower and the maximum hardness value within the implanted region is higher for the CSM than for the CLM and the LVM (Fig. 3.14). These results can be fully understood on basis of the better depth resolution provided by the CSM (see section 3.2.4).

In contrast with the hardness maxima, the maxima of the indentation modulus occur at different depths for all three methods: $t_{max,I}^{LVM} < t_{max,I}^{CLM} < t_{max,I}^{CSM}$ (see Fig. 3.14). Only for the CSM do the maxima of hardness and indentation modulus occur at the same depth. For the LVM and the CLM, the depth at which the maximum of the indentation modulus occurs is smaller than that of the corresponding maximum in hardness. This is due to the larger dimension of the elastic strain field that develops underneath an indenter as compared with that of the plastically deformed zone. Note that the indentation modulus data depend only on the elastic response of the specimen, in contrast with the nanohardness data.

3.4   General discussion

To allow detailed comparison, the variations with depth of microstructure, composition, and mechanical properties (CSM) within the carbon implanted region have been arranged in a composite figure (Fig. 3.15). Then, the compatibility of the different depth scales should be considered. The depth co-ordinate of the CLM hardness profile represents the sum of the sputter depth and the maximum indentation depth (Fig. 3.3). The peak value of the hardness in the CSM occurs at precisely the depth where the

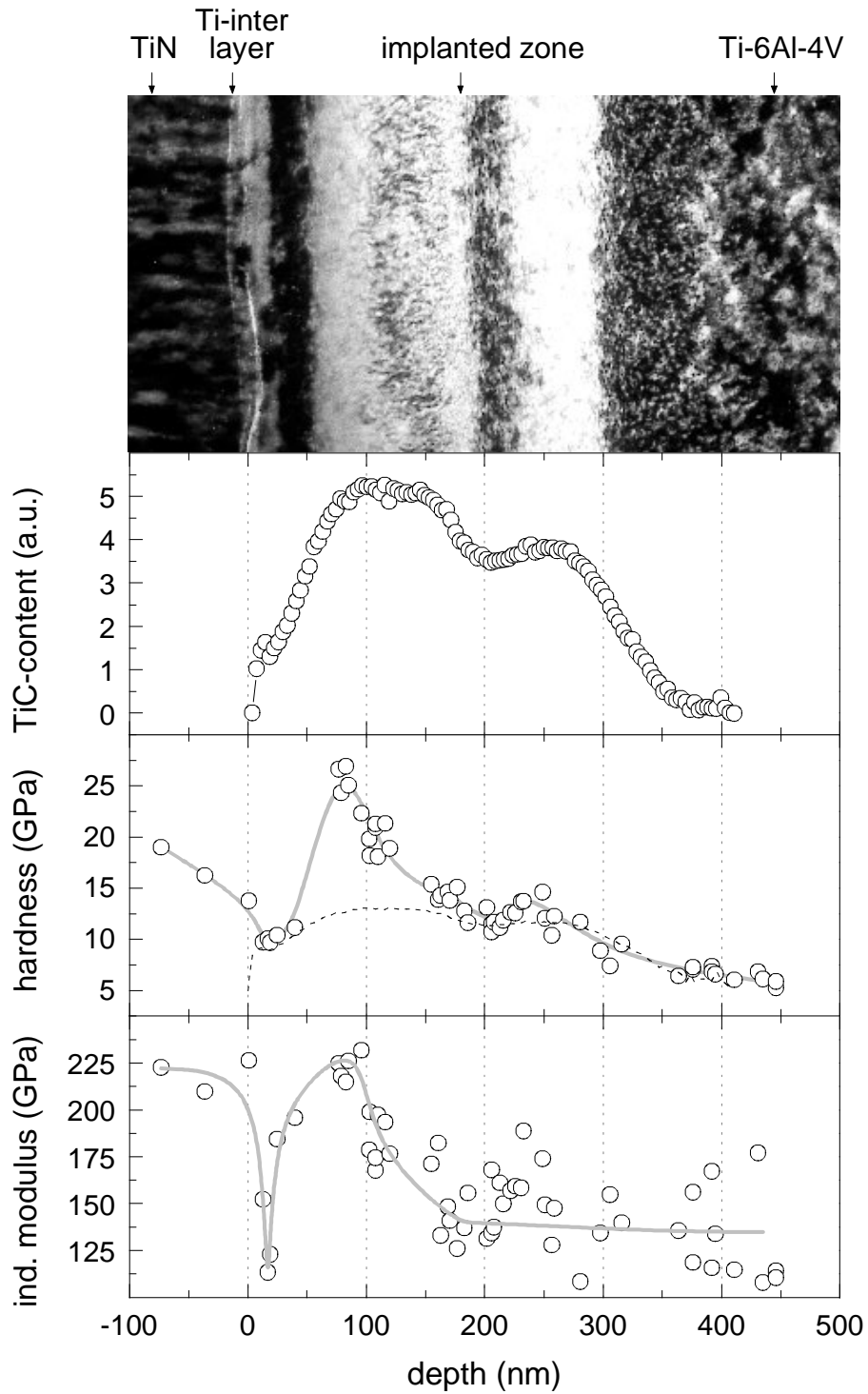*Figure 3.15:* Survey of the variations in the implanted region as a function of depth, from top to bottom: microstructure (bright field electron micrograph, *cf.* Fig. 3.11a), TiC-content (*cf.* Fig. 3.10), and hardness and indentation modulus as obtained using the CSM (*cf.* Fig. 3.14). The dashed line in the hardness plot corresponds to the hardness of precipitation hardened Ti-6Al-4V as derived from Eq. (3.2). See text for details.

specimen is expected to be the hardest (*i.e.* at maximum TiC-content). Apparently, the depth profiles of hardness and composition represent very well the changes with depth of the microstructure, with a depth accuracy of about ± 20 nm.

The implantation process produces a complicated graded microstructure with a high density of precipitates and defects, such as dislocation networks, within the implanted region, which causes an increase of hardness. Several mechanisms of strengthening might contribute: solid solution hardening, work hardening, and precipitation hardening. The latter is thought to be most effective in zones where the precipitate phase (TiC) is the minority phase. The increase in critical shear stress, $\Delta \tau_c$, due to precipitate hardening can be expressed as [114]:

$$\Delta \tau_c \approx 0.81 \cdot \left(\frac{3}{2\pi}\right)^{1/2} \cdot \frac{Gb}{r} \cdot f^{1/2} . \tag{3.1}$$

Here, G is the shear modulus of the matrix ($G_{\text{Ti-6Al-4V}} = 44$ GPa [112]), b is the length of the shortest Burgers vector ($\vec{b} = 1/3[\bar{1}100]$; $b = a/\sqrt{3}$ with $a = 0.293$ nm [112]), r is the radius and f the volume fraction of the precipitates, which are assumed to be of spherical shape. The factor 0.81 takes into account the randomness of the precipitate distribution. With $H = 3 \cdot \sigma_y$ [22] and $\tau_c = 0.5 \cdot \sigma_y$, with σ_y as the yield strength, it follows for the hardness:

$$H \approx H_{\text{Ti-6Al-4V}} + 3.3 \cdot \frac{G \cdot b}{r} \cdot f^{1/2} . \tag{3.2}$$

The hardness of the not implanted Ti-6Al-4V substrate is $H_{\text{Ti-6Al-4V}} = 5$ GPa (Fig. 3.14). The volume fraction of TiC precipitates was approximated by dividing the intensity of the TiC component of the factor analysis (factor 3 in Fig. 3.10) by the total intensity of the titanium peak (factor 4 in Fig. 3.10). The diameter of the precipitates is taken as 7 nm — which is a reasonable value for implantation induced TiC precipitation in Ti-6Al-4V [1]. Then, the hardness values calculated using Eq. (3.2) correlate well with the values of the CSM hardness-depth profile, except in the depth range between about 50–180 nm (see dashed line in Fig. 3.15). In this depth range the TiC phase predominates, possibly with some intergranular α-Ti phase (see section 3.3.2), and hence, particle hardening does not apply as hardening model. Instead, the hardness at these depths should be compared with that of massive TiC, which is ≈ 30 GPa [90]. Since some α-Ti phase is also present, the full hardness of TiC is not reached.

The above reasoning concerning the hardness data also applies to the results of the indentation modulus data. In zones where the hardness is dominated by dispersion hardening (pinning of dislocations), no distinct change in overall elastic parameters (as the indentation modulus) is expected as compared to the not implanted situation. Indeed, the value of the indentation modulus at these depths is close to that of not implanted Ti-6Al-4V (see Fig. 3.14 for a depth of approximately 20 nm). Similarly, for depths larger than 180 nm the modulus is rather constant and about equal to the value of

not implanted Ti-6Al-4V. However, at approximately 240 nm a small increase in modulus is observed. This increase happens at that location where the second maximum in carbon content is observed, *i.e.* where a relatively high density of TiC precipitates is present. The increase of the indentation modulus from 20 nm to larger depths is caused by the increase of the amount of TiC precipitates. The increase of the indentation modulus from 20 nm to smaller depths is due to the occurrence of the TiN protective layer.

3.5 Conclusions

Microstructure, chemical composition, and mechanical properties (hardness, indentation modulus) of a doubly carbon implanted Ti-6Al-4V alloy were measured and were related with each other with a depth accuracy of about $\pm$ 20 nm.

(1) The implanted region exhibits a complicated graded microstructure with a double topped-peak depth profile of the carbon content, a high density of TiC precipitates, and dislocation networks. The precipitate density changes gradually with depth in accord with the carbon content. In the depth region with the highest carbon content an almost continuous TiC film had formed.

(2) The depth profiles of hardness and indentation modulus are best measured using the depth-sensing nanoindentation technique applying the cross-section method (CSM). The depth profiles of hardness and indentation modulus obtained using the CSM, in which the indentations are performed perpendicular to the hardness gradient, represent well the microstructural and compositional variations within the implanted region. The corresponding depth profiles recorded using the CLM and the LVM — usually applied in the literature — in which the indentations are performed in the direction of the hardness gradient, are smeared.

(3) The maximum hardness occurs at that depth where the TiC content is maximal and an almost continuous TiC layer had formed. In zones with a smaller TiC precipitate density, the hardness can be quantitatively explained as due to TiC dispersion hardening.

The possibility to truly trace the hardness-depth profile of an ion implanted region and to relate this hardness-depth profile with the local variations in microstructure and composition, (also) provides a tool for the development of property-tailored ion implantation procedures.

Acknowledgements

Appendix: Thickness of the oxide layer

In the CLM, surface layers are removed successively by ion sputtering and the sample is taken out of the Auger apparatus at chosen sputter depths to perform hardness measurements. The natural oxide layer that had formed each time the specimen was taken outside the vacuum chamber, had to be removed by sputtering at the beginning of the next CLM sputtering step. The oxygen to titanium (O:Ti) ratio of the consecutive sputtering steps as a function of depth is given in Fig. 3.16. The interruptions at the chosen sputter depths are clearly observed in this figure by the corresponding high O:Ti ratios recorded at these sputter depths upon continuation of the sputtering. The O:Ti ratio depends on the stoichiometry of the oxide and on its thickness. The shape of the Auger titanium peak strongly varies with the stoichiometry of the oxide layer [115]. Different peak shapes were not observed here: At each sputtering step the titanium peak shape indicated the presence of TiO_2. Thus, the ratio O:Ti can be used as a measure for the thickness of the oxide layer formed at a given sputter step. The carbon-depth profile is also shown in Fig. 3.16. Clearly, a close relation exists between the thickness of the oxide layer and the carbon content at the occurring surface at which the oxide had formed. The sputtering depth needed to reduce the O:Ti ratio to zero is much larger for the as-implanted surface than for all other sputtering steps. This may be attributed to oxygen from the oxide layer at the original surface being implanted into the near surface region by knock-on effects during carbon implantation.

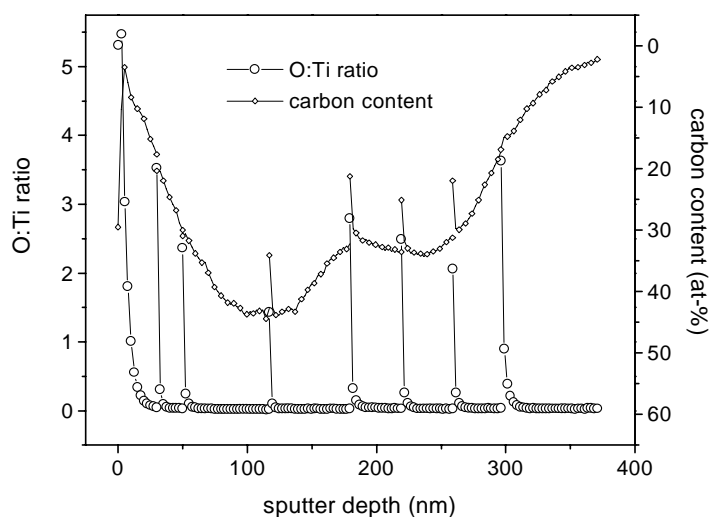*Figure 3.16:* O:Ti ratio as a function of sputter depth. The high values of the O:Ti ratio occur at sputter depths where the sputtering was interrupted to measure — out of the vacuum chamber — the hardness on the current surface. The corresponding carbon content is also shown as a function of sputter depth. Note that the maximum values for the O:Ti ratio correlate with the local carbon content.

Kapitel

4

Kurzfassung der Dissertation

Das Verschleissverhalten der für medizinische Prothesen verwendeten TiAl6V4-Legierung kann durch Kohlenstoffimplantation deutlich verbessert werden. Oft wird dies auf die Erhöhung der Härte im oberflächennahen Bereich zurückgeführt. Um diesen Effekt besser zu verstehen, wurden die Tiefenprofile von chemischer Zusammensetzung und Härte, sowie die Änderung der Mikrostruktur innerhalb der implantierten Region gemessen und, erstmalig, mit einer Genauigkeit von ± 20 nm korreliert. Möglich wurde dies durch die Anwendung einer neuen Methode zur Härte-Tiefenprofilanalyse im Nanometerbereich, der so genannten Querschnittsmethode (CSM). Bei dieser Methode wird – im Unterschied zur bisher üblichen Lastvariationsmethode (LVM) und im Unterschied zur Methode der konstanten Last (CLM) – die Härte nicht in Richtung des Härtegradienten, sondern senkrecht zu ihm, also in eine Richtung konstanter Härte gemessen. Die Möglichkeit, mittels der CSM Härteänderungen innerhalb weniger 10 nm zu messen, wurde anhand einer Modellprobe (TiC-Schicht auf TiAl6V4-Substrat) demonstriert und für die Bestimmung des Härte-Tiefenprofils innerhalb der implantierten Region einer mit Kohlenstoff implantierten TiAl6V4-Legierung genutzt. Die Mikrostruktur der implantierten Region ist hauptsächlich durch TiC-Ausscheidungen geprägt, deren Dichte sich kontinuierlich mit dem Kohlenstoff-Gehalt ändert: je höher der C-Gehalt, desto höher die Dichte an TiC-Ausscheidungen. Diese wiederum bestimmt die Härte innerhalb der implantierten Region: sie ist am höchsten in den Bereichen mit der höchsten Dichte an TiC-Ausscheidungen.

4.1 Einleitung

Werkzeuge und Bauteile sind Beanspruchungen ausgesetzt, die lokal (über den Querschnitt oder lateral) sehr stark variieren können. So sollte der Grundwerkstoff von Knie- und Hüftgelenken z. B. biokompatibel, mechanisch fest und ermüdungsbeständig sein, seine Oberfläche gleichzeitig aber auch eine hohe chemische Beständigkeit und einen hohen Verschleisswiderstand aufweisen. Die Titanlegierung TiAl6V4 besitzt nahezu alle diese Eigenschaften und wird daher als Material für Hüft- und Kniegelenke genutzt. Allein ihre Verschleissbeständigkeit ist ungenügend. Selbst bei Reibung gegen ein so weiches Material wie Polyethylen[1] wird ein Abrieb von schwarzen Titanoxidpartikeln beobachtet, welche als Drittkörper zu einem verstärkten Verschleiss sowohl des Polyethylens als auch der TiAl6V4-Oberfläche führen [6]. Durch eine Modifikation der TiAl6V4-Oberfläche mittels Ionenimplantation kann der Abrieb drastisch verringert und somit das Verschleissverhalten der TiAl6V4/Polyethylen-Paarung verbessert werden [69]. Dieses wird oft durch eine Erhöhung der Härte im oberflächennahen Bereich erklärt [7].

Bei der Ionenimplantation werden hochenergetische Ionen in die Oberfläche der Probe geschossen. Die Tiefe bis zu der die Ionen in die Probe eindringen, also die Dicke der implantierten Region, wird dabei im wesentlichen von der kinetischen Energie der Ionen bestimmt; typische Werte liegen im Bereich von 500 nm. Die implantierte Region selbst ist durch eine starke Variation der Mikrostruktur und der chemischen Zusammensetzung mit der Tiefe geprägt. Da die Eigenschaften eines Materials von dessen chemischer Zusammensetzung und seiner Mikrostruktur abhängen, haben diese Variationen in Mikrostruktur und chemischer Zusammensetzung innerhalb der implantierten Region entsprechende Änderungen der Eigenschaften zur Folge. Will man diesen Eigenschaftsgradienten gezielt den im Einsatz auftretenden Beanspruchungen anpassen, so ist ein grundlegendes Verständnis des Einflusses der Ionenimplantation auf die Eigenschaften innerhalb der implantierten Region notwendig. Dies beinhaltet zwei Punkte: (i) den Einfluss der Implantationsparameter auf die tiefenabhängige Variation von chemischer Zusammensetzung und Mikrostruktur und (ii) den Zusammenhang zwischen dieser tiefenabhängigen Variation von chemischer Zusammensetzung und Mikrostruktur und dem resultierenden Eigenschaftsgradienten. Thema der vorliegenden Arbeit ist der zweite Punkt, die unabhängige Bestimmung von chemischer Zusammensetzung und Mikrostruktur innerhalb der implantierten Region und deren Korrelation mit dem resultierenden Härte-Tiefenprofil.

Infolge der Größe der innerhalb der implantierten Region vorliegenden Gradienten war es notwendig, die tiefenabhängigen Messungen mit einer Tiefenauflösung im Bereich von 10 nm durchzuführen. Für die Bestimmung der chemischen Zusammensetzung und der Mikrostruktur stehen dazu mit der Augerelektronenspektroskopie bzw.

---

[1] Die Gelenkpfanne eines künstlichen Hüftgelenks bzw. das Schienbeinplateau eines künstlichen Kniegelenks besteht i.a. aus einem hochmolekularen Polyethylen (UHMWPE = "ultra-high molecular weight polyethylene").

der Querschnitts-Transmissionselektronenmikroskopie Standardverfahren zur Verfügung. Härtemessungen mit einer solchen Tiefenauflösung sind erst in den letzten Jahren durch die Entwicklung von Geräten zur registrierenden Härtemessung mit hochgenauer Last- und Wegmessung und der gleichzeitigen Entwicklung von entsprechenden Auswertemethoden möglich geworden. Bei der registrierenden Härtemessung wird eine Indenterspitze durch das Aufbringen einer definierten Last in die Oberfläche der Probe gedrückt und, nach Erreichen einer gegebenen Maximallast oder -tiefe, wieder entlastet. Während des Be- und des Entlastungszyklus werden sowohl die Last als auch die Eindringtiefe gemessen (Abb. 4.1a). Aus dieser Last-Eindringtiefe Kurve kann dann mit Hilfe eines geeigneten Auswerteverfahrens die Härte des Materials bestimmt werden. Die Last-Eindringtiefe Kurve, und damit auch die daraus bestimmten Härtewerte, repräsentieren einen Mittelwert über das von der Indenterspitze beeinflusste Materialvolumen. Dieses Volumen steigt mit zunehmender Maximallast (bzw. mit zunehmender Eindringtiefe) stark an. Härtemessungen, für die eine hohe Tiefenauflösung erforderlich ist, sollten daher mit einer niedrigen Maximallast durchgeführt werden.

Härte-Tiefenprofile wurden bis jetzt üblicherweise durch eine schrittweise Erhöhung der Maximallast und damit einer Erhöhung der maximalen Eindringtiefe bestimmt. Bei dieser Methode werden, schon bei Eindringtiefen die deutlich geringer sind als z. B. die Dicke der implantierten Region, die gemessenen Härtewerte sehr stark von den Eigenschaften des Substrates, also des von der Ionenimplantation nicht modifizierten Materials unterhalb der implantierten Region beeinflusst. Die mit dieser Methode bestimmten Härte-Tiefenprofile sind daher stark verschmiert und eine Tiefenauflösung im nm-Bereich kann nicht erreicht werden.

Aus diesem Grund wurden im ersten Teil der Arbeit zwei weitere Methoden der Härte-Tiefenprofilanalyse an einer Modellprobe, einer 200 nm dicken TiC-Schicht auf einem TiAl6V4-Substrat, getestet und im Hinblick auf ihre Tiefenauflösung verglichen. Im zweiten Teil der Arbeit wurde die tiefenabhängige Variation von Härte, chemischer Zusammensetzung und Mikrostruktur innerhalb der implantierten Region einer mit Kohlenstoffionen implantierten TiAl6V4-Legierung bestimmt und mit einer Genauigkeit von ± 20 nm korreliert. Eine solche Korrelation war bisher aufgrund der geringen Tiefenauflösung der Härte-Tiefenprofile nicht möglich.

4.2   Experimentelles

Probenmaterial und -präparation
Als Grundmaterial dienten polierte Scheiben einer TiAl6V4-Gusslegierung. Diese Scheiben wurden entweder mit TiC beschichtet oder mit Kohlenstoffionen implantiert.

Beschichtung.   Die TiC-Schicht wurde mittels reaktiven Sputterns in einer SPUTRON-Apparatur (Balzers) aufgebracht. Als Reaktionsgas wurde Azethylen (C_2H_2) verwendet und die Abscheidung erfolgte ohne Anlegen einer Vorspannung an das Substrat. Die Stöchiometrie der Schicht wurde mittels einer augerelektronenspek-
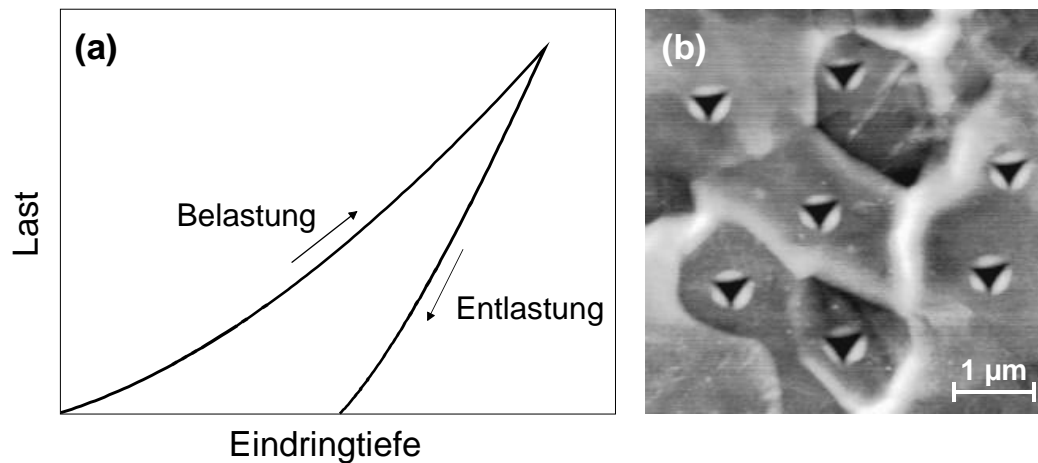
Abbildung 4.1: (a) Schema einer Last-Eindringtiefe Kurve und (b) Härteeindrücke in rekristallisiertem TiAl6V4. Eindrücke und Abbildung wurden mit derselben Spitze erzeugt. Man beachte, dass es möglich war, die Eindrücke jeweils in der Mitte der einzelnen Körner zu positionieren. Der Eindruck in der Mitte der oberen Bildhälfte wurde aus der Kornmitte verschoben, um die dort sichtbare Stufe zu meiden.

troskopischen Analyse mit etwa $TiC_{0,92}$ bestimmt. Die Schichtdicke wurde mit Hilfe eines Profilometers bestimmt und betrug 200 ± 10 nm.

Implantation. Die TiAl6V4-Substrate wurden zweifach mit Kohlenstoffionen implantiert. Die dabei verwendeten Beschleunigungsspannungen und Ionendosen waren $120\,\text{kV}/3 \cdot 10^{17}\,\text{cm}^{-2}$ und $60\,\text{kV}/4 \cdot 10^{17}\,\text{cm}^{-2}$. Die Implantationen erfolgten jeweils bei einer Temperatur unter 100°C.

Registrierende Härtemessung

Die registrierenden Härtemessungen wurden mit Hilfe eines kommerziellen Nanoindenters (Hysitron TriboScope) durchgeführt. Die Besonderheit dieses Gerätes besteht, neben seiner sehr hohen Last- und Wegauflösung (≈ 100 nN bzw. $\approx 0{,}2$ nm), darin, dass es mit einem Rasterkraftmikroskop[2] gekoppelt wird. Durch die Kombination dieser beiden Geräte kann die Indenterspitze sowohl zur registrierenden Härtemessung als auch zur Aufnahme von rasterkraftmikroskopischen Bildern genutzt werden. Somit kann der interessierende Oberflächenbereich vor und nach dem Eindrucksversuch abgebildet und, insbesondere, der Eindruck mit einer lateralen Genauigkeit von ca. 10 nm positioniert werden (Abb. 4.1 b).

Der Be- und Entlastungszyklus war für alle Eindrücke gleich: 5 s Belastung und 5 s Entlastung. Diese relativ kurzen Zeiten wurden gewählt, um den Einfluss einer thermischen Drift ($< 0{,}1$ nm/s) zu vermeiden. Die Härtewerte wurden mittels der Methode von Oliver und Pharr [2] aus den Last-Eindringtiefe Kurven bestimmt.

---

[2] Für diese Untersuchungen wurde ein NanoScope III MultiMode (Digital Instruments) verwendet.

Bestimmung des Tiefenprofils der chemischen Zusammensetzung

Das Tiefenprofil der chemischen Zusammensetzung wurde mittels einer Kombination von Augerelektronenspektroskopie (AES) und Materialabtrag durch Ionenzerstäubung (mittels Ar^+-Ionen) bestimmt. Die Analyse wurde in einer Raster-Auger-Mikrosonde (SAM PHI 600) durchgeführt.

Mikrostrukturelle Untersuchung

Zur Analyse der Mikrostruktur in Abhängigkeit von der Tiefe wurden Querschliffproben der C-implantierten TiAl6V4-Legierungen angefertigt. Die konventionellen transmissionselektronenmikroskopischen Untersuchungen wurden in einem JEM 2000 FX Elektronenmikroskop mit einer Beschleunigungsspannung von 200 kV durchgeführt.

Genauere Informationen zur Probenpräparation sowie zur Durchführung und Auswertung der verschiedenen Untersuchungen entnehmen Sie bitte den Kapiteln 2 und 3.

4.3 Härte-Tiefenprofilanalyse im Nanometerbereich

Das Härte-Tiefenprofil der Modellprobe TiC-Schicht/TiAl6V4-Substrat wurde mit den drei in Abb. 4.2 schematisch dargestellten Methoden bestimmt.

(1) *Lastvariationsmethode (LVM):* Das ist die derzeit übliche Methode der Härte-Tiefenprofilanalyse. Dabei werden alle Eindrücke senkrecht in die Oberfläche der TiC-Schicht gemacht. Ein Tiefenprofil wird durch die schrittweise Erhöhung der Maximallast und der damit verbundenen Erhöhung der maximalen Eindringtiefe des Indenters erhalten. In dieser Untersuchung wurden Maximallasten von 250 µN bis 10 mN verwendet. Bei jeder Last wurden jeweils drei Eindrücke mit einer dreiseitigen pyramidalen Indenterspitze (Berkovich) gemacht.

(2) *Methode der konstanten Last (CLM):* Im Gegensatz zur LVM, ist bei der CLM die Maximallast für alle Eindrucksversuche gleich *klein*: 250 µN. Um ein Tiefenprofil zu erhalten, wurde nach jeder Härtemessung etwas Material von der Oberfläche der TiC-Schicht abgetragen. Dies wurde durch Zerstäuben der Oberfläche mittels Ar^+-Ionen in der Auger-Apparatur erreicht. Dann wurden, auf der neu erzeugten Oberfläche der TiC-Schicht (dessen Dicke nun geringer war), wiederum Härtemessungen mit derselben Maximallast durchgeführt, u.s.w. In jeder Sputtertiefe wurden drei Härtemessungen mit der Berkovich-Indenterspitze durchgeführt.

(3) *Querschnittsmethode (CSM):* Die Härtemessungen wurden an einem Querschliff der Probe mit einer Maximallast von 200 µN durchgeführt. Um eine Kantenverrundung der TiC-Schicht während der Präparation des Querschliffs und einen Einfluss der freien Oberfläche während der Härtemessung zu vermeiden, wurde vor der Präparation des Querschliffs eine etwa 1 µm dicke TiN-Schutzschicht

Lastvariationsmethode
(LVM)

Methode der konstanten Last
(CLM)
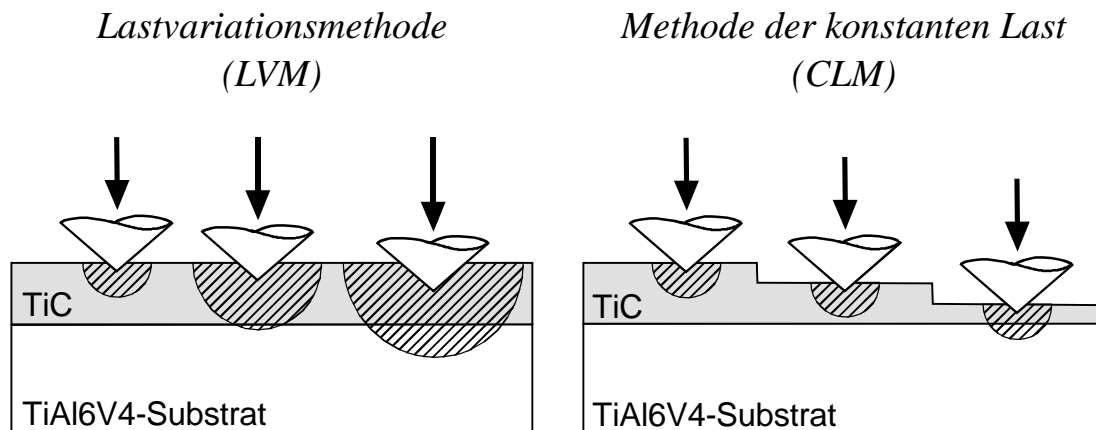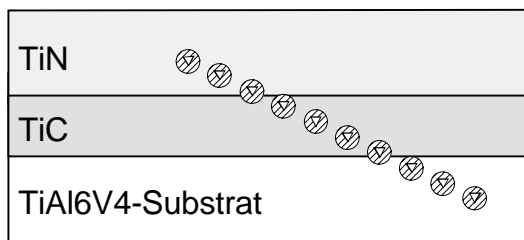

Querschnittsmethode
(CSM)

Abbildung 4.2: Schemata der drei Metho-
den der Härte-Tiefenprofilanalyse: Lastva-
riationsmethode (LVM), Methode der kon-
stanten Last (CLM) und Querschnittsmetho-
de (CSM). Die schraffierten Flächen deuten
jeweils das von der Indenterspitze beeinfluss-
te Materialvolumen an, für welches die Form
einer Halbkugel angenommen wurde. Wäh-
rend für die LVM dieses Volumen mit der Ma-
ximallast zunimmt, ist es im Falle der CLM
und der CSM für alle Eindrücke in erster Nä-
herung gleich.

auf die TiC-Schicht mittels reaktiven Sputterns abgeschieden. Die Härtemessun-
gen erfolgten – im Unterschied zur LVM und zur CLM – mit einem so genann-
ten Würfelspitzen-Indenter. Aufgrund der Geometrie des Berkovich-Indenters
(siehe S. 30) würde bereits ein Eindruck mit einer maximalen Eindringtiefe
von 25 nm die gesamte Schichtdicke von 200 nm umfassen. Der eingeschlos-
sene Halbwinkel eines Würfelspitzen-Indenters ist deutlich geringer als der ei-
nes Berkovich-Indenters (42.3° im Vergleich zu 70.3°). Die von einem Eindruck
gleicher Tiefe erfasste Kantenlänge ist daher für den Würfelkanten-Indenter um
einen Faktor von ca. 3 geringer als für einen Berkovich-Indenter.

Die mit den drei Methoden gemessenen Härte-Tiefenprofile sind in Abb. 4.3 darge-
stellt. Dabei hat der Parameter „Tiefe" für die drei Methoden eine unterschiedliche Be-
deutung (siehe Abb. 4.4): für die LVM ist die Tiefe gleich der maximalen Eindringtiefe
des Indenters ($t = h_{max}$). Im Falle der CLM wird die Tiefe durch die Summe aus der
maximalen Eindringtiefe des Indenters und der Sputtertiefe bestimmt ($t = h_{max} + h_{sp}$).
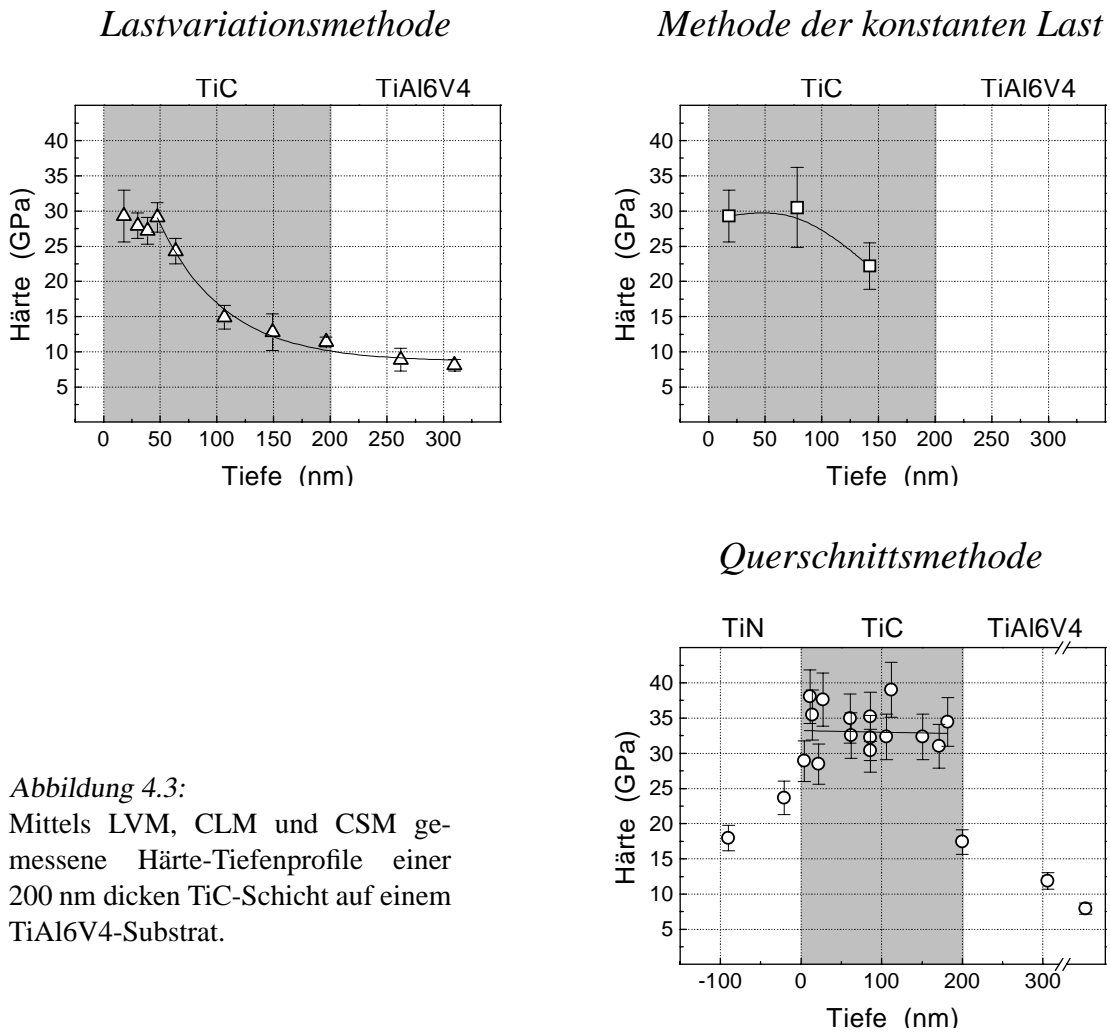
Lastvariationsmethode

Methode der konstanten Last

Querschnittsmethode

Abbildung 4.3:
Mittels LVM, CLM und CSM gemessene Härte-Tiefenprofile einer 200 nm dicken TiC-Schicht auf einem TiAl6V4-Substrat.

Für die CSM ist die Tiefe gleich dem lateralen Abstand des Eindrucks von der Grenzfläche TiC/TiN. Dieser wurde aus rasterkraftmikroskopischen Abbildungen bestimmt, die direkt nach dem Eindrucksversuch mit derselben Würfelspitze aufgenommen wurden.

Die Härte der TiC-Schicht kann in erster Näherung (eventuelle Gradienten von Mikrostruktur und Eigenspannungen werden vernachlässigt) als homogen über die gesamte Dicke angenommen werden. Ein Vergleich dieser Annahme mit den in Abb. 4.3 gezeigten Ergebnissen verdeutlicht die unterschiedliche Eignung der drei Verfahren zur Messung eines Härte-Tiefenprofils mit einer Auflösung im nm-Bereich.

Die LVM ergibt bis zu einer Tiefe von ca. 50 nm einen nahezu konstanten Härtewert. Bei größeren Tiefen ist ein starker Abfall der Härtewerte zu beobachten. Bei der CLM kann der Wert des Härteplateaus auch noch bei einer Tiefe von ca. 80 nm gemessen werden. Bei noch größeren Tiefen erfolgt jedoch auch hier ein deutlicher Abfall der Härtewerte. Der Grund ist in beiden Fällen derselbe. Die Ausdehnung des von der Indenterspitze beeinflussten Materialvolumens nimmt im Vergleich zur Schichtdicke
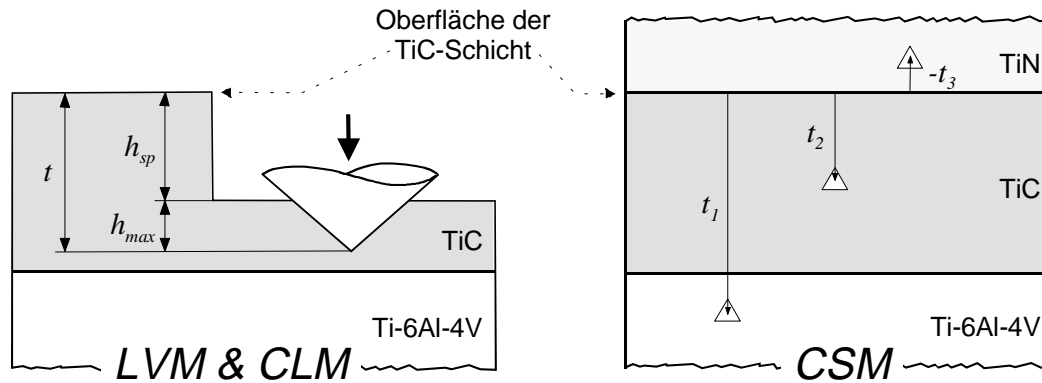
Abbildung 4.4: Schematische Darstellung der Bedeutung des in Abb. 4.3 genutzten Parameters „Tiefe", *t*, für die verschiedenen Methoden der Härte-Tiefenprofilanalyse (h_{sp}- Sputtertiefe, h_{max}- maximale Eindringtiefe des Indenters)

zu: bei der LVM aufgrund der zunehmenden Eindringtiefe des Indenters und bei der CLM wegen der schrittweisen Verringerung der Schichtdicke. Entsprechend steigt mit zunehmender Tiefe der Einfluss des weicheren Substrates auf den gemessenen Härtewert – das Härte-Tiefenprofil wird verschmiert. Aufgrund des für alle Eindrücke nahezu gleich großen beeinflussten Bereiches ist dieser Effekt für die CLM weniger stark ausgeprägt als für die LVM: die Tiefenauflösung der CLM ist höher als die der LVM.

Im Unterschied zur LVM und zur CLM, bei denen die Messungen in Richtung des Härtegradienten erfolgen, wird bei der CSM senkrecht zum Härtegradienten, also in eine Richtung mit homogener Härte gemessen. Dies und die Verwendung der gleichen, geringen Maximallast[3] für alle Eindrücke erklären, dass mittels der CSM ein Härteplateau über nahezu die gesamte Dicke der TiC-Schicht gemessen werden konnte und die Übergänge sowohl zum TiAl6V4-Substrat als auch zur TiN-Schutzschicht durch steile Abfälle der Härtewerte geprägt sind (siehe Abb. 4.3). Die CSM ist daher die einzige Methode die eine Messung von Härteänderungen im nm-Bereich erlaubt.

4.4 Härte-Tiefenprofil einer C-implantierten TiAl6V4-Legierung und dessen Verhältnis zu chemischer Zusammensetzung und Mikrostruktur

Chemische Zusammensetzung. Die Tiefenverteilung des Kohlenstoffs innerhalb der implantierten Region ist durch eine Überlagerung zweier Peaks charakterisiert (siehe Abb. 4.5). Der höhere Kohlenstoffgehalt des oberfächennäheren Peaks korrespondiert dabei mit der höheren Dosis und der geringeren kinetischen Energie der Ionen bei der

---

[3] Besser wäre, alle Messungen mit gleicher und geringer maximaler Eindringtiefe durchzuführen. Dies war mit dem in dieser Untersuchung verwendeten Gerät nicht möglich.

zweiten Implantation; der oberflächenfernere Peak ist das Ergebnis der ersten Implantation. Eine genauere Analyse der C (KLL)- und Ti (LMM)-Augerpeaks in Abhängigkeit von der Tiefe zeigte, dass (i) der gesamte implantierte Kohlenstoff als Titankarbid in der Probe vorliegt und (ii) im Tiefenbereich von 80–150 nm ein Plateau nahezu konstanten TiC-Gehaltes auftritt [116].

Mikrostruktur. Die hell-dunkel Kontraste in der Hellfeld-TEM-Aufnahme in Abb. 4.5 lassen deutlich die Existenz verschiedener Zonen mit unterschiedlicher Dicke innerhalb der implantierten Region erkennen. Mit Hilfe von Dunkelfeldaufnahmen konnte gezeigt werden, dass sich diese Zonen im wesentlichen durch die Dichte von TiC-Ausscheidungen unterscheiden [116]. Dies ist konsistent mit den Ergebnissen der AES-Analyse: je höher der C-Gehalt desto höher die Dichte von TiC-Ausscheidungen (Abb. 4.5). Auch Ergebnisse aus der Literatur stützen die Interpretation der Mikrostruktur innerhalb der implantierten Region: Für eine geringe Dosis implantierten Kohlenstoffs ($2 \cdot 10^{17}$ cm^{-2}/75 kV) wurde TiC in Form einzelner Ausscheidungen gefunden [1, 109], für höhere implantierte Dosen hingegen ($6 \cdot 10^{17}$ cm^{-2}/50 kV und $7 \cdot 10^{17}$ cm^{-2}/75 kV) wurde von der Bildung einer quasi-homogenen TiC-Schicht innerhalb der implantierten Region berichtet [1]. In einer der hier untersuchten Proben wurden TiC-Zwillinge beobachtet [116].

Härte. Das mittels der CSM bestimmte Härte-Tiefenprofil spiegelt die starken Variationen von Mikrostruktur und chemischer Zusammensetzung innerhalb der implantierten Region deutlich wieder: Ausgehend von der Oberfläche, steigt der Härtewert innerhalb weniger 10 nm von ca. 9 GPa auf etwa den dreifachen Wert an (Abb. 4.5). Wie die Tiefenverteilung des Kohlenstoffs, besitzt das Härte-Tiefenprofil zwei Peaks: einen mit einer sehr hohen Härte ($\approx$ 27 GPa) in einer Tiefe von etwa 80 nm und einen zweiten, mit einem geringeren Härtewert von ca. 15 GPa, in einer Tiefe von etwa 230 nm. Beide Härtemaxima treten in den Tiefen auf, wo der C-Gehalt – und somit die Dichte an TiC-Ausscheidungen (siehe oben) – am höchsten sind.

Eine solche Korrelation von Härte, chemischer Zusammensetzung und Mikrostruktur konnte mit dieser Genauigkeit – innerhalb von ± 20 nm – erstmals in dieser Dissertation gezeigt werden. Die Möglichkeit diesen Zusammenhang in diesen Dimensionen messen zu können, ist Voraussetzung für einen gezielten Einsatz der Ionenimplantation zur Modifikation der mechanischen/tribologischen Eigenschaften von Festkörpern.
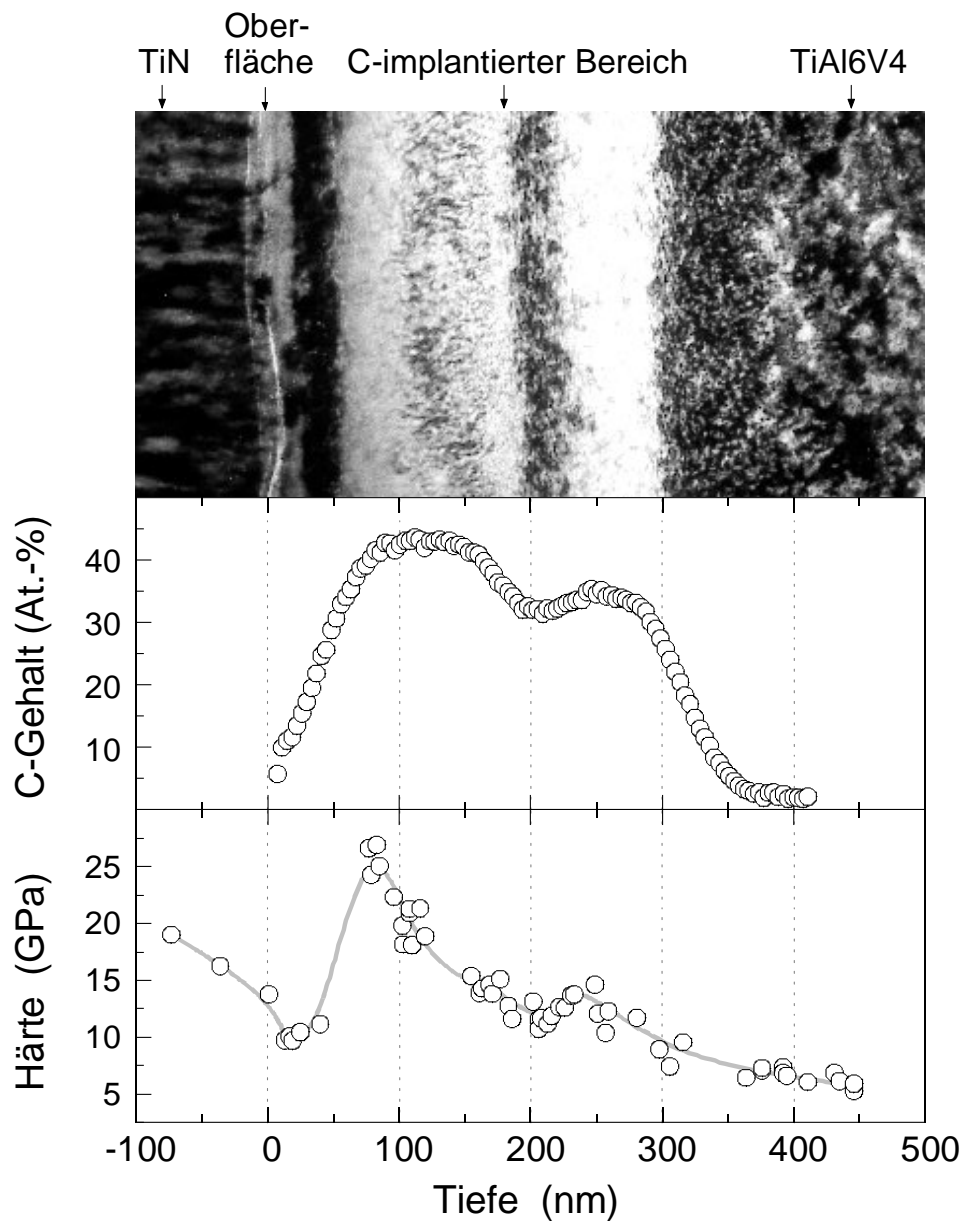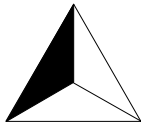
Abbildung 4.5: Variationen innerhalb der mit Kohlenstoff implantierten Region einer TiAl6V4-Legierung (v.o.n.u.): Mikrostruktur (Hellfeld-TEM-Abbildung), C-Gehalt und Härte (bestimmt mittels der CSM).

References

[1] R. N. Bolster, I. L. Singer, and R. G. Vardiman. *Composition, structure and wear resistance of Ti-6Al-4V implanted with carbon or boron to high doses.* Surf. Coat. Technol. **33** (1987) 469–477.

[2] W. C. Oliver and G. M. Pharr. *An improved technique for determining hardness and elastic modulus using load and displacement sensing indentation experiments.* J. Mater. Res. **7** (1992) 1564–1583.

[3] J. A. Brinell. In: *II. Cong. Int. Méthodes d' Essai.* Paris (1900) .

[4] S. Suresh and A. Mortensen. *Functionally Gradient Materials - Processing and Thermomechanical Behaviour of Graded Materials and Metal-Ceramic Composites.* Institute of Metals-Books: Vol. 698 (1998). This book is a revised, expanded, updated and integrated version of a two-part review by the authors which appeared in *International Material Reviews* in 1995 and 1997.

[5] T. Burakowski and T. Wierzchoń. *Surface Engineering of Metals: Principles, Equipment, Technologies.* Materials Science and Technology. CRC Press LLC, Boca Raton, London, New York, Washington D.C. (1999).

[6] D. H. Kohn and P. Ducheneyne. *Materials for bone and joint replacements.* In: *Medical and Dental Materials* (D. F. Williams, ed.), vol. 14 of *Materials Science and Technology.* VCH, Weinheim-New York-Basel-Cambridge (1992) pp. 29–109.

[7] F. Alonso, A. Arizaga, S. Quainton, J. J. Ugarte, J. L. Viviente, and J. I. Oñate. *Mechanical properties and structure of Ti-6Al-4V alloy implanted with different light ions.* Surf. Coat. Technol. **74/75** (1995) 986–992.

[8] F. Mohs. *Grundriss der Mineralogie.* Dresden (1822).

[9] B. Bhushan. *Nanomechanical properties of solid surfaces and thin films*. In: *Handbook of Micro/Nano Tribology* (B. Bhushan, ed.), Mechanical and Materials Science Series. CRC Press, Inc. (1995) pp. 321–396.

[10] B. Bhushan, A. V. Kulkarni, W. Bonin, and J. T. Wyrobek. *Nanoindentation and picoindentation measurements using a capacitive transducer system in atomic force microscopy*. Phil. Mag. A **74** (1996) 1117–1128.

[11] *TriboScope Software V. 3.0b*. (Hysitron Inc., 1996, Minneapolis, MN, USA).

[12] *TriboScope™. Nanomechanical Test System -User's Manual*. (Hysitron Inc., 1996, Minneapolis, MN, USA).

[13] J. L. Loubet, J. M. Georges, and G. Meille. *Vickers indentation curves of elastoplastic materials*. In: *Microindentation Techniques in Materials Science and Engineering* (P. J. Blau and B. R. Lawn, eds.). ASTM, Philadephia (1986) pp. 72–89.

[14] S. V. Hainsworth, H. W. Chandler, and T. F. Page. *Analysis of nanoindentation load-displacement loading curves*. J. Mater. Res. **11** (1996) 1987–1995.

[15] Y.-T. Cheng and C.-M. Cheng. *Further analysis of indentation loading curves: Effects of tip rounding on mechanical property measurements*. J. Mater. Res. **13** (1998) 1059–1064.

[16] M. Sakai. *Energy principle of the indentation-induced inelastic surface deformation and hardness of brittle materials*. Acta metall. mater. **41** (1993) 1751–1758.

[17] J. Gubicza, A. Juhász, and J. Lendvai. *A new method for hardness determination from depth sensing indentation tests*. J. Mater. Res. **11** (1996) 2964–2967.

[18] M. F. Doerner and W. D. Nix. *A method for interpreting the data from depth-sensing indentation instruments*. J. Mater. Res. **1** (1986) 601–609.

[19] I. N. Sneddon. *The relation between load and penetration in the axisymmetric Boussinesq problem for a punch of arbitrary profile*. Int. J. Eng. Sci. **3** (1965) 47–57.

[20] S. I. Bulychev and V. P. Alekhin. Zavod. Lab. **53** (1987) 76.

[21] S. P. Baker. *The Analysis of Depth-Sensing Indentation Data*. In: *Thin Films: Stresses and Mechanical Properties IV* (P. H. Townsend, T. P. Weihs, J. E. Sanchez, Jr., and P. Børgesen, eds.). Mat. Res. Soc. Symp. Proc. Vol. 308, Pittsburgh, PA (1993) pp. 209–219.

[22] D. Tabor. *The Hardness of Metals*. Oxford, Clarendon Press (1951).

[23] D. Tabor. *Indentation hardness and its measurement: Some cautionary comments*. In: *Microindentation Techniques in Materials Science and Engineering* (P. J. Blau and B. R. Lawn, eds.). American Society for Testing and Materials, Philadephia (1986) pp. 129–159.

[24] K. L. Johnson. *The correlation of indentation experiments*. J. of Mech. and Phys. of Solids **18** (1970) 115–126.

[25] A. Bolshakov. *Finite Element Studies of Mechanical Property Testing by Nanoindentation Methods*. Ph.D. thesis, Rice University, Houston, Texas (1996).

[26] R. Hill. *Theory of Plasticity*. University Press, Oxford (1950).

[27] D. M. Marsh. *Plastic flow in glass*. Proc. Royal Society **A279** (1964) 420.

[28] W. Hirst and M. G. J. W. Howse. *The indentation of materials by wedges*. Proc. Royal Soc. **A 311** (1969) 429–444.

[29] S. S. Chiang, D. B. Marshall, and A. G. Evans. *The response of solids to elastic/plastic indentation. I. Stresses and residual stresses*. J. Appl. Phys. **53** (1982) 298–311.

[30] K. L. Johnson. *Contact Mechanics*. Cambridge Unsiversity Press (1985).

[31] S. Harvey, H. Huang, S. Venkataraman, and W. W. Gerberich. *Microscopy and microindentation mechanics of single crystal Fe–3 wt.% Si: Part I. Atomic force microscopy of a small indentation*. J. Mater. Res. **8** (1993) 1291–1299.

[32] J. D. Kiely, R. Q. Hwang, and J. E. Houston. *Effect of surface steps on the plastic treshold in nanoindentation*. Phys. Rev. Lett. **81** (1998) 4424–4427.

[33] D. F. Bahr and W. W. Gerberich. *Plastic zone and pileup around large indentations*. Metall. Mater. Trans. **27A** (1996) 3793–3800.

[34] A. Bolshakov, W. C. Oliver, and G. M. Pharr. *Influence of stress on the measurement of mechanical properties using nanoindentation: Part II. Finite element simulations*. J. Mater. Res. **11** (1996) 760–768.

[35] S. P. Baker. private communication (1997).

[36] T. F. Page, W. C. Oliver, and C. J. McHargue. *The deformation behavior of ceramic crystals subjected to very low load (nano)indentation*. J. Mater. Res. **7** (1992) 450–.

[37] W. Zielinski, H. Huang, and W. W. Gerberich. *Microscopy and microindentation mechanics of single crystal Fe–3 wt.% Si: Part II. TEM of the indentation plastic zone*. J. Mater. Res. **8** (1993) 1300–1310.

[38] M. Odén, H. Ljungcrantz, and L. Hultman. *Characterization of the induced plastic zone in a single crystal TiN (001) film by nanoindentation and transmission electron microscopy*. J. Mater. Res. **12** (1997) 2134–2142.

[39] C. Robertson, S. Poissonnet, and L. Boulanger. *Plasticity in ion-irradiated austenitic stainless steels*. J. Mater. Res. **13** (1998) 2123–2131.

[40] M. A. Wall and U. Dahmen. *An in situ nanoindentation specimen holder for a high voltage transmission electron microscope*. Microscopy Research & Technique **42** (1998) 248–254.

[41] H. Bückle. *Use of hardness test to determine other material properties*. In: *The science of hardness testing and its research application* (J. H. Westbrook and H. Conrad, eds.). ASM, Metals Park, Ohio (1973) pp. 453–494.

[42] W. C. Oliver, R. Hutchings, and J. B. Pethica. *Measurements of hardness at indentation depths as low as 20 nanometers*. In: *Microindentation Techniques in Materials Science and Engineering* (P. J. Blau and B. R. Lawn, eds.). ASTM, Philadephia (1986) pp. 90–108.

[43] M. S. Bobij and S. K. Biswas. *Estimation of hardness by nanoindentation of rough surfaces*. J. Mater. Res. **13** (1998) 3227–3233.

[44] J. F. Song and T. V. Vorburger. *Surface texture*. In: *ASM Handbook,* Vol.18 "Friction, Lubrication, and Wear Technology". Materials Park, OH (USA) (1992) pp. 334–345.

[45] J. D. Kiely and D. A. Bonnell. *Quantification of topographic structure by scanning probe microscopy*. J. Vac. Sci. Technol. **B 15** (1997) 1483–1493.

[46] K. L. Westra and D. J. Thomson. *Effect of tip shape on surface roughness measurements from atomic force microscopy images of thin films*. J. Vac. Sci. Technol. **B 13** (1995) 344–349.

[47] T. A. Laursen and J. C. Simo. *A study of the mechanics of microindentation using finite elements*. J. Mater. Res. **7** (1992) 618–626.

[48] J. B. Pethica and D. Tabor. *Contact of characterised metal surfaces at very low loads: deformation and adhesion*. Surface Science **89** (1979) 182–190.

[49] P. J. Burnett and D. S. Rickerby. *The mechanical properties of wear-resistant coatings; I: Modelling of hardness behaviour*. Thin Solid Films **148** (1986) 41–50.

[50] A. M. Korsunsky, M. R. McGurk, S. J. Bull, and T. F. Page. *On the hardness of coated systems*. Surf. Coat. Technol. **99** (1998) 171–183.

[51] T. Y. Tsui, J. Vlassak, and W. D. Nix. *Indentation plastic displacement field: Part I. The case of soft films on hard substrates*. J. Mater. Res. **14** (1999) 2196–2203.

[52] T. Y. Tsui, J. Vlassak, and W. D. Nix. *Indentation plastic displacement field: Part II. The case of hard films on soft substrates*. J. Mater. Res. **14** (1999) 2204–2209.

[53] M. R. McGurk and T. F. Page. *Using the P-δ^2 analysis to deconvolute the nanoindentation response of hard-coated systems*. J. Mater. Res. **14** (1999) 2283–2295.

[54] S. K. Biswas, K. Venkatesh, M. S. Bobij, and K. S. Sebastian. *Nanoindentation*. Trans. Indian Inst. Met. **49** (1996) 725–738.

[55] J. B. Pethica and W. C. Oliver. *Mechanical properties of nanometre volumes of material: Use of the elastic response of small area indentations*. In: *Thin Films: Stresses and Mechanical Properties* (J. C. Bravman, W. D. Nix, D. M. Barnett, and D. A. Smith, eds.), Mat. Res. Soc. Symp. Proc. Pittsburgh, PA (1989) pp. 13–23.

[56] W. W. Gerberich, J. C. Nelson, E. T. Lilleodden, P. Anderson, and J. T. Wyrobek. *Indentation induced dislocation nucleation: The initial yield point*. Acta mater. **44** (1996) 3585–3598.

[57] S. P. Baker. *Between nanoindentation and scanning force microscopy: Measuring mechanical properties in the nanometer regime*. Thin Solid Films **308–309** (1997) 289–296.

[58] N. X. Randall, C. Julia-Schmutz, and J. M. Soro. *Combining scanning force microscopy with nanoindentation for more complete characterisation of bulk and coated materials*. Surf. Coat. Technol. **108/109** (1998) 489–495.

[59] N. A. Burnham and R. J. Colton. *Measuring the nanomechanical properties and surface forces of materials using an atomic force microscope*. J. Vac. Sci. Technol. **A 7** (1989) 2906–2913.

[60] S. M. Hues, R. J. Colton, E. Meyer, and H.-J. Güntherodt. *Scanning probe microscopy of thin films*. MRS Bulletin **18** (Jan. 1993) 41–49.

[61] S. M. Hues, C. F. Draper, and R. J. Colton. *Measurement of nanomechanical properties of metals using the atomic force microscope*. J. Vac. Sci. Technol. **B 12** (1994) 2211–2214.

[62] S. Bec, A. Tonck, J.-M. Georges, E. Georges, and J.-L. Loubet. *Improvement in the indentation method with a surface force apparatus*. Phil. Mag. A **74** (1996) 1061–1072.

[63] N. A. Stelmashenko, M. G. Walls, L. M. Brown, and Y. Milman. *Microindentations on W and Mo oriented single crystals: An STM study*. Acta Metall. Mater. **41** (1993) 2855–2865.

[64] J. B. Pethica and W. C. Oliver. *Tip surface interactions in STM and AFM*. Physica Scripta **T 19** (1987) 61–66.

[65] G. M. Pharr, A. Bolshakov, T. Y. Tsui, and J. C. Hay. *Nanoindentation of soft films on hard substrates: Experiments and finite element simulations*. In: *Thin Films: Stresses and Mechanical Properties VII* (R. C. Cammarata, M. Nastasi, E. P. Busso, and W. C. Oliver, eds.). Mat. Res. Soc. Symp. Proc., Vol. 505, Pittsburgh, PA (1998) pp. 109–120.

[66] A. Matthews, A. Leyland, K. Holmberg, and H. Ronkainen. *Design aspects for advanced tribological surface coatings*. Surf. Coat. Technol. **100-101** (1998) 1–6.

[67] M. Huq, J. Celis, J. Meneve, L. Stals, and D. Schryvers. *Oscillating sliding wear of mono- and multilayer ceramic coatings in air*. Surf. Coat. Technol. **113** (1999) 242–250.

[68] A. A. Voevodin, M. A. Capano, S. J. P. Laube, M. S. Donley, and J. S. Zabinski. *Design of a Ti/TiC/DLC functionally gradient coating based on studies of structural transitions in Ti-C thin films*. Thin Solid Films **298** (1997) 107–115.

[69] J. K. Hirvonen. *Ion beam processing for surface modification*. Annu. Rev. Mater. Sci. **19** (1989) 401–417.

[70] I. L. Singer, R. N. Bolster, H. M. Pollock, and J. D. J. Ross. *Polishing wear behavior and surface hardness of ion-beam-modified Ti-6Al-4V*. Surf. Coat. Technol. **36** (1988) 531–540.

[71] B. R. Lawn, A. G. Evans, and D. B. Marshall. *Elastic/plastic indentation damage in ceramics: The median/radial crack system*. J. of Amer. Ceram. Soc. **63** (1980) 574–581.

[72] A. K. Battacharya and W. D. Nix. *Analysis of elastic and plastic deformation associated with indentation testing of thin films on substrates*. Int. J. Solids Structures **24** (1988) 1287–1298.

[73] B. D. Fabes, W. C. Oliver, R. A. McKee, and F. J. Walker. *The determination of film hardness from the composite response of film and substrate to nanometer scale indentations*. J. Mater. Res. **7** (1992) 3056–3064.

[74] M. R. McGurk, H. W. Chandler, P. C. Twigg, and T. F. Page. *Modeling the hardness response of coated systems - the plate-bending approach*. Surf. Coat. Technol. **68/69** (1994) 5076–5081.

[75] D. Chicot and J. Lesage. *Absolute hardness of films and coatings*. Thin Solid Films **254** (1995) 123–130.

[76] P. Grau, G. Berg, H. Oettel, and R. Wiedemann. *Comparison of profile functions for the estimation of the film hardness from compound hardness measurements by a depth-sensitive method*. phys. stat. sol. (a) **159** (1997) 447–460.

[77] J. A. Knapp, D. M. Follstaedt, S. M. Myers, J. C. Barbour, and T. A. Friedmann. *Finite-element modeling of nanoindentation*. J. Appl. Phys. **85** (1999) 1460–1474.

[78] D. Chicot, Y. Bénarioua, and J. Lesage. *Hardness measurements of Ti and TiC multilayers: A model*. Thin Solid Films **359** (2000) 228–235.

[79] *MultiPak V. 5.0*. (Physical Electronics, 1997, Eden Prairie, Minnesota, USA).

[80] *Surface roughness-terminology: Part 1: Surfaces and its parameters. ISO 4287/1* (1984).

[81] *Digital Instruments Software V. 4.31r7*. (Digital Instruments, 1997, Santa Barbara, California, USA).

[82] E. S. Berkovich. *Three–faceted diamond pyramid for micro-hardness testing*. Indus. Diamond Rev. **11** (1951) 129–132.

[83] K. Wittmaack. *Surface and depth analysis based on sputtering*. In: *Sputtering by Particle Bombardement III* (R. Behrisch and K. Wittmaack, eds.). Springer-Verlag, Berlin-Heidelberg-New York (1991) pp. 161–256.

[84] M. Lichinchi, C. Lenardi, J. Haupt, and R. Vitali. *Simulation of Berkovich nanoindentation experiments on thin films using finite element method*. Thin Solid Films **312** (1998) 240–248.

[85] C. Maerky, M.-O. Guillou, J. L. Henshall, and R. M. Hooper. *Indentation hardness and fracture toughness in single crystal* $TiC_{0.96}$. Mater. Sci. and Eng. **A209** (1996) 329–336.

[86] H. Oettel and R. Wiedemann. *Residual stresses in PVD hard coatings*. Surf. Coat. Technol. **76-77** (1995) 265–273.

[87] D. S. Rickerby and P. J. Burnett. *Correlation of process and system parameters with structure and properties of physically vapour deposited hard coatings*. Thin Solid Films **157** (1988) 195–222.

[88] P. Panjan, B. Navinsek, A. Cvelbar, A. Zalar, and I. Milosev. *Oxidation of TiN, ZrN, TiZrN, CrN, TiCrN and TiN/CrN multilayer hard coatings reactively sputtered at low temperature*. Thin Solid Films **281–282** (1996) 298–301.

[89] G. Welsch and W. Bunk. *Deformation modes of the α-phase of Ti-6Al-4V as a function of oxygen concentration and aging temperature*. Metall. Trans. **A13** (1982) 889–899.

[90] M. Kunert, B. Baretzky, S. P. Baker, and E. J. Mittemeijer. *Hardness-depth profiling on nanometer scale*. to be published (Chapter 2 of this dissertation).

[91] *Ternery Alloys*. In: *Al-Ni-Tb to An-Zn-Zr* (G. Petzow and G. Effenberg, eds.), vol. 8. VCH (1992) p. 426 ff.

[92] D. M. Rück, N. Andert, H. Emig, K. D. Leible, P. Spädtke, D. Vogt, and B. H. Wolf. *Ion implantation facilities at GSI*. Nucl. Tracks Radiat. Meas. **19** (1991) 951–954.

[93] H. Schmidt, A. Schminke, and D. M. Rück. *Tribological behaviour of ion-implanted Ti-6Al-4V sliding against polymers*. Wear **209** (1997) 49–56.

[94] S. Hofmann and J. Steffen. *Factor analysis and superposition of Auger electron spectra applied to room temperature oxidation of Ni and $NiCr_{21}Fe_{12}$*. Surf. Interface Anal. **14** (1989) 59–65.

[95] B. A. Kooi and M. A. J. Somers. *Factor analysis of Fe $M_{2,3}$VV spectra of oxidizing iron: The role of the background emergence of ghost components*. Surf. Interface Anal. **21** (1994) 501–513.

[96] D. A. Shirley. *High-resolution x-ray photoemission spectrum of the valence bands of gold*. Phys. Rev. B **5** (1972) 4709–4714.

[97] A. Strecker, U. Salzberger, and J. Mayer. *Specimen preparation for Transmission Electron Microscopy: Reliable method for cross-sections and brittle materials*. Prakt. Metallogr. **30** (1993) 482–495.

[98] R. Spolenak, B. Heiland, C. Witt, R.-M. Keller, P. Müllner, and E. Arzt. *Zielpräparation von TEM-Proben mit dem fokussierten Ionenstrahl (FIB)*. Prakt. Met. Sonderband **30** (1999) 229–236.

[99] P. A. Stadelmann. *EMS – A software package for electron diffraction analysis and HREM image simulation in materials science*. Ultramicroscopy **21** (1987) 131–145.

[100] A. Berger, J. Mayer, and H. Kohl. *Detection limits in elemental distribution images produced by energy filtering TEM: Case study of grain boundaries in Si_3N_4*. Ultramicroscopy **55** (1994) 101–112.

[101] H. Rose and E. Plies. *Entwurf eines fehlerarmen magnetischen Energie-Analysators*. Optik **40** (1974) 336–341.

[102] J. Mayer. *Applications of energy filtering TEM in materials science*. European Microscopy and Analysis **9** (1993) 21–23.

[103] C. Jeanguillaume, P. Trebbia, and C. Colliex. *About the use of electron energy-loss spectroscopy for chemical mapping of thin foils with high spatial resolution*. Ultramicroscopy **3** (1978) 237.

[104] G. M. Pharr. *Measurement of mechanical properties by ultra-low load indentation*. Mat. Sci. Engin. **A253** (1998) 151–159.

[105] P. Sigmund. In: *Sputtering by Particle Bombardement* (R. Behrisch, ed.). Springer–Verlag, Berlin–Heidelberg–New York (1981) pp. 9–71.

[106] T. W. Haas, J. T. Grant, and G. J. Dooley. *Chemical effects in Auger electron spectroscopy*. J. Appl. Phys. **43** (1972) 1853–1860.

[107] T. B. Massalski, ed. *Binary Alloy Phase Diagrams*, vol. 1. ASM International, 2nd ed. (1990).

[108] X. Qiu, R. A. Dodd, J. R. Conrad, A. Chen, and F. J. Worzala. *Microstructural study of nitrogen-implanted Ti-6Al-4V alloy*. Nucl. Instrum. Meth. in Phys. Res. **B56/60** (1991) 951–956.

[109] R. G. Vardiman and R. A. Kant. *The improvement of fatique life in Ti-6Al-4V by ion implantation*. J. Appl. Phys. **53** (1982) 690–694.

[110] Y. P. Sharkeev, A. N. Didenko, and E. V. Kozlov. *High dislocation density structures and hardening produced by high fluency pulsed-ion-beam implantation*. Surf. Coat. Technol. **65** (1994) 112–120.

[111] A. P. Sutton and R. W. Balluffi. *On geometric criteria for low interfacial energy*. Acta metall. **35** (1987) 2177–2201.

[112] R. Boyer, G. Welsch, and E. W. Collings, eds. *Materials Properties Handbook: Titanium Alloys*. ASM International, Materials Park, OH (1994).

[113] M. Kunert, B. Baretzky, S. P. Baker, and E. J. Mittemeijer. *Nanometer-scale measurements of mechanical properties and composition in an ion implanted titanium-based alloy*. In: *Fundamentals of Nanoindentation and Nanotribology* (S. P. Baker, N. Burnham, W. W. Gerberich, and N. R. Moody, eds.), vol. 522 of *Mat. Res. Soc. Symp. Proc.*. Warrendale, PA (1998) pp. 95–100.

[114] J. W. Martin. *Precipitation Hardening*. Butterworth-Heinemann, Oxford (1998).

[115] J. S. Solomon and W. L. Braun. *Molecular orbital effects on the Ti LMV Auger spectra of TiO and TiO_2*. Surf. Science **51** (1975) 228–236.

[116] M. Kunert, O. Kienzle, B. Baretzky, S. P. Baker, and E. J. Mittemeijer. *Hardness-depth profile of a carbon- implanted Ti-6Al-4V alloy and its relation to composition and microstructure.* to be published (Chapter 3 of this dissertation).
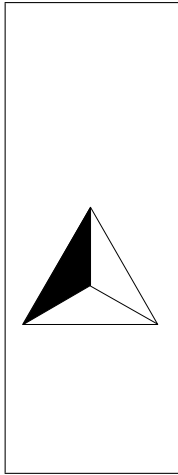
Curriculum Vitae

Maik Kunert
born on 17th of march 1970 in Görlitz

School

1976–1986	school, Görlitz
1986–1988	secondary school, Halle (Saale), high school graduation ("Abitur")

Higher education

9/89–9/91	State Metallurgical Institute, Dnepropetrovsk (Ukraine), Metallurgy
10/91–2/96	Technical University Bergakademie Freiberg, Materials Science and Technology, Dipl.-Ing. Degree dissertation: *"Influence of transition elements on the microstructure of Beryllium"*
9/96–4/00	PhD at Max-Planck-Institut für Metallforschung, Institute for Materials Science, Stuttgart